Miguel Alexandre Ramos de Melo

Implementation and development of a system for the fabrication of Bragg gratings with special characteristics

Universidade do Porto
Faculdade de Engenharia
FEUP

Thesis submitted to the Faculty of Engineering of the University of Porto
for the degree of Master in Electrical and Computer Engineering

Department of Electrical and Computer Engineering
Faculty of Engineering, University of Porto
2006

Thesis supervised by

Paulo Vicente da Silva Marques, Ph.D.
Assistant Professor in the Physics Department
Faculty of Science, University of Porto

and co-supervised by

Henrique Manuel de Castro Faria Salgado, Ph.D.
Associate Professor in the Department of Electrical and Computer Engineering
Faculty of Engineering, University of Porto

"Tell me and I forget.
Teach me and I remember.
Involve me and I learn."
Benjamin Franklin

Acknowledgements

The possibility of working at the labs of the Optoelectronics and Electronic Systems Unit (UOSE) of INESC Porto, located at the Science Faculty of the University of Porto, was fundamental for the execution of the work presented in this thesis. Following this, I have to start by thanking to Prof. José Luís Santos for giving me the opportunity to work in such a group, and especially for his friendship. His advices during my stay at INESC Porto have always indicated the best path to achieve success in my professional activities.

A very special acknowledgement is also for my supervisor, Prof. Paulo Marques, which made this thesis possible. His continuous effort and hard work on creating conditions for the execution of this work were essential to the accomplishment of the proposed objectives. Also, his constant availability, support and guidance through all the work made me feel much more comfortable in carrying out each task. It was a great pleasure to work with him as it will be anytime in the future…

I also would like to thank my co-supervisor, Prof. Henrique Salgado, for his support, suggestions and final remarks to this thesis.

To my friends that since the beginning of college and until now gave always me their support: Dionisio, Filipe, Rui, Luís and Jaime; and to all the people from UOSE, namely Orlando, Gaspar, Paulo Caldas, Pedro Jorge, Joel, Rosa, Daniel, Diana and Paulo Moreira by the good work environment created, exchange of ideas and suggestions. And of course I cannot forget Luísa.

Thanks to Prof. Pereira Leite for his interest and suggestions in some points of this work. Thanks to Multiwave Photonics, SA, especially to Martin Berendt and João Sousa that provided me time to write this thesis and the opportunity of making some last characterization measurements.

The beginning of this project is intimately linked to Dr. Isabelle Riant (Alcatel CIT, France) and Prof. Marc Douay (Univ. Lille, France) that trusted in our work and so a special acknowledgment should also be given to them.

I also would like to thank the European Community for the project PLATON – PLAnar Technology for Optical Networks, under which this work was developed. From here several project partners contributed to this thesis, namely Alcatel SEL (Stuttgart, Germany) and IPHT - Institute for Physical High Technology (Jena, Germany) by delivering planar samples to test, Highwave Optical Technologies (France) by proving us with some photosensitive fiber and TUHH - Technische Universität Hamburg – Harburg (Germany) by proving spatially modelled profiles and by performing its characterization when needed.

To my parents and to Elisabete…for everything!

Summary

Bragg gratings are nowadays key components in numerous optical fiber systems. From the wide range of applications, these structures find particular relevance in the fields of sensors and optical communications. In this last domain, Bragg gratings have important functionalities as filters and dispersion compensators. However, in this kind of applications, the fabrication of these structures with special characteristics is necessary.

This work presents a system for the inscription of apodized, chirped and phase shifted Bragg gratings using the phase mask dithering technique. The advantages of this technique consist basically in the possibility of tailoring the Bragg gratings characteristics in order to fit a particular application, based in an efficient and reliable method, using simply a standard uniform phase mask. An experimental setup, as well as all the software in a LabView™ platform, for the fabrication of these elements, was implemented and developed. This includes several apodization functions (pre-defined or that can be read from a file after modelling) and routines for the introduction of phase shifts and chirp behaviour in Bragg gratings. All the aspects regarding the experimental implementation and calibrations required are also described in this work.

Experimental results of complex Bragg gratings fabricated by the implemented phase mask dithering technique, and using the developed software, are presented. Initially, a study of the setup and a certification of all the calibrations used were performed. Apodized Bragg gratings with pre-defined functions and modelled spatial profiles were written, resulting in efficient side mode suppression levels in high reflective gratings. Chirped gratings with reasonable spectral bandwidths and showing dispersion properties, $\pi/2$, π and $3\pi/2$ phase shifted gratings and sampled Bragg gratings, either in amplitude either in phase, achieving equalization, were also fabricated.

After the demonstration of this method in optical fibers, the setup was converted to allow Bragg gratings inscription in silica-on-silicon planar devices. Gratings in channel waveguides and Mach-Zhender interferometers were written for implementation of optical add-drop MUX/DEMUX functions in planar technology.

Sumário

Redes de Bragg são, hoje em dia, considerados elementos fundamentais em inúmeros sistemas de fibra óptica. De entre as muitas aplicações possíveis, estas encontram particular interesse na área dos sensores e das comunicações ópticas. Neste último domínio, as redes de Bragg encontram importantes aplicações como filtros e compensadores de dispersão. No entanto, neste tipo de aplicações é necessária a fabricação de estruturas com características especiais.

Assim, este trabalho apresenta um sistema de escrita de redes de Bragg apodizadas, "chirp" e com desvios de fase baseado na técnica de vibração da máscara de fase. As vantagens desta técnica consistem essencialmente na possibilidade de fabricação de redes de Bragg com as caracteristicas desejadas utilizando um método eficiente e reprodutivel, utilizando apenas uma máscara de fase uniforme. Foi implementada e desenvolvida uma montagem experimental, bem como todo o software de controlo associado baseado na plataforma de LabView™, para a fabricação destes elementos. Este inclui diversas funções de apodização (pré-definidas ou que podem ser lidas a partir de um ficheiro obtido após modelização) e rotinas para introdução de desvios de fase e comportamento chirp em redes de Bragg. Todas as considerações relativamente à implementação prática e calibrações necessárias são também aqui descritas.

Resultados experimentais de redes de Bragg complexas fabricadas pela técnica de vibração da máscara de fase implementada, e usando o software desenvolvido, são apresentados. Inicialmente foi efectuado um estudo da montagem e uma verificação de todas as calibrações usadas. Redes de Bragg apodizadas com funções pré-definidas e perfis espaciais simulados foram escritas, resultando numa eficiente supressão dos lóbulos laterais em redes com elevada reflectividade. Redes chirp com larguras de banda espectrais razoáveis e apresentando propriedades de dispersão, redes com desvios de fase de $\pi/2$, π e $3\pi/2$ e redes de Bragg amostradas, quer em amplitude quer em fase, tendo-se conseguido equalização de picos, foram também fabricadas.

Após a demonstração do método em fibras, a montagem experimental foi convertida de forma a permitir a escrita de redes de Bragg em dispositivos ópticos planares em sílica-sobre-silício. Foram escritas redes em guias e em interferómetros Mach-Zhender para implementação de multiplexagem/desmultiplexagem óptica em tecnologia planar.

Acknowledgements 7
Summary 9
Sumário 11
Index 13
List of Figures 15

1 Introduction 19
1.1 Motivation 19
1.2 Overview and state of the art 20
1.3 Thesis content 26

2 Theory of Bragg gratings 29
2.1 Introduction 29
2.2 Bragg grating fundamentals 29
2.3 Coupled mode theory 33
2.4 Transfer matrix method 46
2.5 Bragg gratings with special characteristics 50
2.5.1 Apodized Bragg gratings 50
2.5.2 Chirped Bragg gratings 54
2.5.3 Phase shifted Bragg gratings 57
2.5.4 Sampled Bragg gratings 59
2.6 Photosensitivity 61
2.7 Conclusion 64

3 Bragg gratings fabrication methods 65
3.1 Introduction 65
3.1.1 Holographic method 65
3.1.2 Phase mask method 67
3.2 The phase mask dithering/moving technique 70
3.2.1 Experimental setup description 71
3.2.2 Developed software description 73
3.2.3 Basic calibrations 76
3.3 Conclusion 83

4 Fabrication and characterization of Bragg gratings 85
4.1 Introduction 85
4.2 Characterization of Bragg gratings 85
4.3 Preliminary setup calibrations and Bragg grating studies 87
4.3.1 Phase mask dithering amplitude variation 88
4.3.2 Beam scanning velocity variation 90
4.3.3 Writing UV beam power variation 92
4.3.4 Grating length variation 94
4.3.5 High reflective fiber Bragg gratings 94
4.4 Apodized fiber Bragg gratings 96
4.4.1 Direct spatial profile functions 97

4.4.2 Modelled spatial profiles 98
4.5 Chirped fiber Bragg gratings 101
4.6 Phase shifted fiber Bragg gratings 104
4.7 Sampled fiber Bragg gratings 107
4.8 Bragg gratings on planar devices 110
4.8.1 Experimental setup conversion and waveguide alignments 110
4.8.2 Apodized Bragg gratings in straight waveguides and MZIs 112
4.9 Conclusion 115
5 Conclusions 117
5.1 Final considerations and evaluation of the developed work 117
5.2 Suggestions for future work 119
Bibliography 121

List of Figures

Figure 2.1 – Refractive index modulation in the core of a fiber along z, with varying visibility of the fringe pattern……... 30

Figure 2.2 – Diffraction of a light wave by a grating…… 31

Figure 2.3 – Illustration of fiber Bragg grating properties…… 32

Figure 2.4 – Reflection spectra of three uniform gratings (L=10mm) versus wavelength for Bragg reflection for kL=2 (dot), kL=5 (dash) and kL=8 (solid)……. 41

Figure 2.5 – Reflectivity versus k_{ac} and modulated index change, Δn, for grating lengths of 5, 10, 20, 30 and 40 mm (λ=1550nm and η=1)……... 43

Figure 2.6 – Bandwidth as a function of (a) the grating length and (b) k_{ac} or modulated index change considering the limits for weak and strong gratings, respectively (λ=1550nm, n_{eff}=1.45 and η=1)……... 44

Figure 2.7 – Group delay of three uniform gratings (L=10mm) versus wavelength for kL=2 (dot), kL=5 (dash) and kL=8 (solid)…….. 46

Figure 2.8 – Representation of the input and output fields in the refractive index modulation for a small section of the grating…….. 47

Figure 2.9 – Different apodization profiles described in equations (2.67) to (2.70)……... 52

Figure 2.10 – Variation of the refractive index change along the grating for a (a) Gaussian, (b) raisedcosine, (c) sinc, (d) Hamming and (e) Blackman profile, with constant-dc index change……. 53

Figure 2.11 – Reflectivity spectrum of three apodized Bragg gratings with Gaussian, raisedcosine and sinc apodization profiles…….. 53

Figure 2.12 – Close-up view of the edges of the three apodized gratings shown in Figure 2.11 compared with a uniform Bragg grating……... 54

Figure 2.13 – Illustration and principle of operation of a chirped fiber Bragg grating structure……... 55

Figure 2.14 –Non-uniform variation (a) of the refractive index modulation and (b) of the grating period along the grating length……... 55

Figure 2.15 – Reflectivity and delay spectrum of chirped Bragg gratings…….. 56

Figure 2.16 – Illustration of a π-shifted fiber Bragg grating structure……... 57

Figure 2.17 – Simulated spectra of phase-shifted fiber Bragg grating structures for three different phase steps applied in the center of the grating…….. 58

Figure 2.18 – Illustration of three different phase stepped gratings along the grating length with (a) two π-phase shifts introduced at L/4 and 3L/4; (b) two π-phase shifts introduced at L/3 and 2L/3; and (c) three π-phase shifts introduced at L/4, L/2 and 3L/4…… 58

Figure 2.19 – Sampled Bragg grating superstructure and associated spatial frequencies……... 60

Figure 2.20 – Photoionization process of the GeO center, resulting in the release of an electron to the conduction band and in the formation of a GeE' center…….. 62

Figure 3.1 – UV interferometer for writing Bragg gratings……... 66

Figure 3.2 – Schematic diagram of the phase mask method……. 67

Figure 3.3 – Phase mask used as beam splitter……. 69

Figure 3.4 – Experimental setup for fibre/planar waveguide gratings photoinscription……..... 71

Figure 3.5 – Photograph of the laboratory showing the experimental setup for fiber gratings photoinscription…….. 73

Figure 3.6 – Control panel of the LabView™ based program developed for the experimental setup control……..... 74

Figure 3.7 – Variation of fringe visibility with dither amplitude (in units of the grating period) for a square and a triangular carrier function……... 78

Figure 3.8 – Dither amplitude (in units of the grating period) as a function of the normalized modulation index for a square and a triangular carrier function……... 79

Figure 3.9 – PZT calibration curve…….. 80

Figure 3.10 – Acousto-optic cell calibration curve……..... 81

Figure 3.11 – Example of implementation of the Gaussian apodization profile using the required calibrations…….. 82

Figure 3.12 – Application of the example of Figure 3.11 in the LabView™ system control software…... 83

Figure 4.1 – Experimental setup for spectral characterization of Bragg gratings using (a) a broadband source and an OSA; and (b) a tunable laser source and an optical power meter for high resolution measurements…….. 86

Figure 4.2 – Experimental setup for chromatic dispersion measurements by the modulated phase-shift method……..... 87

Figure 4.3 – 30 mm long uniform fiber Bragg gratings fabricated with different phase mask dithering amplitudes……... 88

Figure 4.4 – Corrections to the writing system to compensate bad mechanical response of the PZT/phase mask holder by (a) introducing and arbitrary PZT driven function and by (b) introducing a correction factor to the PZT calibration curve(α is the correction factor which has a value of 0.13)…… 89

Figure 4.5 – 30 mm long uniform fiber Bragg gratings fabricated with different phase mask dithering, with software corrections and an arbitrary PZT carrier function…….. 90

Figure 4.6 – Direct comparison of two fiber Bragg gratings written with zero visibility before and after corrections were made to the writing system……..... 90

Figure 4.7 – Grating reflectivity versus beam scanning velocity…….….. 91

Figure 4.8 – Reflectivity versus k_{ac} and modulated index change, Δn, for the 30 mm gratings with peak reflectivities plotted in Figure 4.7 (λ_B=1532nm and η=0.75)…….…….. 92

Figure 4.9 – Grating reflectivity versus cell efficiency (or writing power)……. 93

Figure 4.10 – Reflectivity versus k_{ac} and modulated index change, Δn, for the 30 mm gratings with peak reflectivities plotted in Figure 4.9 (λ_B=1532nm and η=0.75)……... 93

Figure 4.11 – Normalized grating reflectivity versus grating length…….. 94

Figure 4.12 – Experimental results of high reflective fiber Bragg grating showing (a) reflection and transmission in normalized linear scale and (b) transmission in logarithmic scale……. 95

Figure 4.13 – Reduction of cladding mode resonances by using high NA fiber in high reflective fiber Bragg gratings…….. 96

Figure 4.14 – Experimental comparison of a uniform Bragg grating and a (a) Gaussian, a (b) raised cosine and a (c) sinc apodized Bragg grating…… 97

Figure 4.15 – Close-up view of the edges of the three apodized and the uniform Bragg gratings shown in Figure 4.14……... 98

Figure 4.16 – Apodization spatial design#1 provided by TUHH……. 99

Figure 4.17 – Fiber Bragg gratings fabricated using the spatial profile shown in Figure 4.16 presenting reflectivities of (a) 78 % and (b) 99 %…….. 99

Figure 4.18 – Measured magnitude of k_{dc} (z) of the grating of Figure 4.17-a) using optical frequency domain reflectometry (OFDR)…… 100

Figure 4.19 – Apodization spatial design#2 provided by TUHH……. 100

Figure 4.20 – High reflectivity apodized fiber Bragg gratings using the spatial profile of Figure 4.19…... 101

Figure 4.21 – Wavelength shift by the moving phase mask/ scanning beam technique…… 102

Figure 4.22 – Spectra of chirped fiber Bragg gratings fabricated by simultaneous phase mask movement and beam scanning. The spectra were obtained when the phase mask and beam move (a) in opposite directions (*negative chirp*), (b) in the same direction (*positive chirp*), and (c) in both (double exposure)…… 103

Figure 4.23 – Measured reflection spectra and group delay of a positive chirped fiber Bragg grating…... 104

Figure 4.24 – Experimental and simulation of a π-shift fiber Bragg grating……. 105

Figure 4.25 – Fine control of π-shift fiber Bragg gratings by changing PZT driven voltage by 1 mV, corresponding to a spatial shift difference of 15 nm……..... 106

Figure 4.26 – Transmission and reflection spectrums of 10 mm long fabricated fiber Bragg gratings with a (a) π/2, a (b) π and a (c) 3π/2 phase shift……. 106

Figure 4.27 – Measured reflection spectra and group delay of a π–shift fiber Bragg grating……. 107

Figure 4.28 – Sampled fiber Bragg gratings fabricated by amplitude modulation through acousto optic cell efficiency variation (0, 85 %, 0, 85 %, …) with a sampling period of (a) 250 μm and (b) 500 μm….. 108

Figure 4.29 – Sampled fiber Bragg grating fabricated by amplitude modulation through phase mask dithering variation (visibility: 0, 1, 0, 1, …) with a sampling period of 500 μm……. 109

Figure 4.30 –Experimental results from sampled fiber Bragg gratings fabricated by phase modulation (0, π, 0, π, …) with a double exposure and different sampling periods…… 109

Figure 4.31 – Photograph of the experimental setup for planar waveguide gratings photoinscription….. 111

Figure 4.32 – CCD camera view of planar waveguide structures and waveguide fluorescence with UV laser beam incidence…… 112

Figure 4.33 – Spectral transmission and reflectivity of apodized Bragg gratings written in straight waveguides with scanning velocities of 10 mm/s and different UV laser powers……. 113

Figure 4.34 – Add-drop filter implementation based on a Mach-Zhender interferometer…… 114

Figure 4.35 – Reflected and transmitted signals from an integrated MZI when two equal apodized Bragg gratings were written on the interferometer arms, before UV trimming……. 114

Figure 4.36 – CCD camera view of a planar sample and a flat glass slide in parallelism when illuminated with a hydrogen lamp……... 115

1 Introduction

1.1 Motivation

Optical communication is one of the fields where a strong effort has been allocated into the research and development of new optical devices, driven mainly by the powerful telecom market. Full integration in optical fiber systems through all-optical components is therefore an advantage. One key element that has a strong impact in these components is the fiber Bragg grating (FBG). There are already many applications and components using Bragg gratings, either in fiber and planar technology. Optical filtering, add-drop multiplexing, dispersion compensation, switching, routing and fiber lasers and amplifiers are examples of some of the current applications. Another useful and interesting application of Bragg gratings is in optical sensing. This growing market makes use of these elements mainly as sensing heads, due to its sensitivity to various physical parameters (temperature and strain are some examples).

An important issue of Bragg gratings is concerned, of course, with its fabrication. Several methods and experimental arrangements have been proposed, being divided in three main categories: holographic, phase mask and point-by-point. Each method has its own advantages and drawbacks, and the choice should be based in several factors like feasibility, reproducibility, writing time, flexibility, cost and available ultraviolet (UV) laser source. Also, the growing demand for customized Bragg gratings is an important aspect that should be taken into account when implementing new writing schemes. Therefore, the method chosen in this work makes use of the effectiveness of the phase mask method, introducing other control elements to allow the tailoring of Bragg grating structures. The phase mask dithering/moving technique allows, in this way, the combination of simplicity and high reproducibility with the desired flexibility.

The core of this work is the implementation and development of a system for special Bragg gratings fabrication in fiber and planar waveguides, based on the phase mask dithering/moving technique. The acquisition of this kind of facilities and competences is extremely important for a good positioning of any institution in this research field, since not only allows the production of tailored Bragg gratings, but also allows seeking opportunities in existing or new applications and in the integration of new devices.

1.2 Overview and state of the art

Bragg gratings are nowadays key components in optical systems, since they share the same advantages offered by the optical fibers, such as low loss transmission, immunity to electromagnetic interference and electrical isolation. The gratings are achieved through a periodic perturbation of the effective refractive index along the waveguide, which is formed by exposing it to an intense optical interference pattern. This was first demonstrated by Hill *et al.* in 1978 [1, 2], using an argon-ion laser (at 488 nm) launched in a germania – doped fiber; an increase of the reflected light intensity was observed with time, until almost all the light was reflected back; the modulation was created by a standing wave of radiation (visible) interference within the fiber core introduced from the end of the fiber.

This mechanism, called photosensitivity, is responsible for the creation of permanent changes in the refractive index by photo-induction. A Bragg grating behaves as a wavelength-selective filter, reflecting a narrow band of wavelengths while transmitting all others. This discover raised a lot of questions concerning the causes behind this phenomena and its dependence on the illumination light used. One of the first reported studies about grating formation indicated a two photon process as the main mechanism, showing that the grating strength increased with the square of the light intensity [3]. Some years later, in an experiment where the fiber was irradiated from the cladding side with two intersecting coherent ultraviolet light beams (at 244 nm, one half of the wavelength used in [1]), Meltz *et al.* [4] demonstrated that photosensitivity could be much more efficient if a single photon process was employed by using a wavelength in the vicinity of the 245 nm germania oxygen-vacancy defect band [5]. Moreover, the period of the interference maxima and the index change was set by the angle between the two interfering beams and the UV wavelength, rather than by the wavelength of the visible radiation which was launched into the fiber core. In this way, the formation of Bragg gratings operating at wavelengths above the one used for the illumination was demonstrated and enabled the properties of this device to be explored in the telecommunications spectral windows. The fact that the gratings could be written from the side of the fiber (externally inscribed) was a major breakthrough that turned this phenomenon from simple scientific curiosity to a mainstream tool.

Since then, significant progress has been made towards realizing various types and more efficient gratings. Advances in grating fabrication methods, having the phase mask approach as the best example [6], and fiber photosensitivity enhancement techniques (hydrogen loading) [7] have made it possible to fabricate a variety of index-modulated structures within the core of an optical fiber including the already mentioned standard uniform Bragg gratings [4, 6], π-phase shifted gratings [8], blazed or tilted gratings [9], chirped gratings [10] and long period gratings [11, 12].

Several techniques for the fabrication of Bragg gratings have been demonstrated, starting with the internal writing [1] and the holographic method [4], where two overlapping light beams produce a periodic interference pattern. Other interferometer methods based in the standard Talbot arrangement [13, 14] have been proposed, enabling grating inscription with a wide wavelength tunability. An adaptation to this arrangement has been proposed by Kashyap et al. [15, 16]; in this case, a phase mask is placed in the path of a normally incident UV beam to act as a beam splitter, and the ±1 orders are reflected off two mirrors to intersect at a fiber. The Bragg wavelength is tuned by rotation of the mirrors and the phase mask acts simply as a beam splitter.

Another fabrication method, but not very efficient and therefore not very used, is the point-by-point or single slit technique [17]. Each point (or each index perturbation) can be controlled in terms of UV dose and in terms of waveguide positioning when illuminated and so custom designs can be achieved. However, some disadvantages and restrictions must be addressed. First of all, it is extremely difficult to focus a "clean" slit of UV light of sub-micron dimensions, and so only higher order gratings (micro-Bragg gratings) have been reported to date for the typical near infrared wavelengths [18]. Secondly, the point-by-point method is a tediously long process.

The mostly used and attractive is the phase mask technique [6, 19-21], since it greatly simplifies the fabrication process, while yielding high performance gratings. When compared with the holographic technique, the phase mask method offers easier alignment of the waveguide, reduced stability requirements on the photoimprinting apparatus and lower coherence requirements on the ultraviolet laser beam. Therefore, this technique allows Bragg gratings to be written with relaxed tolerances on the coherence of the writing beam and with better repeatability. The main drawback is that the grating period, and consequently the Bragg wavelength, is imposed by the fixed phase mask period, requiring different masks for each different grating wavelength. However, some fine wavelength tuning (~2 nm) is possible when different mechanical tension levels are applied to the fiber during the photoinscription process.

Various types of Bragg gratings can be fabricated using the above mentioned methods. Desired spectral and dispersive characteristics can be achieved by varying numerous physical parameters like induced index change, length, periodicity and fringe tilt. In this way, special structures like apodized, chirped, phase shifted and sampled gratings can be fabricated, instead of the standard uniform Bragg gratings. Most of the designed gratings for practical applications are not uniform.

The use of a standard uniform phase mask for grating fabrication results in a uniform refractive index modulation along the grating length, and in expected strong side lobes in the

spectral response of Bragg gratings, undesirable in many applications like wavelength division multiplexing (WDM). The suppression of these secondary maxima can be achieved if the profile of the index modulation along the grating length is a given bell-like functional shape [22]. This procedure, called apodization, have been extensively studied and demonstrated [23-26]. Although apodization can be achieved simply by varying the intensity of the UV writing beam along the grating length, the accompanying variation in the average refractive index induces an undesired chirp that needs to be compensated by another exposure step through an amplitude mask [24]. Alternatively, complex phase masks with variable diffraction efficiency can be used to produce pure apodization [25, 27], or techniques based on periodic fiber stretching while being exposed [28]. Another approach is the moving fiber/scanning beam, where pure apodization is achieved by the application of a variable dither to the fiber during the photoinscription process [29, 30]. This technique has the major advantage of inducing a constant average refractive index change, since the average UV fluence is constant along the grating length. It also enables the creation of more complex structures, like chirped and phase shifted gratings, by executing a proper movement of the fiber while the beam scanning is being performed [30].

Chirped gratings have attracted a lot of interest, since they were recognized as important and reliable structures for dispersion compensation [31-34], becoming an alternative to long lengths of dispersion compensation fiber (DCF). This chirp behavior is a consequence of varying the grating period or the effective refractive index change along the FBG length. Several techniques for fabricating chirped gratings were demonstrated based on temperature and strain gradients [35-38], by curving or tilting the fiber [10, 39, 40], but also writing FBGs in tapered core fibers [10, 41-43]. These structures can also be used as strain sensing elements [44, 45] and as part of interrogation schemes [46].

Phase shifted gratings are precise complex structures and their working principle was first demonstrated by Alferness *et al.* [47] in periodic structures made from semiconductor materials, where a phase shift was introduced by etching a larger spacing at the center of the device, forming the basis of single mode phase shifted semiconductor Distributed Feedback (DFB) lasers [48]. Similar devices in optical fibers can be created by raising the general refractive index at a certain region in the fiber grating through irradiation with UV light, and was firstly demonstrated by Canning et al. [8]. In this experience, such post-processing produces two gratings out of phase with each other which act as a wavelength selective Fabry-Perot resonator, allowing light at the resonance to penetrate the stop band of the original grating. The resonance wavelength depends on the size of the phase change. Discrete phase shifts are normally used to open extremely narrow transmission resonances in a reflection grating or to tailor the passive filter shape. The most well known application of discrete phase shifts is the use of a "quarter-

wave" or π-shift in the center of a distributed-feedback laser. Among these post-processing fabrication techniques [49], other alternatives usually involve the translation of an interferogram by the desired phase shift. This can be achieved by scanning the beam or optical fiber and introducing a desired mismatch between system velocities, during modulation of the UV amplitude [29], or by shifting the interferogram independently, either by dithering or translation of an optical phase mask [29, 50] and combinations thereof. Other techniques exploit two beam interference methods through an optical phase mask, either by using two separate beams [51] or two overlapped but oppositely tilted polarized beams out of phase with each other [52, 53]. Based on the latter arrangements, phase-shifts were efficiently induced during the inscription process without requiring a spatial resolution below the phase-shift [54].

More complex structures are the sampled or superstructure Bragg gratings, which are generated by a periodic modulation of the refractive index amplitude and/or phase in the waveguide. The resultant reflection spectrum and channel separation is a function of the shape and period of this modulation. The sampled grating is a conventional grating at the appropriate wavelength multiplied by a sampling function. Therefore, the spatial frequency content of these superstructures can be approximated by a comb of delta functions centered at the Bragg frequency. Most of the already reported sampled Bragg gratings use simple binary sampling functions, simply by modulating the intensity of the UV beam while translating it along a fiber and phase mask assembly [55-57]. Other fabrication approaches, seeking performance improvement have also been reported, like, for example, the one that uses a sinc-shaped sampling function that causes the overall envelope to be square, ensuring that the individual sections are concatenated, thereby guarantying a continuously alternating refractive index amplitude and phase profile [58]; other approach uses a multiple phase shift sampled Bragg grating that can realize the same bandwidth and density as conventional sampled Bragg gratings in a much shorter length, enabling dense channel spacing without increasing the spacing of the Bragg grating [59].

The range of applications of Bragg gratings is very broad in the fields of optical communications and optical sensing. Some examples will be explored in more detail in the next paragraphs, but a summary of Bragg gratings in some concrete applications can be found in Table 1. The summary gives a perspective of the developments in the last 10 to 15 years of application of these structures to specific purposes.

Table 1

Applications of Bragg gratings in optical communications and sensors

APPLICATION	REFERENCES
Optical Communications	
Pump laser wavelength stabilizer	[60-63]
Dispersion compensation	[31, 32]; [64-68]
Wavelength selective devices	
Filtering, Multiplexing/Demultiplexing	[69-78]
Fiber lasers	[79-95]
Erbium doped fiber amplifiers	[91-95]
Optical Fiber Sensors	
Measurement of:	
Strain / temperature	[96-105]
Displacement / temperature	[106-109]
Curvature / temperature	[110-112]
Pressure / temperature	[113-115]
Refractive index / Salinity	[116, 117]
Acceleration	[118, 119]
Relative Humidity	[120]
Applied to:	
Civil structures	[121-124]
Medical applications	[125, 126]

In lightwave communications, gratings can be used from simple auxiliary components (as pump laser wavelength stabilizers) to network elements performing critical functions (in add/drop multiplexers). The most explored commercial applications of Bragg gratings until now have been as feedback mirrors in wavelength stabilized semiconductor lasers and as dispersion compensators. Grating stabilization for 980 nm and 1480 nm pump lasers for erbium doped fiber amplifiers are commonly deployed nowadays. Weak (reflectivities of 1-10 %) and narrow band

(reflection bandwidths of 0.2-3 nm) gratings are written in the fiber pigtail in order to couple light back into a Fabry-Perot pump laser, creating an external laser cavity. It prevents, in this way, significant risks to optimum amplifier performance from pump wavelength fluctuations arising from temperature and injection current variations, as well as from ageing. Chirped Bragg gratings for dispersion compensation should be operated in the reflection mode in order to equalize the dispersion of an optical pulse. As light pulse propagates down an optical fiber its width broadens because the longer wavelength light lags the light at a shorter wavelength, and, therefore, is said to be dispersed. As a consequence, at sufficiently high data rates and/or fiber lengths, the pulses in a data stream start to overlap, limiting the maximum data that can be transmitted through a fiber. If the longer wavelengths are reflected near the front of the grating, whereas the shorter wavelengths are reflected near the back, the shorter wavelengths are delayed relative to the longer ones. Therefore, chirped gratings can be designed so that all wavelengths in the light pulse exit the reflector at the same time, equalizing the dispersion in the optical pulse. Other examples using standard uniform and specialty Bragg gratings, as in add/drop multiplexing for WDM, fiber lasers including linear, ring and distributed feedback cavities, band rejection filters, mode converters, gain equalization or clamping in fiber amplifiers are presented in Table 1.

Apart from optical telecommunications, the most promising application of Bragg gratings is in the field of optical fiber sensors. Advantages of optical fiber sensing are well known and have been widely demonstrated in the literature on this subject. However, until now, fiber sensors have resulted in relatively few real commercial successes, and the technology remains in many instances, laboratory-based at the prototype stage. The main reason for this is that many fiber optic sensors were developed to replace existing conventional electro-mechanical sensor systems, which are well established, have proven reliability records and manufacturing costs. Thus, even though fiber sensors offer important advantages such as electrically passive operation, electromagnetic interference immunity, high sensitivity, and multiplexing capabilities, market penetration of this technology has been slow to develop. In applications where fiber sensors offer new capabilities, however, such as distributed sensing, fiber sensors appear to have a distinct edge over the competition. In this way, fiber Bragg gratings and other grating-based devices are examples of the type of sensors which provide this capability. These intrinsic sensing elements have an inherent self-referencing capability and are easily multiplexed in a serial fashion along the fiber length. The most typical measurands that can be measured by fibre Bragg gratings are temperature and strain, either independently or simultaneously. Fiber gratings exhibit a well-behaved wavelength response to these physical parameters reflected in its Bragg wavelength shift when deformed or when it experiences thermal changes. Also, their typical high reflectivity (>75%) offers a sufficient amount of optical power for detection in photodiodes, giving fibre

Bragg grating sensors a unique Bragg wavelength that is independent of the optical intensity used in the system. But the range application of Bragg gratings as sensing elements is very broad and not restricted to applications where strain and temperature measurements are required, like when they are embedded in materials, creating "smart structures" from which the health of civil structures can be assessed and tracked in a real time basis. They present also advantageous features in areas like medicine, gas, pressure and chemical sensing in adequate optical sensor configurations.

Apart from the literature already referenced, it is important to mention that there are also several review papers [127-136] and some books [137-140] specially dedicated to the fundamentals, fabrication methods, different types and applications of Bragg gratings, which, by itself, indicate the big interest that this devices have been raising in the last years.

1.3 Thesis content

This thesis is composed of five chapters, starting with an introduction to the theme and the theoretical aspects involving Bragg gratings. It is followed by a description of the experimental work performed, presenting results for Bragg grating inscription in fiber and planar waveguides. It finalizes with a conclusion that includes suggestions for future work.

The detailed structure of this thesis is as follows:

Chapter 1 describes the initial motivations for the development of the work described in the thesis and makes an overview about Bragg gratings. The section *Overview and state of the art*, introduces the reader how these devices where first discovered and why they became so attractive for researchers. It also describes the most used methods for its fabrication, stating only some of the advantages and disadvantages of each, without much detail, introducing then various types of gratings and techniques to fabricate them. Finally, some of the applications of Bragg gratings are described. It is the intention of the author to indicate paths in the published literature, so that the reader can easily find more detailed information.

Chapter 2 describes the theory and mechanisms behind Bragg gratings formation and operation in optical waveguides. Particular attention is then dedicated to gratings with special characteristics, like apodized, chirped, phase shifted and sampled. Grating modelling using the transfer matrix method introduces the reader to the expected spectral and temporal responses of the several types of gratings.

Chapter 3 starts by describing in detail the Bragg grating fabrication methods mentioned in chapter 1. The phase mask dithering/moving technique used in this work is introduced, starting by the experimental setup implemented and the developed software. All the calibrations needed in order to implement this technique are also described.

Chapter 4 presents the results achieved by this fabrication setup, including the calibration studies for phase mask dithering amplitude, beam scanning velocity and UV beam power variations, as well as the demonstration of some of the setup capabilities in terms of grating fabrication. Apodized with different spatial apodization profiles, chirped, phase shifted and sampled fiber Bragg gratings are some examples of gratings presented in this chapter. Chapter 4 is also dedicated to the writing of Bragg gratings in planar waveguides using the proposed technique. A modification of the setup to support this kind of structure is presented, as well as the major alignment concerns regarding the inscription in these waveguides. Examples of apodized Bragg gratings written in this planar structures (waveguides and in the arms of Mach-Zhender interferometers) are shown.

Chapter 5 concludes the thesis with a discussion and evaluation of the main results achieved in this work. Suggestions for future work are also given.

2 Theory of Bragg gratings

2.1 Introduction

Good understanding of Bragg grating working principles and properties is essential for the theoretical design of these devices. It is also crucial to know some fundamental issues related with the spectral and temporal response when some specific spatial profile is implemented, and for that computer simulation tools based on wave propagation analysis are usually used. This is especially true if the purpose is to fabricate the gratings.

This chapter describes the basic theory of Bragg gratings, starting by a review of the fundamental properties. The results derived from the coupled mode theory are briefly presented, together with a common numerical technique for computing the spectral and temporal response of these devices, the transfer matrix method. Several types of Bragg gratings with different transfer functions that depend on the induced refractive index modulation profile are then presented. Along with this, the main principles and mechanisms behind the phenomenon of photosensitivity, as well as some photosensitivity enhancement methods are introduced.

2.2 Bragg grating fundamentals

A Bragg grating is a periodic perturbation of the refractive index along the waveguide formed by exposure to an intense ultraviolet optical interference pattern. For example, in an optical fiber, the exposure induces a permanent refractive index change in the core of the fiber, by the already mentioned mechanism of photosensitivity. This resulting variation of the effective refractive index, n_{eff}, of the guided mode along an optical fiber axis, z, can be described by [129]

$$\delta n_{eff}(z) = \overline{\Delta n}(z)\left\{1 + \nu \cos\left[\frac{2\pi}{\Lambda} z + \varphi(z)\right]\right\} \tag{2.1}$$

where $\overline{\Delta n}$ is the "dc" index change spatially averaged over a grating period, ν is the "fringe visibility" of the index change, Λ is the nominal grating period, and $\varphi(z)$ describes grating chirp. Therefore, the effective refractive index for each grating position can be described by

$n_{eff}(z) = n_{eff}^0 + \delta n_{eff}(z)$, where n_{eff}^0 is the effective refractive index of the guided mode without any UV induced perturbation.

This modulation pattern is represented in Figure 2.1 for different "fringe visibility" and no chirp, representing the standard modulation of a uniform Bragg grating. As it can be seen, visibility has a strong impact in the amplitude of the index change, and consequently in the reflectivity of the grating, as it will be demonstrated in the next section. In this case, the unperturbed core-to-cladding refractive index difference is 5×10^{-3}, while the maximum refractive index amplitude modulation for unity visibility is 2×10^{-3}. By introducing chirp, the modulation period can be changed along the grating.

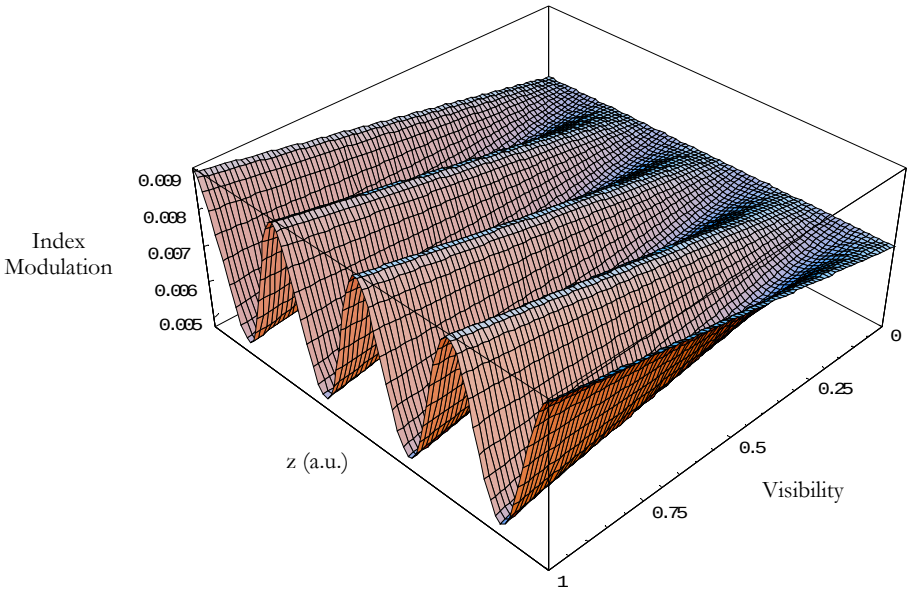

Figure 2.1 – Refractive index modulation in the core of a fiber along z, with varying visibility of the fringe pattern.

A combination of one or both of these features, visibility and chirp, along the grating length can result in more complex structures, like apodized and/or chirped gratings, originating desired spectral and temporal responses. Therefore, the optical properties of Bragg gratings are essentially determined by the variation of the induced index change, δn_{eff} , along the fiber axis, z.

The working principle of a fiber Bragg grating can be understood by simply considering it as an optical diffraction element, and thus its effect upon an incident light wave. A diffraction grating may be defined as any refractive index arrangement which imposes a periodic variation of amplitude or phase, or both, on an incident wave.

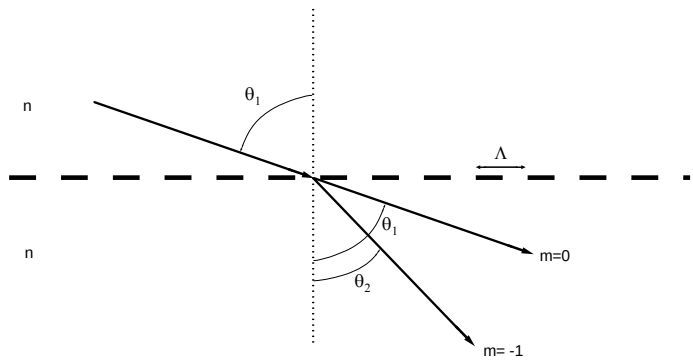

Figure 2.2 – Diffraction of a light wave by a grating.

Considering Figure 2.2, an incident wave at an angle θ_1 can suffer a change described by the grating equation [141],

$$n \ \sin\theta_2 = n \ \sin\theta_1 + m\frac{\lambda}{\Lambda}, \quad m = 0, \pm 1, \pm 2, ..., \tag{2.2}$$

where θ_2 is the angle of the diffracted wave and the integer m determines the diffraction order, or the order of interference. Despite from the fact that (2.2) predicts only the directions θ_2 at which constructive interference occurs, it is also capable of determining the wavelength at which a fiber grating most efficiently couples light between two modes. In Bragg gratings (also called reflection or short-period gratings) coupling occurs between modes traveling in opposite directions and so the mode traveling in the opposite direction should have a bounce angle $\theta_2 = -\theta_1$. Since the mode propagation constant β is given by

$$\beta = \frac{2\pi}{\lambda} n_{eff}, \tag{2.3}$$

where $n_{eff} = n \ \sin\theta$, equation 2.2 may be rewritten for guided modes as

$$\beta_2 = \beta_1 + m\frac{2\pi}{\Lambda} \quad . \tag{2.4}$$

Taking into account that for first-order diffraction, which usually dominates in a fiber grating, m = -1, and using (2.3) in (2.4), it is easily found that the resonant wavelength for coupling from a mode of index $n_{eff,1}$ into a mode of index $n_{eff,2}$ is

$$\lambda = \left(n_{eff,1} + n_{eff,2}\right)\Lambda \quad . \tag{2.5}$$

If the two modes are identical, the result is the well known equation for Bragg reflection:

$$\lambda_B = 2n_{eff}\Lambda \tag{2.6}$$

A small amount of incident light is reflected at each periodic refractive index change. The entire reflected light waves are combined into one large reflection at a particular wavelength when the strongest mode coupling occurs. This is referred to as the Bragg condition (2.6), and the wavelength at which this reflection occurs is called the Bragg wavelength, λ_B. When the Bragg condition is satisfied, the contributions of reflected light from each grating plane add constructively in the backward direction to form a back-reflected peak with a centre wavelength defined by the grating parameters. The Bragg grating is essentially transparent for incident light at wavelengths other than the Bragg wavelength, where phase matching between the incident and reflected beams do not occur. An illustration of a Bragg grating in an optical fiber representing those properties is drawn in Figure 2.3.

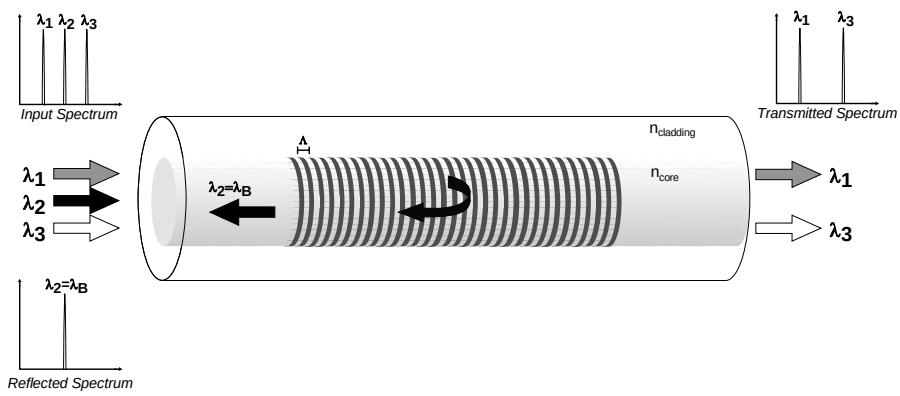

Figure 2.3 – Illustration of fiber Bragg grating properties.

As it can be seen from Figure 2.3, the wavelength λ_2 tuned to the grating Bragg wavelength ($\lambda_2=\lambda_B$) is reflected (from a few percent up to more than 99.9%, depending on the grating strength) while the other wavelengths are totally transmitted.

In resume, fiber Bragg gratings can be formed by a series of planes characterized by an index of refraction different from the one of the regular fiber core. Light propagating in the core will be reflected by the interfaces between regions having different refractive indices. But the reflected light

is generally out of phase and vanishes. However, for a certain wavelength, the Bragg wavelength (λ_B), the light reflected by the periodically varying index of refraction will be in equal phase and added constructively. This results in a characteristic depression in the transmission spectrum as well as in a peak in the reflection spectrum, when illuminated by a broadband source. Such spectral response will be explored in detail in the next section.

2.3 Coupled mode theory

The relation between the gratings structure and their spectral characteristics can be determined using the coupled mode theory. Coupled mode theory is straightforward, intuitive, and it accurately models the optical properties of most gratings of interest and can be found in a large number of texts; detailed analysis can be found in [129, 138, 142-147].

The solutions provided by solving Maxwell's equations with appropriate boundary conditions when considering wave propagation in optical fibers give the basic field distributions of the bound and radiation modes of the waveguide. These modes propagate without coupling in the absence of any perturbation. But coupling can occur between specific propagating modes if the waveguide has a periodic phase and/or amplitude perturbation with a "phase/amplitude-constant" close to the sum or difference between the propagation constants of the modes. It is here that coupled mode theory appears, solving this kind of problems. This technique assumes that the mode fields of an unperturbed waveguide remain unchanged in the presence of weak perturbations, providing a set of first-order differential equations for the change in the amplitude of the fields along the fiber.

In this section, only the most relevant results will be presented, derived from a detailed analysis that can be found in the references already indicated. It follows closely the study and the notation used in [138].

In order to derive the coupled mode equations, effects of the perturbation have to be included in the unperturbed wave equation. Assuming that wave propagation takes place in a perturbed system with a dielectric grating, the total polarization response of the dielectric medium can be separated into two terms, unperturbed and perturbed polarization,

$$\overline{P} = \overline{P}_{unpert} + \overline{P}_{grating} \tag{2.7}$$

where

$$\overline{P}_{unpert} = \varepsilon_0 \chi^{(1)} \overline{E}_{\mu} \tag{2.8}$$

being ε_0 the dielectric constant, $\chi^{(1)}$ the linear susceptibility and $\overline{E}_\mu$ the applied electric field. Substituting (2.7) in the wave equation given by,

$$\nabla^2 \overline{E} = \mu_0 \varepsilon_0 \frac{\partial^2 \overline{E}}{\partial t^2} + \mu_0 \frac{\partial^2 \overline{P}}{\partial t^2} \tag{2.9}$$

results in

$$\nabla^2 E_{\mu t} = \mu_0 \varepsilon_0 \varepsilon_r \frac{\partial^2}{\partial t^2} E_{\mu t} + \mu_0 \frac{\partial^2}{\partial t^2} P_{grating,\mu} \tag{2.10}$$

where μ_0 is the magnetic permeability, ε_r is the relative permittivity of the unperturbed core and the subscripts refers to the transverse, *t*, mode number, μ.

After some treatment, that includes the introduction of the guided modes of the optical fiber into the wave equation (the modes of an optical fiber can be described as a summation of *l* transverse guided mode amplitudes, $A_\mu(z)$, along with a continuum of radiation modes, $A_\rho(z)$, with corresponding propagation constants β_μ and β_ρ [145]), one can reach the transformed wave equation that describes a variety of phenomena in the coupling of modes

$$\sum_{\mu=1}^{\mu=l} \left[-2iw\mu_0 \frac{\partial A_\mu}{\partial z} e^{i(wt-\beta_\mu z)} + cc \right] = \int_{-\infty}^{+\infty}\int_{-\infty}^{+\infty} \mu_0 \frac{\partial^2}{\partial t^2} P_{grating,t} \xi_{\mu t}^* dxdy \tag{2.11}$$

where $\xi_{\mu t}$ is radial transverse field distribution of the μth guided mode.

Equation (2.11) applies to a set of forward and backward propagating modes, becoming now clearer how mode coupling occurs. The total transverse field may be described as a sum of both fields, not necessarily composed of the same mode order

$$E_t = \frac{1}{2}\left(A_\upsilon \xi_{\upsilon t} e^{i(wt-\beta_\upsilon z)} + cc + B_\mu \xi_{\mu t} e^{i(wt+\beta_\mu z)} + cc \right) \tag{2.12}$$

$$H_t = \frac{1}{2}\left(A_\upsilon H_{\upsilon t} e^{i(wt-\beta_\upsilon z)} + cc - B_\mu H_{\mu t} e^{i(wt+\beta_\mu z)} - cc \right) \tag{2.13}$$

The negative sign in the exponent signifies the forward and the positive sign the backward propagating mode, respectively. The modes of a waveguide form an orthogonal set, which in an ideal fiber will not couple unless there is a perturbation. Using (2.12) and (2.13) in (2.11) leads to

$$\left[\frac{\partial A_\upsilon}{\partial z}e^{i(wt-\beta_\upsilon z)}+cc\right]-\left[\frac{\partial B_\mu}{\partial z}e^{i(wt+\beta_\mu z)}+cc\right]=+\frac{i}{2w}\int_{-\infty}^{+\infty}\int_{-\infty}^{+\infty}\frac{\partial^2}{\partial t^2}P_{grating,t}\xi^*_{\mu,\upsilon t}dxdy \tag{2.14}$$

Considering now a spatially periodic refractive index modulation in a medium in which the dielectric constant varies periodically along the wave propagation direction, the total polarization can be defined with the perturbed permittivity, $\Delta\varepsilon(z)$ and the applied field as

$$P=\varepsilon_0\left[\varepsilon_r-1+\Delta\varepsilon(z)\right]E_\mu \tag{2.15}$$

where the terms in parentheses are equivalent to $\chi^{(1)}$ of (2.8). The constitutive relations between the permittivity of a material and the refractive index, n, result in the perturbation modulation index being derived from $n^2=\varepsilon_r$, so that

$$\left[n+\delta n(z)\right]^2=\varepsilon_r+\Delta\varepsilon(z) \tag{2.16}$$

Considering the perturbation to be a small fraction of the base refractive index ($\delta n << n$), results in

$$\Delta\varepsilon(z)\approx 2n\delta n(z) \tag{2.17}$$

Introducing now the spatially periodic sinusoidal refractive index modulation defined in (2.1), results in the expression for the total material polarization which is given by

$$P=\varepsilon_0\left\{n^2-1+2n\overline{\Delta n}\left[1+\frac{\nu}{2}\left(e^{i[(2\pi N/\Lambda)z+\phi(z)]}+cc\right)\right]\right\}E_\mu \tag{2.18}$$

where the exponent term along with the complex conjugate cc describe the real periodic modulation in complex notation and N is an integer ($-\infty<N<+\infty$) that signifies its harmonic order. The first term on the right hand side of equation (2.18) is the permittivity, the second term is the "dc" refractive index change, and the third term is the "ac" refractive index modulation. Incorporating

now the visibility in terms of $\Delta n = \nu \overline{\Delta n}$ as the amplitude of the "ac" refractive index modulation, the perturbed polarization can be described by

$$P_{pert} = 2n\varepsilon_0 \left[\overline{\Delta n} + \frac{\Delta n}{2} \left(e^{i[(2\pi N/\Lambda)z+\phi(z)]} + cc \right) \right] E_\mu \tag{2.19}$$

Including (2.19) in (2.14) results in

$$\begin{aligned} &\left[\frac{\partial A_\upsilon}{\partial z} e^{i(wt-\beta_\upsilon z)} + cc \right] - \left[\frac{\partial B_\mu}{\partial z} e^{i(wt+\beta_\mu z)} + cc \right] \\ &= -inw\varepsilon_0 A_\upsilon \int_{-\infty}^{+\infty}\int_{-\infty}^{+\infty} \left[\overline{\Delta n} + \frac{\Delta n}{2} \left(e^{i[(2\pi N/\Lambda)z+\phi(z)]} + cc \right) \right] \xi_{\upsilon t} e^{i(wt-\beta_\upsilon z)} \xi^*_{\mu,\upsilon t} dxdy \\ &\quad - inw\varepsilon_0 B_\mu \int_{-\infty}^{+\infty}\int_{-\infty}^{+\infty} \left[\overline{\Delta n} + \frac{\Delta n}{2} \left(e^{i[(2\pi N/\Lambda)z+\phi(z)]} + cc \right) \right] \xi_{\mu t} e^{i(wt+\beta_\mu z)} \xi^*_{\mu,\upsilon t} dxdy + cc \end{aligned} \tag{2.20}$$

On the left hand side of (2.20), the rate of variation of A_υ and B_μ is determined by the mode order μ or υ of the electric field $\xi^*_{\mu,\upsilon t}$ chosen as the multiplier according to the orthogonality relationship, as shown in equation (2.11) for the case of the single field. The right hand side has two generic components for both A and B modes as

$$\begin{aligned} &- inw\varepsilon_0 B_\mu e^{i(wt+\beta_\mu z)} \times \int_{-\infty}^{+\infty}\int_{-\infty}^{+\infty} \overline{\Delta n} \xi_{\mu t} \xi^*_{\mu t} dxdy \\ &- inw\varepsilon_0 A_\upsilon e^{i(wt-\beta_p z+\phi(z))} \times \int_{-\infty}^{+\infty}\int_{-\infty}^{+\infty} \frac{\Delta n}{2} \xi_{\upsilon t} \xi^*_{\mu t} dxdy + cc \end{aligned} \tag{2.21}$$

where the first exponent must agree with the exponent of the generated field on the left hand side of (2.20) and has a dependence on the "dc" refractive index change. The reason is that any other phase velocity dependence (as for other coupled mode) will not remain in synchronism with the generated wave. The second term has two parts; the first is dependent on the phase synchronous factor,

$$\beta_p = \frac{2\pi N}{\Lambda} \pm \beta_\upsilon \tag{2.22}$$

The mode interactions that can take place are determined by the right hand sides of (2.20) and (2.21). There are two important aspects that need to be taken into account: first, conservation of momentum (also known as phase matching) requires that the phase constants on the left hand side and the right hand side of (2.21) to be identical [equation (2.22)] and so this influences the coupling between copropagating and counterpropagating modes. Secondly, the transverse integral on the right hand side of (2.21), which is simply the overlap of the refractive index modulation profile and the distributions of the mode fields, determines the strength of the mode interactions.

In equation (2.22), the phase factor is the sum or difference between the magnitude of the driving electric field mode propagation constant β_υ and the phase factor of the perturbation. The resultant β_p is the phase constant of the induced polarization wave. This is the propagation constant of a bound wave generated by the polarization response of the material due to the presence of sources. To exist any significant transfer of energy from the driving field amplitude A to the generated fields on the left hand side of (2.21), the generated and the polarization waves must remain in phase over a significant distance, z. The phase matching condition (for a continuous transfer of energy) is described by

$$\beta_\mu = \beta_p \tag{2.23}$$

The phase mismatch is referred to as a detuning, and can be expressed by

$$\Delta\beta = \beta_\mu - \beta_p \tag{2.24}$$

Including (2.22) in (2.24), results in

$$\Delta\beta = \beta_\mu \pm \beta_\upsilon - \frac{2\pi N}{\Lambda} \tag{2.25}$$

If both β_υ and β_μ have identical (positive) signs, then the phase matching condition is satisfied ($\Delta\beta = 0$) for counterpropagating modes; if they have opposite signs, the interaction is between copropagating modes.

Therefore, considering that the phase matching condition is verified, equation (2.25) becomes

$$\beta_\upsilon = \pm\left(\frac{2\pi N}{\Lambda} - \beta_\mu\right) \tag{2.26}$$

In equation (2.26) it can be seen that a mode with a propagation constant of β_μ will synchronously drive another mode A_υ with a propagation constant of β_υ, provided, of course, that the latter is an allowed solution of the wave equation for guided modes and its equivalent for radiation modes.

Let's now consider the coupling of identical counterpropagating guided modes, the simplest form of interaction. For a general approach lets rewrite (2.20), where dissimilar modes are considered for the counterpropagating (reflected) mode phase matching

$$\begin{aligned}
&\frac{\partial B_\mu}{\partial z} e^{i(wt+\beta_\mu z)} + cc \\
&= inw\varepsilon_0 B_\mu \int_{-\infty}^{+\infty}\int_{-\infty}^{+\infty} \overline{\Delta n}\xi_{\mu t}\xi_{\mu t}^* e^{i(wt+\beta_\mu z)} dxdy \\
&\quad + inw\varepsilon_0 A_\upsilon \int_{-\infty}^{+\infty}\int_{-\infty}^{+\infty} \frac{\Delta n}{2} e^{i[(2\pi N/\Lambda)z+\phi(z)]}\xi_{\upsilon t}\xi_{\mu t}^* e^{i(wt-\beta_\upsilon z)} dxdy + cc
\end{aligned} \tag{2.27}$$

By choosing the appropriate β value for identical modes ($\mu = \upsilon$), but with opposite propagation directions, in (2.27) and dividing both sides by $\exp[i(wt + \beta_\mu z)]$ results in

$$\begin{aligned}
\frac{\partial B_\mu}{\partial z} &= inw\varepsilon_0 B_\mu \int_{-\infty}^{+\infty}\int_{-\infty}^{+\infty} \overline{\Delta n}\xi_{\mu t}\xi_{\mu t}^* dxdy \\
&\quad + inw\varepsilon_0 A_\upsilon \int_{-\infty}^{+\infty}\int_{-\infty}^{+\infty} \frac{\Delta n}{2} e^{i([(2\pi N/\Lambda)-\beta_\upsilon-\beta_\mu]z+\phi(z))}\xi_{\upsilon t}\xi_{\mu t}^* e^{i(wt-\beta_\upsilon z)} dxdy
\end{aligned} \tag{2.28}$$

which leads to the following simple coupled mode equations by choosing the appropriate synchronous terms,

$$\frac{\partial B_\mu}{\partial z} = ik_{dc}B_\mu + ik_{ac}A_\upsilon e^{-i(\Delta\beta z-\phi(z))} \tag{2.29}$$

with

$$\Delta\beta = \beta_\mu + \beta_\upsilon - \frac{2\pi N}{\Lambda} \tag{2.30}$$

The "dc" and "ac" coupling constants, k_{dc} and k_{ac}, are given, respectively, by

$$k_{dc} = nw\varepsilon_0 \int_{-\infty}^{+\infty}\int_{-\infty}^{+\infty} \overline{\Delta n}\xi_{\mu t}\xi_{\mu t}^* dxdy \tag{2.31}$$

$$\begin{aligned} k_{ac} &= nw\varepsilon_0 \int_{-\infty}^{+\infty}\int_{-\infty}^{+\infty} \frac{\Delta n}{2}\xi_{\upsilon t}\xi_{\mu t}^* dxdy \\ &= \frac{\nu}{2} k_{dc} \end{aligned} \tag{2.32}$$

where it was considered that $\mu = \upsilon$ and using $\Delta n = \nu\overline{\Delta n}$ in (2.32). The change in the amplitude of the driving mode may also be derived from (2.20) as

$$\frac{\partial A_\upsilon}{\partial z} = -ik_{dc}A_\upsilon - ik_{ac}^* B_\mu e^{-i(\Delta\beta z - \phi(z))} \tag{2.33}$$

Equations (2.29) and (2.33) are the coupled mode equations from which the transfer characteristics of Bragg gratings can be calculated. To find a solution, the following substitutions are made for the forward and backward propagating modes

$$\begin{aligned} R &= A_\upsilon e^{-(i/2)(\Delta\beta z - \phi(z))} \\ S &= B_\mu e^{(i/2)(\Delta\beta z - \phi(z))} \end{aligned} \tag{2.34}$$

Differentiating (2.34) and substituting into (2.29) and (2.33) results in the following couple mode equations

$$\frac{dR}{dz} + i\left[k_{dc} + \frac{1}{2}\left(\Delta\beta - \frac{d\phi(z)}{dz}\right)\right]R = -ik_{ac}^* S \tag{2.35}$$

$$\frac{dS}{dz} - i\left[k_{dc} + \frac{1}{2}\left(\Delta\beta - \frac{d\phi(z)}{dz}\right)\right]S = ik_{ac}R \tag{2.36}$$

The "dc" coupling constant, k_{dc}, influences propagation due to the change in the average refractive index of the mode. Any absorption, scatter loss, or gain can be incorporated in the magnitude and sign of the imaginary part of k_{dc}. The term $\Delta\beta/2$ in (2.35) and (2.36) is the detuning and indicates how rapidly the power is exchanged between the "radiated" (generated) field and the polarization ("bound") field. This weighting factor is proportional to the inverse of the distance that the field travels in the generated mode. At phase matching ($\Delta\beta = 0$), the field couples to the generated wave over an infinite distance. Finally, the rate of change of ϕ signifies a chirp in the period of the grating and has an effect similar to that of the detuning. Therefore, for uniform gratings, $d\phi/dz = 0$, and for unity visibility factor of the grating, $k_{ac} = k_{dc}/2$.

The coupled mode equations (2.35) and (2.36) can be solved by replacing the differential operator by λ and solving the characteristic equation by equating the characteristic determinant to zero. The resultant eigenvalue equation is in general a polynomial in the eigenvalues λ. Once the eigenvalues are found, the boundary values are applied for uniform gratings, assuming that the amplitude of the incident radiation from $-\infty$ at the input of the grating (of length L) at z=0 is R(0)=1, and that the field S(L)=0. The latter condition is satisfied by the fact that the reflected field at the output end of the grating cannot exist due to the absence of the perturbation beyond that region. These conditions result in the following analytical solution for the amplitude reflection coefficient

$$\rho = \frac{S(0)}{R(0)} = \frac{-k_{ac}\sinh(\alpha L)}{\delta\sinh(\alpha L) - i\alpha\cosh(\alpha L)} \tag{2.37}$$

where

$$\delta = k_{dc} + \frac{1}{2}\left(\Delta\beta - \frac{d\phi(z)}{dz}\right) \tag{2.38}$$

$$\alpha = \sqrt{|k_{ac}|^2 - \delta^2} \tag{2.39}$$

From equations (2.35) to (2.39), a few points deserve particular attention: for reflection gratings that have constant period Λ, the phase variation, $d\phi(z)/dz$, is zero; at precise phase matching $\Delta\beta$ is zero and the "ac" coupling constant, k_{ac}, is a real quantity; finally, the power reflection coefficient, $r = |\rho|^2$ is given by

$$r = |\rho|^2 = \frac{|k_{ac}|^2 \sinh^2(\alpha L)}{|k_{ac}|^2 \cosh^2(\alpha L) - \delta^2} \tag{2.40}$$

in which (2.39) has been used to simplify the result.

A number of interesting features of fiber Bragg gratings can be seen from these results. Quantities of interest include the bandwidth, $\Delta\lambda$, the reflectivity, the transmissivity, the variation in the phase, ϕ, and the grating dispersion, D, as a function of the wavelength.

Typical examples of the power reflectivity, r, for uniform gratings with three different values of $k_{ac}L$, 2 ($\Delta n=1\times10^{-4}$), 5 ($\Delta n=2.5\times10^{-4}$) and 8 ($\Delta n=3.95\times10^{-4}$), using (2.40), are shown in Figure 2.4. It can be seen that the central peak is bounded on either side by a number of sub peaks. This feature is characteristic of a uniform periodic grating of finite length, with a constant fringe visibility. The abrupt spatial start and end of the grating is responsible for the side band structure.

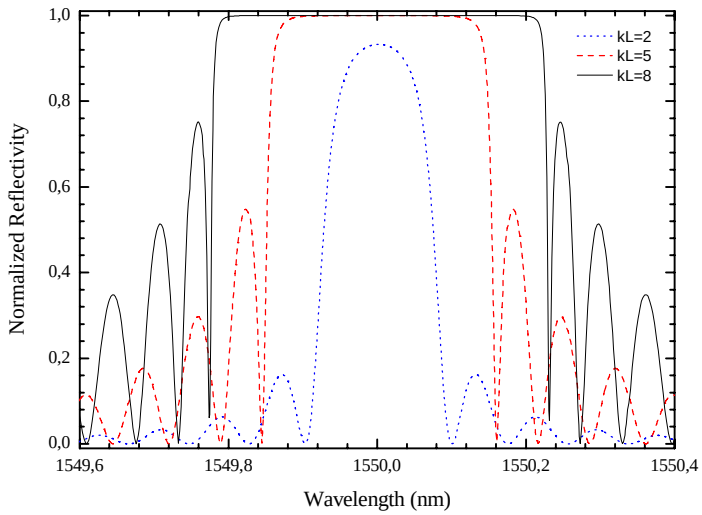

Figure 2.4 – Reflection spectra of three uniform gratings (L=10mm) versus wavelength for Bragg reflection for kL=2 (dot), kL=5 (dash) and kL=8 (solid).

For the uniform grating, $d\phi/dz=0$, the peak reflectivity occurs at a wavelength at which $\delta=0$ (and therefore, $\alpha=k_{ac}$), and equation (2.38) leads to

$$k_{dc} + \frac{\Delta\beta}{2} = 0 \tag{2.41}$$

At the phase matching wavelength, the reflectivity reduces to

$$r = \tanh^2\left(k_{ac}L\right) \tag{2.42}$$

For identical forward and counterpropagating modes, and using the orthogonality relationship [138] in (2.31) and (2.32) it comes that

$$\begin{aligned} k_{dc} &= \frac{2\pi\,\overline{\Delta n}\;\eta}{\lambda} \\ k_{ac} &= \frac{\nu}{2}k_{dc} = \frac{\pi\,\Delta n\,\eta}{\lambda} \end{aligned} \tag{2.43}$$

where the overlap integral, η, is ≈1 for identical modes and the substitution $\Delta n = \nu\overline{\Delta n}$ was used in the "ac" coupling constant equation. The overlap integral is a weighting factor, $0<\eta<1$, dependent on the mode and refractive index profiles and can be understood as the core power confinement factor for the mode of interest. For a uniformly written grating along the core, $\eta \approx 1\text{-}V^{-2}$, where $V = \left(2\pi a/\lambda\right)\sqrt{n_{co}^2 - n_{cl}^2}$ is the normalized frequency parameter, being a the core radius, n_{co} and n_{cl} the core and cladding refractive index, respectively.

Therefore, the peak of the Bragg reflection is at

$$\lambda_{\max} = \lambda_B\left(1 + \frac{\overline{\Delta n}\;\eta}{n}\right) \tag{2.44}$$

The Bragg wavelength, λ_B, is defined at the phase matching point $\Delta\beta=0$ for the general case of dissimilar modes,

$$\frac{2\pi}{\Lambda} = \frac{2\pi n_{eff,\upsilon}}{\lambda} + \frac{2\pi n_{eff,\mu}}{\lambda} \tag{2.45}$$

giving

$$\Lambda = \frac{\lambda}{n_{eff,\upsilon} + n_{eff,\mu}} \tag{2.46}$$

For identical forward and counter propagating modes or nearly identical mode indexes, (2.46) reduces to

$$\Lambda = \frac{\lambda}{2n_{eff}} \tag{2.47}$$

which is an equivalent result to the grating condition (2.6) predicted by considering the optical diffraction analysis presented in section 2.2. The reflection peak given by (2.44) is at a longer wavelength than the Bragg wavelength, since the average refractive mode index, $\overline{\Delta n}$, continuously increases with a positive refractive index modulation.

Figure 2.5 shows the grating reflectivity as a function of k_{ac} (and refractive index change) for five different grating lengths.

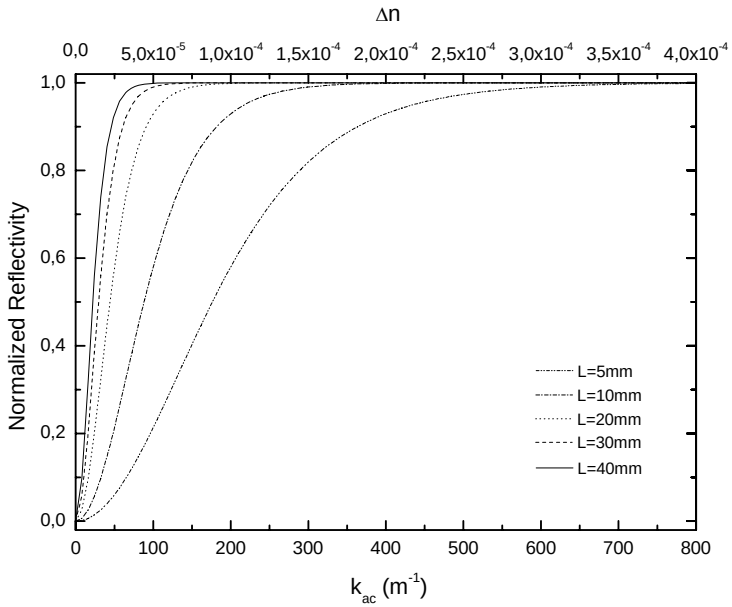

Figure 2.5 – Reflectivity versus k_{ac} and modulated index change, Δn, for grating lengths of 5, 10, 20, 30 and 40 mm (λ=1550nm and η=1).

From Figure 2.5 it can be seen that longer gratings reach high reflectivity levels even for low induced index changes, while shorter gratings need high induced index changes in order to achieve high reflectivities.

In terms of grating bandwidth, the most common deducible definition is the distance between the first minima on either side of the main reflection peak, which is given by [138]

$$2\Delta\lambda = \frac{\lambda^2}{\pi\ n_{eff} L}\sqrt{(k_{ac}L)^2 + \pi^2} \tag{2.48}$$

For weak gratings, $(k_{ac}L)^2 << \pi^2$, the bandwidth is an inverse function of the grating length:

$$2\Delta\lambda \approx \frac{\lambda^2}{n_{eff} L} \tag{2.49}$$

while for strong gratings, $(k_{ac}L)^2 >> \pi^2$, the bandwidth is independent of the length of the grating and is proportional to the "ac" coupling constant:

$$2\Delta\lambda \approx \frac{\lambda^2 k_{ac}}{\pi\ n_{eff}} \tag{2.50}$$

Figure 2.6 shows the bandwidth behaviour for the limits of (2.49) and (2.50), where in the case of weak gratings the dependence is only on the grating length, while for strong gratings, the bandwidth is independent of the grating length and depends strongly on the induced refractive index change.

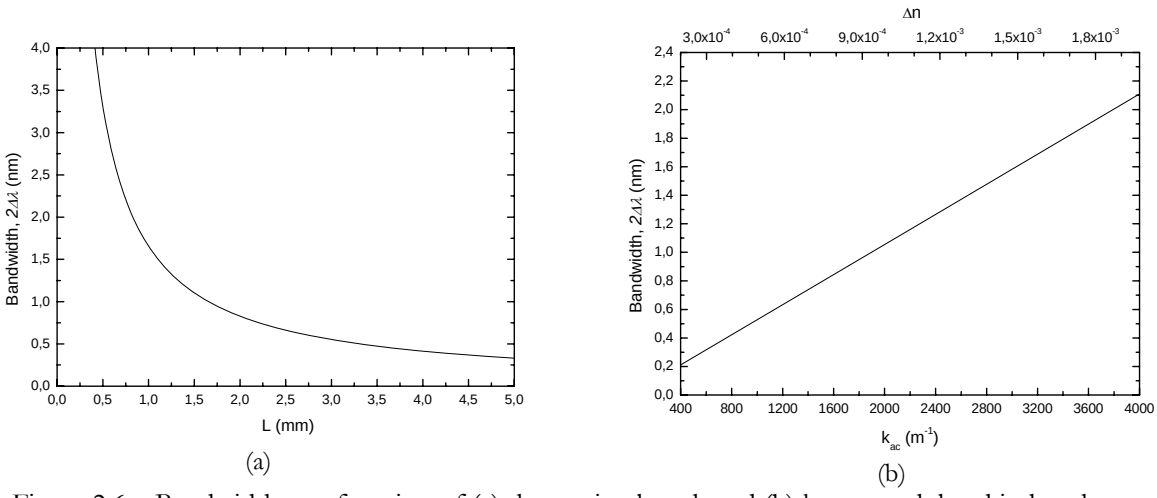

Figure 2.6 – Bandwidth as a function of (a) the grating length and (b) k_{ac} or modulated index change considering the limits for weak and strong gratings, respectively (λ=1550nm, n_{eff}=1.45 and η=1).

For strong gratings the light does not penetrate the fully into the grating, and thus the bandwidth is independent of length and directly proportional to the induced index change, so that increasing k_{ac} increases the bandwidth. In strong gratings, the bandwidth is similar whether measured at the band edges (at the first zeros) or as the full-width-half-maximum (FWHM), as it can be seen, for example, in Figure 2.4 for kL=8.

The temporal response of Bragg gratings is also an important property that should be considered in some applications, like dispersion compensation and pulse shaping. More and more the dispersive properties of fiber Bragg gratings are being considered, since fiber optic systems are no longer loss limited (thanks to optical amplifiers) but rather limited by dispersion. Dispersion compensation neglection can lead to inter-symbol interference and to a considerable hampering of system performance.

The group delay and dispersion of the reflected light through or from a Bragg grating can be determined from the phase of the amplitude reflection coefficient of (2.37). Thus, if $\phi \equiv \text{phase}(\rho)$, then at a local frequency w_0, ϕ can be expanded in a Taylor series about w_0. Since the first derivative $d\phi/dw$ is directly proportional to the frequency w, this quantity can be identified as a time delay. Therefore, the time delay (usually given in picoseconds), τ, for light reflected from a grating is

$$\tau = \frac{d\phi}{dw} = -\frac{\lambda^2}{2\pi c}\frac{d\phi}{d\lambda} \tag{2.51}$$

where c is the speed of light. Figure 2.7 shows the calculated delay for the three grating spectra profiles shown in Figure 2.4. From these two figures, it can be seen that for unchirped uniform Bragg gratings, the reflectivity and delay are symmetric about the wavelength λ_{max}.

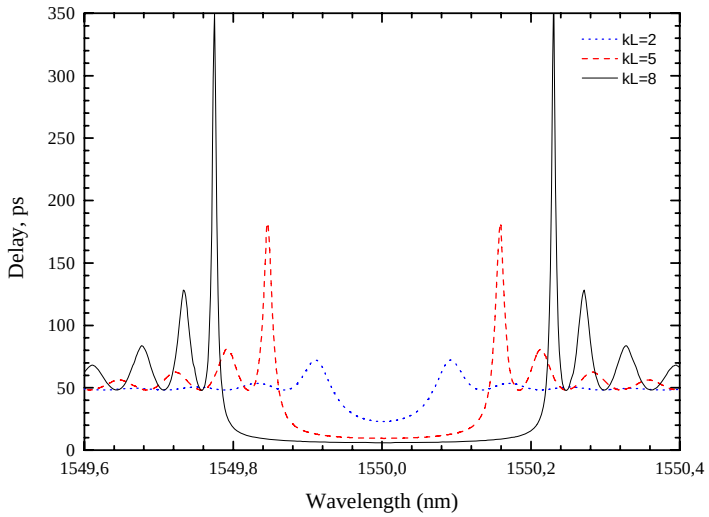

Figure 2.7 – Group delay of three uniform gratings (L=10mm) versus wavelength for kL=2 (dot), kL=5 (dash) and kL=8 (solid).

The dispersion, *D*, is the rate of change of delay with wavelength and so is given by (usually in ps/nm)

$$D = \frac{d\tau}{d\lambda} = -\frac{2\pi c}{\lambda^2}\frac{d^2\phi}{dw^2} \tag{2.52}$$

In uniform gratings, the dispersion is zero near λ_{max} and only becomes appreciable near the band edges and side lobes of the reflection spectrum, where it tends to vary rapidly with wavelength. For wavelengths outside the bandgap, the boundaries of the uniform grating act like abrupt interfaces, behaving like a Fabry-Perot cavity. The nulls in the reflection spectra are analogous to Fabry-Perot resonances. At these frequencies, light is trapped inside the cavity for many round trips, thus experiencing enhanced delay.

2.4 Transfer matrix method

A fiber Bragg grating of a constant refractive index modulation and period can have an analytical solution. However, for a more complex structure, with an arbitrary varying coupling constant, $k(z)$, and chirp, $\Lambda(z)$, no simple form exists because the variables cannot be separated since they collectively affect the transfer function. In this case, the structure (grating) may be considered to be a concatenation of several small sections, each of constant period and unique refractive index

modulation. Thus, the modeling of the transfer functions of Bragg gratings becomes a relatively simple problem, and the application of the transfer matrix method [148] provides an accurate and fast technique for analyzing more complex grating profiles. This method is capable of simulating both strong and weak gratings, with or without chirp and apodization. In the transfer matrix method, the coupled mode equations deduced in section 2.3 are used to calculate the output fields of a short uniform section, δl_1, of the grating, each possessing a unique and autonomous functional dependence on the spatial parameter z. For such a grating (representing a small section of the total grating), the analytical solution provides the amplitude reflectivity, transmission and phase. These parameters are then used as the input for the adjacent small section, δl_2 (not necessarily equal to δl_1). Figure 2.8 shows the input (R(-δl_1/2) and R(δl_1/2)) and output (S(-δl_1/2) and S(δl_1/2)) fields for each single grating section. A transfer matrix T represents the grating amplitude and phase response. The relation between the input and output fields is then given by

$$\begin{bmatrix} R(-\delta l_1/2) \\ S(-\delta l_1/2) \end{bmatrix} = [T] \begin{bmatrix} R(\delta l_1/2) \\ S(\delta l_1/2) \end{bmatrix} \tag{2.53}$$

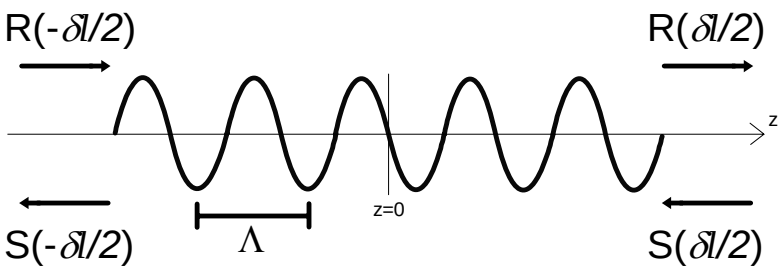

Figure 2.8 – Representation of the input and output fields in the refractive index modulation for a small section of the grating.

Considering a reflection grating (or Bragg grating), the input field amplitude R(-δl_1/2) is normalized to unity and the reflected field amplitude at the output of the grating S(δl_1/2) is zero, since there is no perturbation beyond the end of the grating. By applying these boundary conditions to (2.53) and writing the matrix elements results in

$$\begin{bmatrix} 1 \\ S(-\delta l_1/2) \end{bmatrix} = \begin{bmatrix} T_{11} & T_{12} \\ T_{21} & T_{22} \end{bmatrix} \begin{bmatrix} R(\delta l_1/2) \\ 0 \end{bmatrix} \tag{2.54}$$

From (2.54), the transmitted and reflected amplitudes are easily seen to be given by

$$R(\delta l_1/2) = \frac{1}{T_{11}}$$
$$S(-\delta l_1/2) = \frac{T_{21}}{T_{11}} \tag{2.55}$$

These new fields can now be transformed by another matrix, representing the next adjacent section, so that the entire grating with N sections is described by

$$\begin{bmatrix} R(-L/2) \\ S(-L/2) \end{bmatrix} = [T^N]\cdots[T^3]\,[T^2]\,[T^1]\begin{bmatrix} R(L/2) \\ S(L/2) \end{bmatrix} \tag{2.56}$$

where $L = \sum_{j=1}^{N} \delta l_j$. The multiplication of the individual matrices can be described by an overall 2×2 matrix as follows

$$[T_{Grating}] = \prod_{j=1}^{N} [T^j] \tag{2.57}$$

yielding,

$$\begin{bmatrix} R(-L/2) \\ S(-L/2) \end{bmatrix} = [T_{Grating}]\begin{bmatrix} R(L/2) \\ S(L/2) \end{bmatrix} \tag{2.58}$$

Following the results obtained in (2.55), the transmissivity, *t*, and the reflectivity, *r*, of the whole grating are given by

$$t = \frac{1}{T_{11}}$$
$$r = \frac{T_{21}}{T_{11}} \tag{2.59}$$

where the elements of the matrix are obtained from the solution of the coupled mode equations (2.35) and (2.36) for the *j*th section as follows

$$T_{11} = \cosh(\alpha\delta l_j) - \frac{i\delta \sinh(\alpha\delta l_j)}{\alpha} \tag{2.60}$$

$$T_{22} = \cosh(\alpha\delta l_j) + \frac{i\delta \sinh(\alpha\delta l_j)}{\alpha} \tag{2.61}$$

$$T_{12} = -\frac{ik_{ac} \sinh(\alpha\delta l_j)}{\alpha} \tag{2.62}$$

$$T_{21} = -\frac{ik_{ac} \sinh(\alpha\delta l_j)}{\alpha} \tag{2.63}$$

Particular interest exists in well controlled phase shifts incorporated at precise positions within a distributed grating structure. The phase jump introduces a bandgap within the reflection bandwidth, creating a narrow transmission band. A phase shift is obtained in the transfer matrix by multiplying the reflectivity of the *j*th section by matrix elements containing only phase terms. Therefore, the transfer matrix takes the form

$$\begin{bmatrix} R(-L/2) \\ S(-L/2) \end{bmatrix} = [T^N] \cdots [T^3] \, [T_{ps}] \, [T^1] \begin{bmatrix} R(L/2) \\ S(L/2) \end{bmatrix} \tag{2.64}$$

where T_{ps} is the new phase shift matrix for a Bragg grating, given by

$$T_{ps} = \begin{bmatrix} e^{-i\phi/2} & 0 \\ 0 & e^{i\phi/2} \end{bmatrix} \tag{2.65}$$

The phase factor, $\phi/2$, is any arbitrary phase and may result from a change in n_{eff}, or from a discontinuity within the grating.

Finally, it is important to mention that some conditions must be met in order to accurately simulate the grating response. First, the length of the sections must be larger than the period of the modulation: $\delta l_j \geq \Lambda_j \times K$, where K is a suitably large number. Second, each section j must have an integer number of grating periods in order to have a smooth transition between sections, since an

abrupt change in the grating modulation is equivalent to a phase shift. Third, any spatial variation in the refractive index modulation should be smooth, since sections of constant k_{ac} but different from adjacent ones certainly forms a superstructure.

2.5 Bragg gratings with special characteristics

Most of the designed gratings for practical applications are not uniform. The need for high performance and tailored spectral and dispersive characteristics of Bragg gratings imposes the fabrication of special structures. These structures can be achieved by varying numerous physical parameters like induced index change and/or periodicity along the grating, length, and fringe tilt. In this way, special gratings like apodized, chirped, phase shifted and sampled can be fabricated, instead of the standard uniform Bragg gratings. In this section, the fundamental properties such as the spectral and the temporal response of these special Bragg gratings are described. Indications about their fabrication methods and applications were already referenced in section 1.2. All the simulation results included in this section were performed using the transfer matrix method described in section 2.4.

2.5.1 Apodized Bragg gratings

In standard uniform Bragg gratings the refractive index change along the grating length is constant. Thus, they begin abruptly and end abruptly, presenting a sudden step change in the refractive index. The Fourier transform of this rectangular function is the well known *sinc* function, with its associated sidelobe structure presented in the reflection spectrum (see Figure 2.4). In a vast number of applications, like WDM, it is very important to minimize and, if possible, eliminate the reflectivity of these sidelobes. The Fourier transform of a gaussian function is also a gaussian, and so a grating with such refractive modulation amplitude profile would reduce substantially the sidelobe structure, and such grating is said to be apodized. However, a simple change of the refractive index modulation amplitude changes the local Bragg wavelength as well, forming a distributed Fabry-Perot interferometer, which causes sidelobes to appear in the low wavelength side of the reflection spectrum of the grating [129]. To avoid this effect, the average refractive index through the length of the grating should be kept unchanged, while varying the refractive index modulation amplitude. Apodization is thus a valuable tool to smooth out the reflection spectrum of a Bragg grating, but

that has also impact in the dispersion characteristics of the grating, reducing the ripple usually present in the group delay.

The effect of the apodization in the models of the Bragg grating can be represented by using a z-dependent function, $f(z)$, in the refractive index, along the grating length, L. The variation refractive index, from (2.1), can now be rewritten for an apodized Bragg grating as

$$\delta n_{eff}(z) = \overline{\Delta n} + \Delta n \; f(z) \cos\left[\frac{2\pi}{\Lambda} z\right] \tag{2.66}$$

Generally, the modulation function (also called apodization function), $f(z)$, is a given bell-like functional shape (for the uniform Bragg grating, it is clear that $f(z)=1$), that can be, for example, *Gaussian*, *raised cosine*, *Hamming*, *Blackman* or *sinc*. Other examples of modulation functions are the *tanh*, *Cauchy* and *Kaiser*, but will not be explored here.

The *Gaussian* profile, one of the most popular, is given by [129]

$$f(z) = \exp\left[-4\ln(2) \times \left(\frac{z - \frac{L}{2}}{FWHM}\right)^2\right], \qquad 0 \le z \le L \tag{2.67}$$

where FWHM is the full-width-at-half-maximum of the grating profile, and typically chosen as FWHM~$L/3$.

Another common profile is the *raised-cosine* shape [129]

$$f(z) = \frac{1}{2}\left\{1 + \cos\left[\frac{\pi\left(z - \frac{L}{2}\right)}{FWHM}\right]\right\}, \qquad 0 \le z \le L \tag{2.68}$$

where in this case, normally, FWHM=L.

The *Hamming* and *Blackman* profiles are members of the *cosine* windows, and can be described as [147]

$$f(z) = \sum_{l=1}^{K} a_l \cos\left[\frac{2\pi\ l\left(z - \frac{L}{2}\right)}{L}\right], \qquad 0 \le z \le L \tag{2.69}$$

The Hamming shape requires a_0=0.42 and a_1=0.50, whereas the Blackman window requires an additional coefficient a_2=0.08. Optimization of these coefficients leads to the minimization of the maximum sidelobe levels.

Another option is the *sinc* profile, which can be expressed as [142]

$$f(z) = \frac{\sin\left[\frac{2\pi}{L}\left(z - \frac{L}{2}\right)\right]}{\frac{2\pi}{L}\left(z - \frac{L}{2}\right)}, \qquad 0 \le z \le L \tag{2.70}$$

The various envelopes of the index modulation profiles expressed from (2.67) to (2.70) are plotted in Figure 2.9 for visualization and comparison. The functions are truncated at the values described, but investigation can be carried in order to optimize these values for specific application purposes.

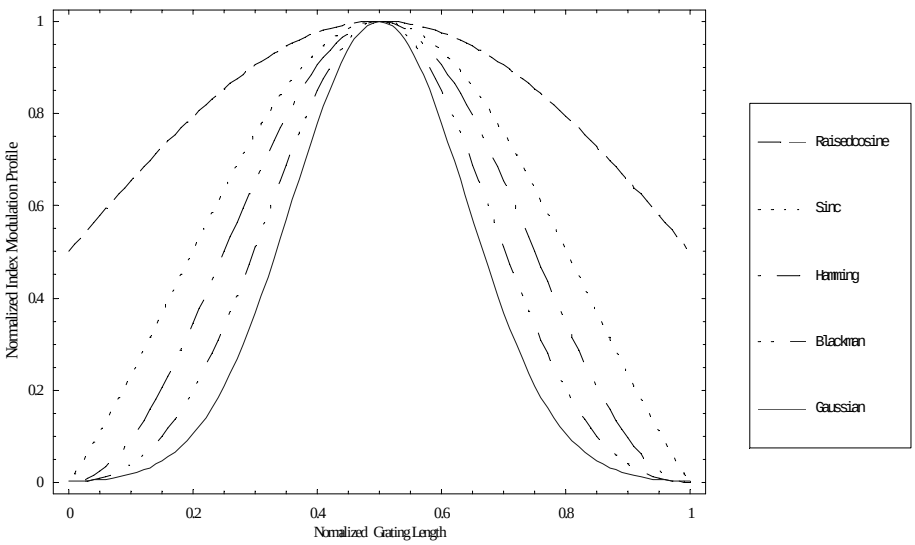

Figure 2.9 – Different apodization profiles described in equations (2.67) to (2.70).

By keeping the average refractive index constant, a symmetrical spectrum is obtained, avoiding in this way the already mentioned effect of sidelobes appearing in the low wavelength side of the reflection spectrum of the grating [129]. Figure 2.10 shows the variation of the induced index change

along the grating for the various types of the apodization envelopes presented in Figure 2.9 (with constant average refractive index).

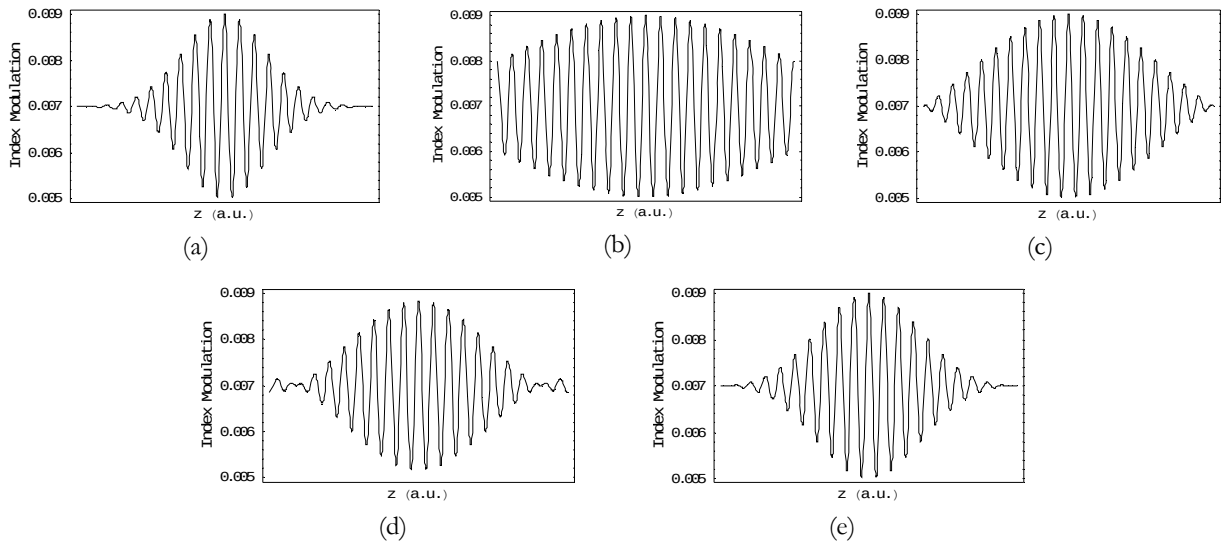

Figure 2.10 – Variation of the refractive index change along the grating for a (a) Gaussian, (b) raisedcosine, (c) sinc, (d) Hamming and (e) Blackman profile, with constant-dc index change.

The reflection spectrum of three apodization functions is shown in Figure 2.11.

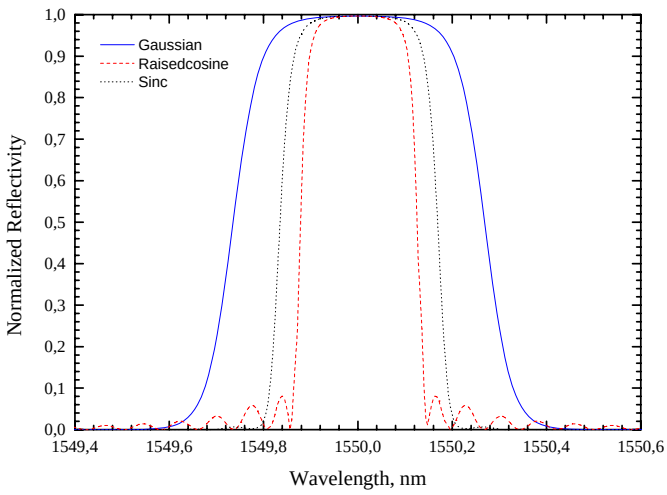

Figure 2.11 – Reflectivity spectrum of three apodized Bragg gratings with Gaussian, raisedcosine and sinc apodization profiles.

All gratings shown in Figure 2.11 have the same reflectivity (99.7 %, corresponding to 25 dB isolation in transmission) and the same length (10 mm) and the spatial profiles used are described in (2.67), (2.68) and (2.70) for the *Gaussian*, *raisedcosine* and *sinc* functions, respectively. For a better comparison of the side lobe suppression on each, Figure 2.12 shows a close-up view of the filter

edges on a logarithmic scale, including also the profile of a uniform Bragg grating with the same reflectivity and length.

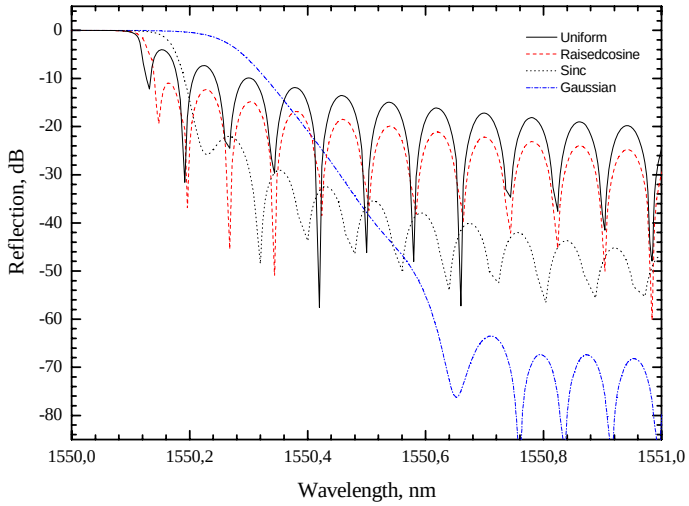

Figure 2.12 – Close-up view of the edges of the three apodized gratings shown in Figure 2.11 compared with a uniform Bragg grating.

Clearly, the *Gaussian* apodization function is the one that allows higher side lobes suppression, when compared to the *raisedcosine* and *sinc* profiles. The side lobe structure still very evident in the *raisedcosine* spectrum results from the fact that the ends of the grating does not experience a smooth transition in terms of refractive index change, but instead a small step inherent to the *raisedcosine* function (Figure 2.10-b).

2.5.2 Chirped Bragg gratings

Gratings that present a nonuniform period along their length are known as chirped. The period may vary symmetrically, either increasing or decreasing around a pitch in the middle of a grating, may vary linearly with length of the grating (linear chirp), or may be quadratic. Another alternative is the variation of the average effective refractive index along the length of the grating, which can be achieved by changing the amplitude of the refractive index modulation profile, or by tapering the fiber in the region of the grating length.

Figure 2.13 shows the schematic of a chirped Bragg grating structure and its basic properties.

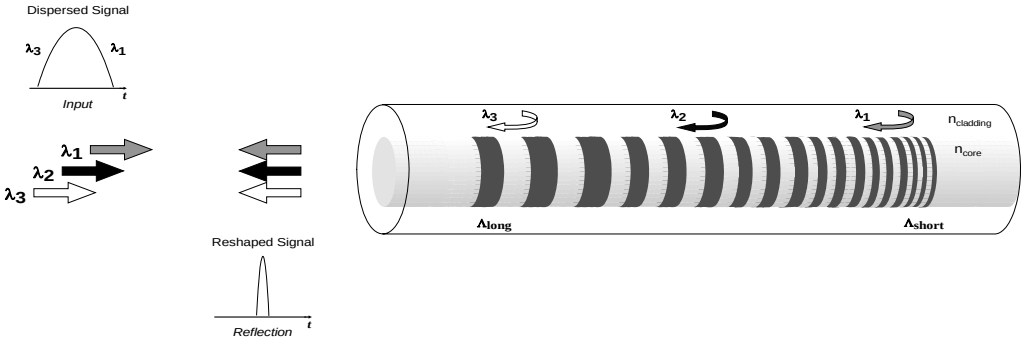

Figure 2.13 – Illustration and principle of operation of a chirped fiber Bragg grating structure.

The variation refractive index, from (2.1), can now be rewritten for a chirped Bragg grating as

$$\delta n_{eff}(z) = \overline{\Delta n}(z)\left\{1 + \nu \cos\left[\frac{2\pi z}{\Lambda + C_\Lambda z}\right]\right\} \tag{2.71}$$

where C_Λ is the chirp coefficient (typically between 0.05 and 40 nm/mm) and the z dependence in the refractive index change considers also the possibility of chirping by average refractive index variation. Figure 2.14 shows the refractive index variation for this type of gratings, (a) considering only a refractive index variation ($C_\Lambda = 0$) or (b) only a direct period variation ($\overline{\Delta n}$=const.) by means of changing the chirp coefficient.

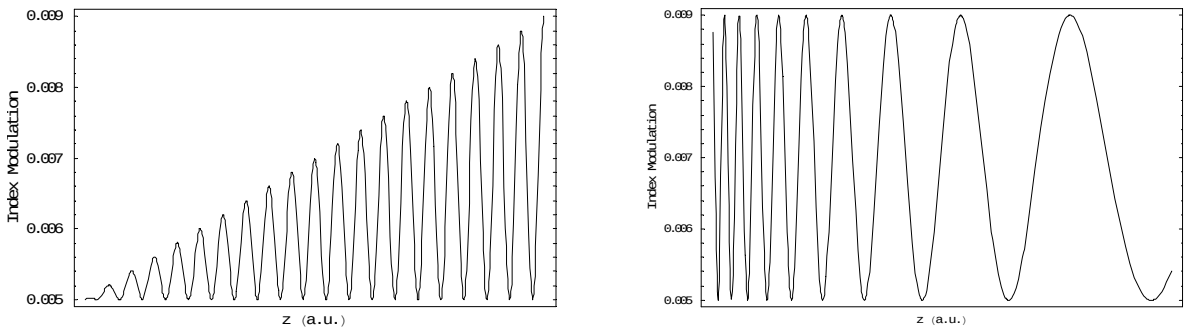

(a) (b)

Figure 2.14 –Non-uniform variation (a) of the refractive index modulation and (b) of the grating period along the grating length.

The chirp period, $\Delta\Lambda_{chirp}$, may be related to the bandwidth of the chirped grating, $\Delta\lambda_{chirp}$, by

$$\Delta\lambda_{chirp} = 2n_{eff}\left(\Lambda_{long} - \Lambda_{short}\right) = 2n_{eff}\Delta\Lambda_{chirp} \tag{2.72}$$

Light entering into a positively chirped grating (increasing period from input end) suffers a delay, τ, since reflection is a function of wavelength, given by

$$\tau(\lambda) \approx \frac{(\lambda_0 - \lambda)}{\Delta\lambda_{chirp}} \frac{2L}{v_g}, \qquad 2n_{eff}\Lambda_{short} < \lambda < 2n_{eff}\Lambda_{long} \tag{2.73}$$

where λ_0 is the Bragg wavelength at the center of the chirped bandwidth of the grating, L is the grating length and v_g is the average group velocity of light in the fiber. Therefore, chirped gratings disperse light by introducing a maximum delay of $2L/v_g$ between the shortest and longest reflected wavelengths. This dispersion is of extreme importance, since it can be used to compensate for the chromatic dispersion induced broadening in optical fiber transmission systems. As the grating period varies along the length, different wavelengths are delayed by different intervals when they travel along the fiber, introducing differential group delay among the various wavelengths. The net effect is a compression (or broadening) of the input pulse thus compensating for the chromatic dispersion along the fiber link. For reflective-type gratings, the compressed and compensated reflected wavelengths all return to the entrance of the grating at the same time (see Figure 2.13), where, for example, using an optical circulator one can collect the dispersion-compensated signal.

The reflection spectrum of chirped Bragg gratings, as well as its important delay behavior as a function of wavelength, is shown in Figure 2.15.

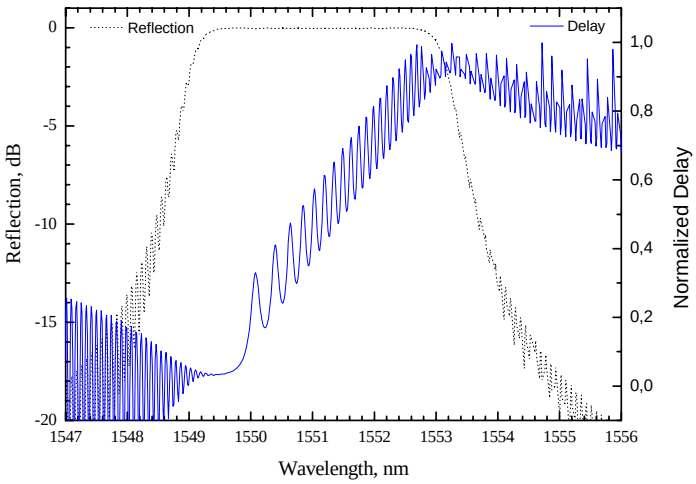

Figure 2.15 – Reflectivity and delay spectrum of chirped Bragg gratings.

The strong ripple observed in the delay of Figure 2.15 is due to the way how the simulation program was made, and so this may be improved.

2.5.3 Phase shifted Bragg gratings

As the name indicates, a phase shifted grating consists on a grating with an introduced phase jump in the refractive index modulation. This phase shift originates two Bragg gratings out of phase that act like a resonant cavity. The resonant frequencies correspond to very narrow transmission filters on the rejection band of the Bragg grating. The respective resonant wavelength is defined by the amplitude and position of the phase step. The distributed feedback (DFB) fiber grating is probably the simplest band-pass filter. A simple illustration of this type of grating is shown in Figure 2.16.

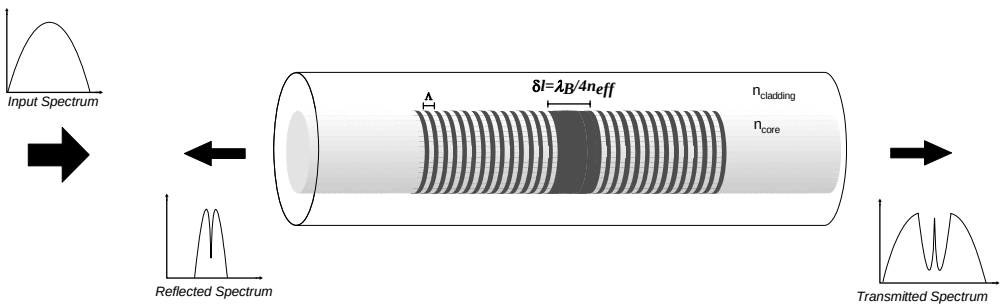

Figure 2.16 – Illustration of a π-shifted fiber Bragg grating structure.

For the particular case of Figure 2.16, the amplitude of the band gap, δl, between the two Bragg gratings is set to $\lambda_B/4n_{eff}$, and a transmission peak appears in the center of the band stop. The pass band peak has a very narrow Lorentzian line shape and is extremely useful for filtering. This narrow pass band peak can be tuned by adjusting δl. For a better understanding, one can describe this behavior by considering this type of gratings as equivalent to an interferometer. Thus, it can be considered as multiple or two beam interference, like for example the Fabry-Perot interferometer, where each Bragg grating acts like a mirror and δl is the distance between them. The relations between the path difference, created by δl, and the corresponding change in the phase, ϕ, of an incident wave are well known and result in [141]

$$\delta l = \frac{\lambda_B}{4\pi\, n_{eff}}\phi \tag{2.74}$$

for normal incidence, which is the case. Equation (2.74) explains why for a desired phase shift of π, δl should be equal to $\lambda_B/4n_{eff}$, as already mentioned above. Other phase shifts, like $\pi/2$ and $3\pi/2$ are also easily achieved by a proper adjustment of δl, respecting (2.74).

Simulated phase shift gratings are shown in Figure 2.17. The phase shift is introduced exactly in the middle of the grating for all cases, but the amplitude of the phase shift is different for each situation ($\pi/2$, π and $3\pi/2$).

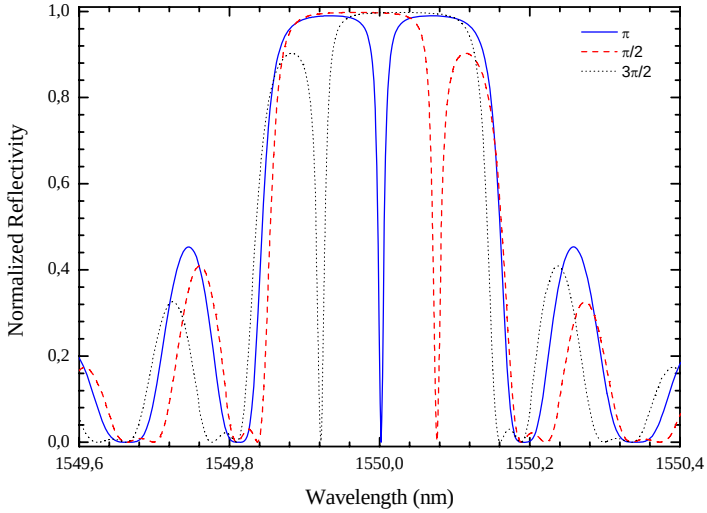

Figure 2.17 – Simulated spectra of phase-shifted fiber Bragg grating structures for three different phase steps applied in the center of the grating.

As it can be seen from the reflection spectra of Figure 2.17, by changing the amplitude of the phase shift, one can tune the resonant wavelength, and in this way select the desired position of the narrow transmission band inside the grating reflection spectrum. Some more complex configurations can be achieved by introducing various phase steps along the grating length. For example, Figure 2.18 shows three different arrangements. In the first (a), two π-phase shifts are introduced at L/4 and 3L/4. In the second (b), two π-phase shifts are introduced at L/3 and 2L/3. And in the third (c), three π-phase shifts are introduced at L/4, L/2 and 3L/4.

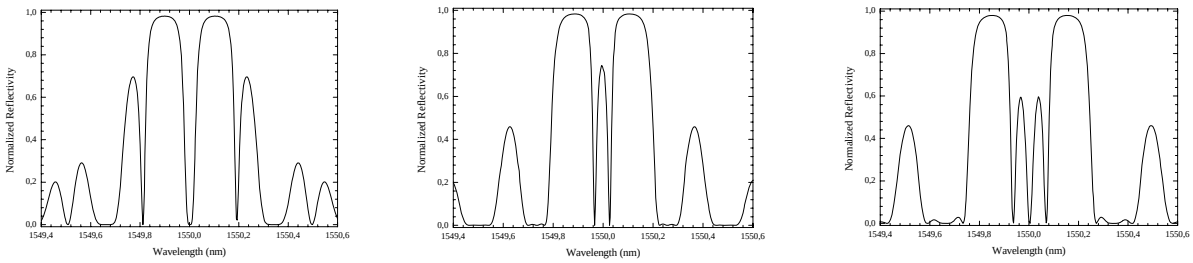

(a) (b) (c)

Figure 2.18 – Illustration of three different phase stepped gratings along the grating length with (a) two π-phase shifts introduced at L/4 and 3L/4; (b) two π-phase shifts introduced at L/3 and 2L/3; and (c) three π-phase shifts introduced at L/4, L/2 and 3L/4.

2.5.4 Sampled Bragg gratings

Sampled Bragg gratings are generated by a periodic modulation of the refractive index amplitude and/or phase in the waveguide. The resultant reflection spectrum and channel separation is a function of the shape and period of this modulation. The sampled grating is a conventional grating at the appropriate wavelength multiplied by a sampling function. Therefore, the spatial frequency content of these superstructures can be approximated by a comb of delta functions centered at the Bragg frequency. Most of the sampled Bragg gratings are amplitude modulated, using simple binary sampling functions, like simply modulating the intensity of the UV beam while scanning it along a fiber and phase mask assembly. Sampled Bragg gratings realized by phase modulation are also possible, enabling dense channel spacing without increasing the spacing of the Bragg grating.

The definition of the refractive index variation from (2.1), can now be rewritten for a sampled Bragg grating as

$$\delta n_{eff}(z) = \overline{\Delta n} + \Delta n \; S(z) \cos\left[\frac{2\pi}{\Lambda} z\right] \tag{2.75}$$

where *S(z)* is the sampling function with period *M*. This superstructure in then originated by a periodic modulation of the effective refractive index amplitude caused by multiplication of two signals with different frequencies (a rapidly varying component of period Λ, and a slowly varying envelope of period *M*). The resultant reflection spectra is a set of reflection peaks separated by a quantity given by [55]

$$\Delta\lambda = \frac{\lambda_B^2}{2 n_{eff} M} \tag{2.76}$$

Figure 2.19 shows this type of Bragg grating superstructures and its frequency response.

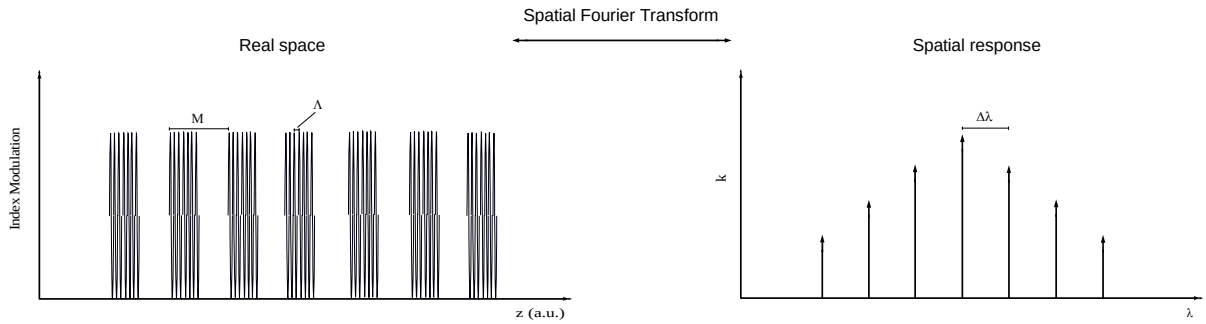

Figure 2.19 – Sampled Bragg grating superstructure and associated spatial frequencies.

As already mentioned, the spatial frequency content can be approximated by a comb of delta functions centred at the Bragg frequency. Every Fourier component contributes to a reflectivity peak of the reflection spectrum of the superstructure.

From (2.76) is clear that the peak separation, $\Delta\lambda$, can be easily increased (or decreased) by simply reducing (or rising) the sampling period, M. For example, to halve the channel spacing to $\Delta\lambda/2$, the sampling period has to be doubled to $2M$. Thus, the total sampled Bragg grating length needs to be doubled to keep the total sampled grating bandwidth. This kind of amplitude modulation leaves sections unused between each Bragg grating making it inefficient for writing sampled gratings. An alternative is the use of phase modulation, which can realise dense channel spacing without increasing the total grating length [59]. For example, the phase shift 0, π, 2π, 3π, … or 0, π, 0, π … between each Bragg grating enables the channel density to be doubled without changing the sampling period. In the same way, sampled gratings with triple channel density can be obtained by giving phase shifts of 0, $2\pi/3$, $4\pi/3$, 0, $2\pi/3$, …. To reduce the channel spacing to 1/m while keeping the sampling period, the phase shifts, ϕ_j, between the jth and (j+1)th Bragg grating are

$$\phi_j = \frac{2\pi}{m}(j-1), \qquad 0 \le j \le N \tag{2.77}$$

where N is the total number of Bragg gratings. Thus, channel spacing can be densified to $\Delta\lambda$/m while keeping the total sampled grating length unchanged. In this way, sampled gratings can realise dense channel spacing in a short length and can use the phase mask length and the waveguide efficiently.

2.6 Photosensitivity

Most applications require Bragg gratings with high reflectivity, and therefore the waveguide photosensitivity is an important factor in the development of specific gratings. Photosensitivity is the term describing refractive index changes of a waveguide when exposed to ultraviolet light. Initially, photosensitivity was considered to be a phenomenon associated only with germanium doped waveguides, becoming clear later on that this thought was not true since it has been observed in a wide variety of different waveguides, particularly in optical fibers, with no germanium content. Nevertheless, the presence of germanium in the fiber core remains as the most important material in which higher refractive index changes are achievable.

Several factors influence the magnitude of the refractive index change (Δn) such as the writing conditions (wavelength, intensity and total dose of irradiating light - fluence), the composition of the glassy material forming the core and any pre-processing routines before exposure (the most common photosensitivity enhancement is through molecular hydrogen loading by in-diffusion). The dependencies on fluence and hydrogen loading are the best studied, because of their commercial importance. The index change is not a simple, linear function of fluence, but rather a complicated curve, which does not allow a straightforward definition of the UV-sensitivity. Concerning treatment of the samples with hydrogen or deuterium there is consensus that it increases the UV-sensitivity. Another important aspect of UV-induced processes in glass is its stability over time, or the decay of the refractive index changes. As commercial products based on UV-writing find increasing applications, accelerated ageing tests have been performed to determine their stability. Most of the results are analyzed using a model that assumes the index changes are due to a very broad spectrum of defects with activation energies ranging from 0.5eV to 3.5eV [149, 150].

Although CW lasers, like the frequency doubled Argon laser at 244 nm, are used to photo-induce refractive index changes, the most common sources are the pulsed KrF and ArF excimer lasers (operating at 248 and 193 nm, respectively). Typically, the photosensitive waveguide is exposed to laser radiation for a few minutes at intensities ranging from 100 to 1000 mJ/cm^2. Under these conditions, values of Δn between 10^{-5} and 10^{-3} can be achieved in germanium doped monomode fiber. Techniques to enhance the refractive index change are well known, such as hydrogen loading or flame brushing, allowing a Δn as high as 10^{-2}.

Although photosensitivity is a well known and explored phenomena, its physical mechanisms are not completely understood, but are associated with defects in glassy materials [151-153]. This misunderstanding arises from the great complexity of glass material and is due to several aspects: its amorphous structure, the complications related to doping of the pure silica material, and the great experimental difficulties associated with precise spectroscopic investigations in the deep-UV part of the spectrum where the most important changes take place. Even though many researchers tend to agree that a large part of the UV-induced refractive index changes must be linked to some kind of compaction of the glass, there is still a lot of controversy on the details. For instance there is absolutely no consensus on how large a fraction of the refractive index change can be related to absorption changes and how much is simply compaction.

Among the well known defects formed in the germanium doped silica core are the paramagnetic Ge (*m*) defects, where *m* refers to the number of next-nearest-neighbor Ge/Si atoms surrounding a germanium ion with an associated unsatisfied single electron [154]. The Ge (1) and Ge (2) have been identified as trapped-electron centers [155], while the Ge (0) and Ge (3) centers, known as GeE', common in oxygen deficient germania, represent a hole trapped next to a germanium at an oxygen vacancy [156]. It has been shown to be independent of the number of next-neighbor Ge sites. Here an oxygen atom is missing from the tetrahedron, while the germania atom has an extra electron as an hanging bond. The extra electron distorts the molecule of germania as shown in Figure 2.20.

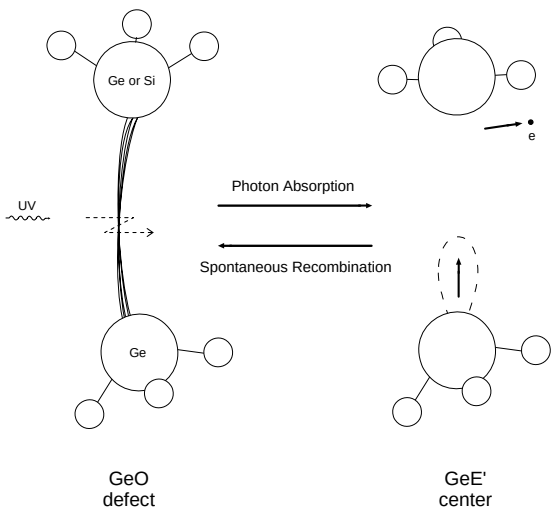

Figure 2.20 – Photoionization process of the GeO center, resulting in the release of an electron to the conduction band and in the formation of a GeE' center.

The GeO defect, shown in Figure 2.20, has a germanium atom coordinated with another Ge or Si atom. This bond has the characteristic 240 nm absorption peak that is observed in many

germanium-doped photosensitive optical fibers [5]. Under UV exposure, the bond breaks, creating a GeE' center. The electron from the GeE' center is liberated and it is free to move within the glass matrix via hopping or tunneling, or by two-photon excitation into the conduction band [157]. This electron can be re-trapped at the original site or at some other defect site. The removal of this electron causes a reconfiguration of the shape of the molecule, also changing the density of the material, as well as the absorption.

Photosensitivity enhancement is often needed since, besides allowing higher refractive index changes, it also accelerates the writing process. A method for photosensitizing silica optical fibers is based on the observation that increasing the 240 nm absorption enhances the effect [158]. Several mechanisms of photosensitivity enhancement have already been demonstrated, but the most used are the core doping and/or co-doping and the hydrogen loading [159].

Silica optical fibers with cores doped with germania (Ge), phosphorous (P), or alumina (Al) all exhibit increased photosensitivity when fabricated in a reduced atmosphere of hot hydrogen [160-162]. The disadvantage of this type of treatment is the increase in the absorption due to the presence of OH^- ions and also an increase in the refractive index of the core. An alternative is the co-doping with boron (B), which showed to be highly efficient in increasing photosensitivity [158, 163]. Another advantage of the presence of boron is the large reduction in the background refractive index, allowing more germania to be added in the core for a given core-cladding index difference. Although boron co-doped fiber gratings decay with temperature more rapidly than the ones made of pure germania doped fibers, there are ways to enhance their stability. Also, the presence of boron increases the absorption loss in the 1500 nm window by ~0.1 dB/m. An option to overcome this problems is to use tin (Sn) co-doping with germania [162]. This combination is more difficult to fabricate, but it does not present additional absorption in the 1500 nm window. It has a similar photosensitivity as the boron-germanium configuration and exhibits better temperature stability.

Hydrogen loading is a simple and very efficient technique to achieve high photosensitive responses in germanosilicate optical fibers [164, 165]. It is carried out by molecular diffusion of hydrogen in fibers, and can be achieved by two different ways: exposing the fiber to hydrogen at high temperature (600-700 ºC) and atmospheric pressure [166, 167]; or loading at room temperature but high pressure (20-700 atm) [165]. Nearly every germanium ion is a potential candidate for conversion from the Ge-O to the Ge-H state [168], causing index changes as large as 0.01. Once hydrogenated at room temperature, the fibers need to be stored at low temperatures to maintain their photosensitivity, since hydrogen diffuses out just as it can be introduced.

Finally it is worth to mention an interesting review paper by Douay *et al.* [169] and references therein, where the aspects and parameters described above are joined and very well presented, giving the reader a good perspective of the results that can be obtained when using some specific type of UV source, combined with co-doped waveguides and photosensitization treatments.

2.7 Conclusion

In this chapter, theory of Bragg gratings was introduced by means of the coupled mode theory analysis. The application of this analysis in the transfer matrix method allowed the simulation of different types of Bragg gratings. By defining its spatial profile, apodized (using and comparing specific apodization functions), chirped and phase-shifted Bragg gratings were modelled by implementing this method in Matlab®. The description of these complex structures, including also sampled Bragg gratings, provides a very useful understanding of its fundamental properties. Photosensitivity mechanisms, describing how waveguide refractive index changes when exposed to ultraviolet light, and photosensitivity enhancement techniques, like the doping and hydrogen loading, also deserved attention in this chapter, since they can largely affect the gratings desired performance.

3 Bragg gratings fabrication methods

3.1 Introduction

Advanced fabrication methods are essential for obtaining high quality and low cost Bragg gratings for telecom and sensing applications. An ideal Bragg grating technique should present some important features. First of all, it must allow the writing of gratings with good physical and optical qualities. The mechanical strength of a grating should not be degraded significantly after fabrication when compared with the strength of a good quality fiber. Also, a narrow and well defined spectral linewidth and a low excess loss are normally required to achieve high resolution measurements. Secondly, a fabrication technique should allow good repeatability, mainly of the central wavelength and the reflectivity in order to make Bragg gratings standard devices under the condition of mass production and interchangeable without calibration. Thirdly, it should be flexible, since reflectivities and central wavelengths of the produced gratings should be easily selectable. Finally, and in a commercial point of view, it should provide an economical mass production capability, since low cost Bragg gratings would be available if they could be mass produced at high speed.

The Bragg grating fabrication techniques most used broadly fall into two categories: the holographic and the phase mask approaches. In this chapter, these two techniques will be presented and described very briefly. In the first technique, a single UV input beam is divided into two, interfering then at the fiber plane. The second depends on an exposure of the fiber through an optical diffractive element. While some basic aspects regarding these methods have already been described in section 1.2, this section is focused on the different schemes proposed for grating inscription using the different techniques. Details on each writing method can be easily found in [137, 138]. The phase mask dithering/moving technique, which is used in this work, will be presented in detail in section 3.2, including the experimental setup description, the software developed for its control and the basic calibration procedures.

3.1.1 Holographic method

The first practical fabrication method reported [4] uses a holographic interferometer to produce an interference pattern within the fiber core, normal to the fiber axis as shown in Figure 3.1.

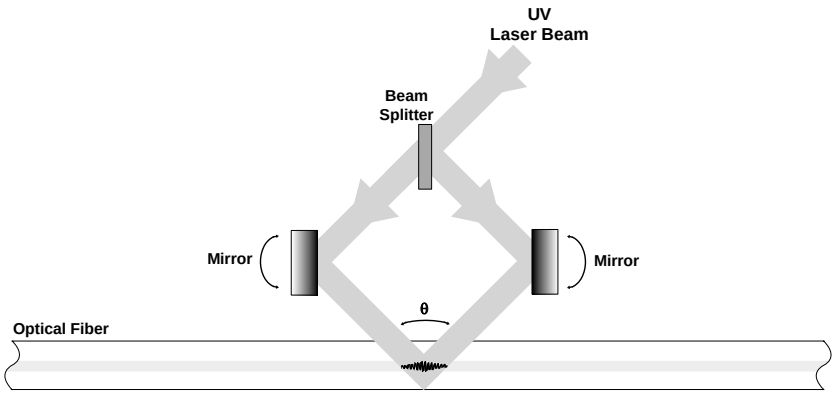

Figure 3.1 – UV interferometer for writing Bragg gratings.

As it can be seen, the UV beam is divided in two at a beam splitter and then brought together at a mutual angle of θ, by reflections from two UV mirrors. The fiber is then held at the intersection of the beams. This method allows the Bragg wavelength tunability, being the central wavelength, λ_B, given by

$$\lambda_B = \frac{n_{eff}\,\lambda_{UV}}{\sin\left(\frac{\theta}{2}\right)} \tag{3.1}$$

where n_{eff} is the effective mode index in the fiber, λ_{UV} is the wavelength of the writing radiation, and θ is the mutual angle of the UV beams. According to equation (3.1), tuning of the Bragg wavelength can be practically achieved by changing the angle between beams (by rotation of the mirrors). In this arrangement, three main parameters need to be controlled: the quality and stability of the beams; the accurate and precise adjustment of the incidence angle; and the mechanical stability of the complete writing system. Since the beam splitter spatially inverts the beam, if the spatial coherence of the source is poor, the quality of the interference fringe pattern can be seriously diminished. So, the spatial coherence requirements can be relaxed simply by controlling the total number of reflections in both arms of the interferometer in order to guarantee that both beams interfere with the symmetrical image. This allows the use of UV sources with low spatial coherence, as for example excimer lasers. The temporal coherence of the light has to be at least equal to the length of the grating in order to ensure that the interference pattern has good contrast ratio. Other variations of the scheme of Figure 3.1 make use of a simpler component, the transmission phase grating (a phase mask), in place of the 50 % beam splitter, like the standard based Talbot arrangement [16].

3.1.2 Phase mask method

The phase mask method has been reported as an improved technique for the fabrication of Bragg gratings [6, 19], allowing easier alignment and inscription. The UV light beam is spatially phase modulated and diffracted by the phase mask, as shown in Figure 3.2. The produced interference pattern is then used to photoimprint a refractive index modulation in the photosensitive fiber placed in proximity and parallel behind the phase mask.

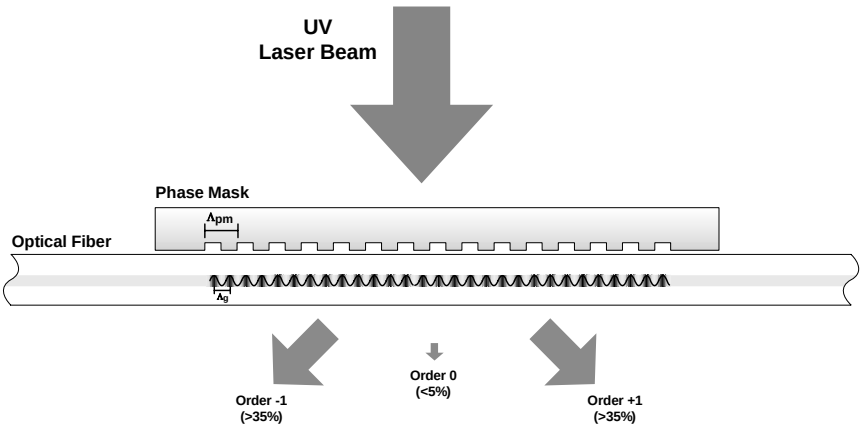

Figure 3.2 – Schematic diagram of the phase mask method.

As it can be seen from Figure 3.2, the phase mask is basically a grating etched in a high quality silica plate with well controlled space ratio and depth of the etched grooves. The principle of operation is based on the diffraction of an incident UV beam into several orders, m=0, ±1, ±2…. The incident and diffracted orders satisfy the general diffraction equation, with the period of the phase mask, Λ_{pm}, being given by

$$\Lambda_{pm} = \frac{m\lambda_{UV}}{\sin\left(\frac{\theta_m}{2}\right) - \sin(\theta_i)} \tag{3.2}$$

where λ_{UV} is the wavelength of the writing radiation, $\theta_m/2$ is the angle of the diffracted order, and θ_i is the angle of the incident UV beam. For normal incidence (θ_i = 0), as represented in Figure 3.2, the diffracted radiation is split into m=0 and ±1 orders. By a proper adjustment of the grooves depth, the zero diffraction order can be suppressed to values below 5 %, while each of the main diffracted beam orders (+1 and -1) contain more than 35 % of the incident radiation. Each phase mask has a zero order minimized for a single incident wavelength and so should be used with care at other

wavelengths since this factor can influence the grating pattern. The interference pattern of the two beams of orders ±1 brought together has a period Λ_g given by

$$\Lambda_g = \frac{\lambda_{UV}}{2\sin\left(\frac{\theta_m}{2}\right)} = \frac{\lambda_{UV}}{2\frac{\lambda_{UV}}{\Lambda_{pm}}} = \frac{\Lambda_{pm}}{2} \tag{3.3}$$

which is exactly half the value of the phase mask period and is independent of the UV wavelength. The Bragg wavelength, λ_B, required for the grating in the waveguide is determined by the period of the grating etched in the mask, Λ_{pm}. Thus, relating equations (3.3) and (2.6) or (2.47) becomes

$$\lambda_B = n_{eff}\Lambda_{pm} \tag{3.4}$$

The apparatus that implements the phase mask method is very compact and in general less sensitive to vibrations. But one of the most important advantages is the small coherence needed in the UV illuminating source to create the desired interference pattern. Associated with the fact that the Bragg wavelength is determined by the pitch of the phase mask and is independent of the wavelength of the UV source, this makes this technique much more attractive than the one described in 3.1.1. It also offers a high probability of mass production with good repeatability at low cost. However, for each Bragg wavelength a different phase mask is required. In order to remove this disadvantage, several approaches and modified schemes based in this technique have been presented. The easiest approach is to apply some mechanical tension to the optical fiber which allows to shift down the Bragg wavelength to a maximum of ~3 nm [170]. Another approach is the placement of a reducing lens before the phase mask, allowing the tuning of the Bragg wavelength of ~2 nm [171]. Other modifications have been proposed, like for example the already mentioned based Talbot arrangements, where the phase mask is used as a beam splitter (see Figure 3.3) [16]. In this case, one or two of the mirrors are rotatable and/or displaceable, building a small size interferometer integrating the flexibility of the mirror interferometer and the compactness of the phase mask scheme.

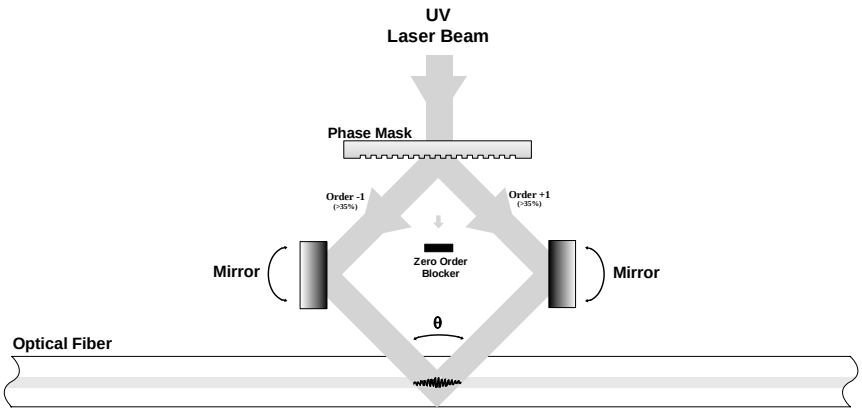

Figure 3.3 – Phase mask used as beam splitter.

This scheme allows wide wavelength tunability and it may have any type of grating which can also be replicated and translated to different wavelengths.

Additionally, if in the configurations shown in Figures 3.2 and 3.3 the incident UV beam and the phase mask/fiber are relatively and accurately displaced, arbitrary apodized and chirped gratings can be fabricated. Based on this, a technique called moving fiber/phase mask scanning method, that also allows tuning the Bragg wavelength, has been demonstrated [29]. The setup is similar to previous mask scanning configurations [20, 172], but with the difference that the fiber, or alternatively the phase mask, is slowly moved while the incident UV beam is being scanned, overcoming many of the limitations associated with phase masks. For uniform motions of the mask and/or the fiber, the relative movement results in a shift of the Bragg wavelength. If λ_0 is the unshifted Bragg wavelength, v_f and v_{sc} are the fiber and scanning beam velocities (with $v_f << v_{sc}$), respectively, the wavelength shift is given by

$$\Delta\lambda = \lambda_0 \frac{v_f}{v_{sc}} \tag{3.5}$$

Thus, for a shift of ~1 nm, the fiber must move at only 0.1 % of the UV beam scanning speed. An important aspect that should be taken into account is that for larger wavelength shifts, the grating strength decreases, since the refractive index modulation is averaged when the fibre moves too quickly across the interference pattern formed by the mask. The grating reflectivity, R, decreases with the wavelength shift as [29]

$$R \sim \mathrm{sinc}^2\left(\frac{\pi D v_f}{\Lambda_g v_{sc}}\right) = \mathrm{sinc}^2\left(\frac{2n_{eff}\,\pi D \Delta\lambda}{\lambda_0^2}\right) \tag{3.6}$$

where D is the writing beam diameter and n_{eff} is the effective refractive index (λ_0=2 n_{eff} Λ). From (3.6), it can be seen that R=0 for $v_{f,\ max}=\pm\Lambda v_{sc}/D$ or $\Delta\lambda_{max}=\lambda_0^2/2n_{eff}D$. Therefore, if the initial fiber velocity is set to $v_{f,\ max}$ and linearly decreased to $-v_{f,\ max}$ during the course of writing the grating, the result will be not only linearly chirped (across $2\Delta\lambda_{max}$), but automatically apodized with a *sinc* profile. This modified phase mask technique is the basis of the experimental effort carried out in this work.

3.2 The phase mask dithering/moving technique

A flexible writing method for advanced gratings using a single exposure step can be implemented by the phase mask dithering/moving technique. Basically, this method uses controlled dithering of the phase mask or the fiber/waveguide in order to control the local grating visibility and phase, without affecting the average refractive index. High dithering amplitudes destroy the interference pattern created by the phase mask at the fiber plane by fringe blurring. This corresponds to low visibility and results in gratings with low induced refractive index modulation amplitudes, i.e., gratings exhibiting low reflectivity. Dithering is thus an ideal mechanism for varying the local strength of the grating without changing its local Bragg wavelength.

This technique allows writing of complex gratings of good quality with a standard uniform phase mask, and it is today one of the preferred methods for fabrication of the most demanding gratings, such as those used for dispersion compensation. Although this technique is very attractive, few of the intimate technological details have been published, the equipment is also rather expensive and the throughput per production line is modest when a high grating quality is needed, which may pose a problem for high-volume production.

In this work, implementation and development of the phase mask dithering/moving method were the main goals. The phase mask is slowly moved during the UV beam scanning, overcoming the limitations associated with the use of uniform phase masks. For apodized Bragg gratings, the phase mask is dithered according to the profile defined for each position along the grating, resulting in high refractive index modulation amplitude (for low dithering amplitude) or low modulation amplitude (for high dithering amplitude), while maintaining a mean refraction index change along the total grating length. For chirped Bragg gratings, the phase mask is displaced with a non-uniform velocity along the grating length, resulting in a variable relative ratio between the phase mask and the beam scanning velocities. Phase shifted Bragg gratings are achieved by a very well quantified and

controlled displacement of the phase mask in the correct position or positions of the grating during its photoinscription. This allows structuring of the grating spatial modulation profile, in order to obtain gratings with variable phase steps, or more complex structures like sampled Bragg gratings.

In this section, the experimental setup implemented is explained, followed by the description of the control software. The basic calibrations used are also presented.

3.2.1 Experimental setup description

The experimental setup developed for gratings fabrication is shown in Figure 3.4.

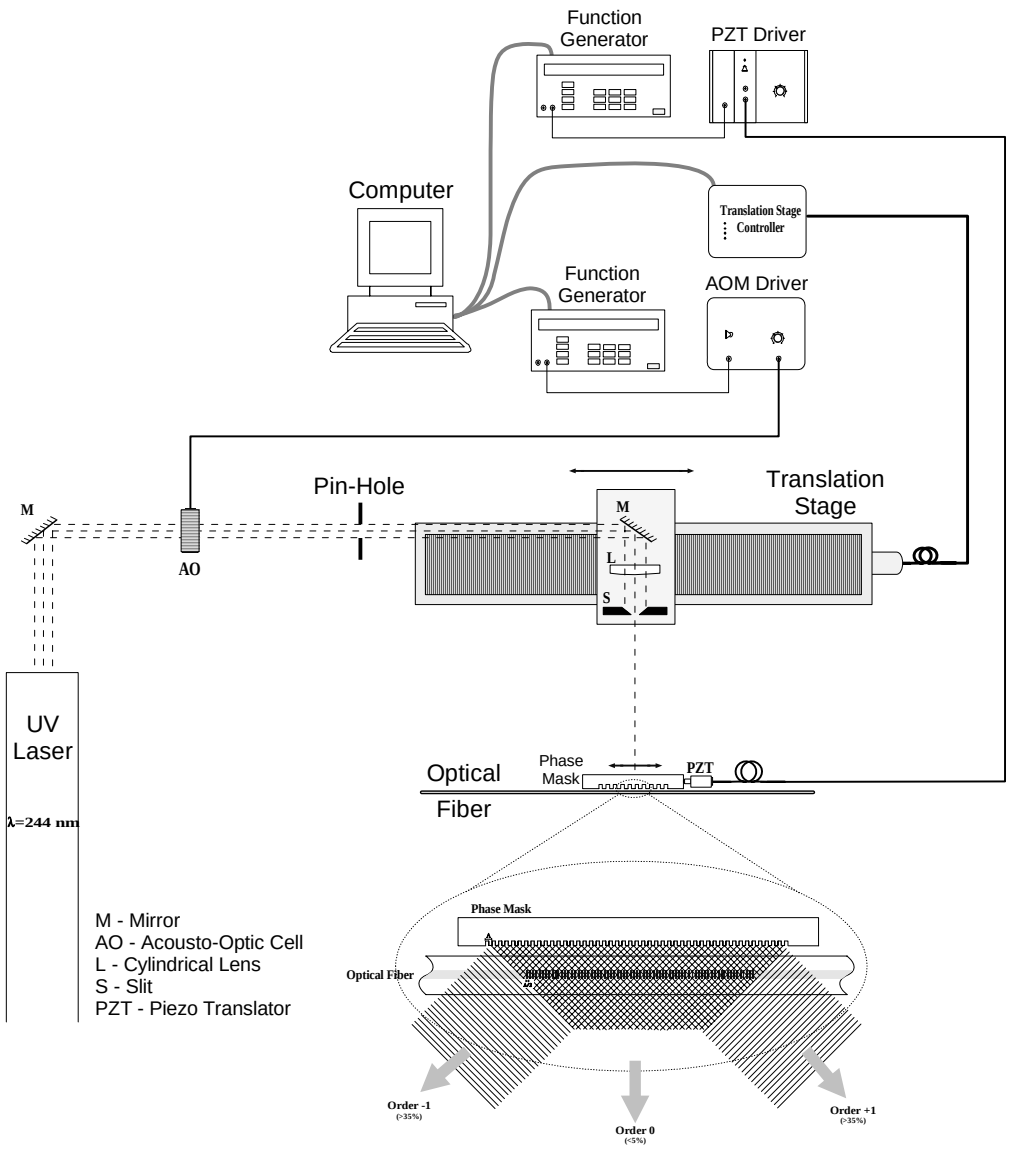

Figure 3.4 – Experimental setup for fibre/planar waveguide gratings photoinscription.

The optical source used for the photoinscription is a frequency doubled CW Argon laser (Coherent Innova® Sabre® Fred™) operating at 244 nm with a maximum output optical power of 500 mW at this wavelength. The UV laser beam, (~1 mm diameter), is then directed to an acousto-optic modulator (AOM) by a mirror. The modulator (AA.MQ.80/A2 from *A.A.-Automates et Automatismes*) controls the power passing through it by deflecting the incident beam from the order 0 to the order +1 according to the voltage applied to the cell by the AOM driver (AA.MOD.80-4W from *A.A.-Automates et Automatismes*). The maximum efficiency of the AOM is 85%. The beam is then spatially "cleaned" by a pin-hole that also filters the order 0. A mirror, a cylindrical lens and a slit are mounted on a translation stage in order to have the ability to scan the beam over different and desired grating lengths. The cylindrical lens (f=30 mm) is used to focus the beam on the photosensitive waveguide, and the slit, with micrometer resolution, controls the lateral dimension of the beam incident on the waveguide. The translation stage (Schneeberger TMF3 with power chassis TPP1/2) has a maximum resolution of 0,08 μm and a maximum displacement distance of 20 cm.

The phase mask is placed on a proper machined aluminium holder which can be dithered and/or displaced by a Piezo Translator (PZT). It is basically a two arm deflector with enough stiffness to allow the mask to follow the PZT movement when it is dithered at frequencies in the order of 10 Hz. The PZT (P-841.10 from PI-Physik Instrument), has a resolution of 0,3 nm and a maximum displacement distance of 15 μm, and is controlled by an amplification LV-PZT (Low Voltage PZT) module (E-505.00) connected to a sensor module (E-509.X1).

Both the PZT and the AOM drivers are controlled by independent synthesized function generators (Model DS345-30MHz from Stanford Research Systems).

The fibre or planar waveguide is then placed after the phase mask, in the focal plane of the lens. The sample is positioned with the help of a microscope, allowing the parallelism and distance between the sample and the phase mask to be adjusted at any time. In the case of optical fibers, the vertical alignment is performed simply by the visualization of the diffraction pattern on a target behind the fiber and when illuminated by the UV laser beam.

Figure 3.5 is a photograph of the laboratory showing the writing setup. It is also visible the Michelson interferometer that allows the visualization (by the interference fringes displacement) of the dither/displacement of the phase mask, since one of the mirrors is placed in the two arm deflector holder where the phase mask is fixed. The purpose is only to give a visual inspection of the phase mask behaviour at each position along the grating, since that any dither amplitude change is clearly identified. Also, an important feature of having this interferometer implemented is that it allows the detection of any kind of vibrations, totally undesirable, that can be present is the system.

As a matter of fact, the UV laser can transmit vibrations to the optical table simply because of the circulating cooling water around the cavity. To avoid this, care was taken and the laser placed on special air insufflated rubber feet that can absorb the vibrations.

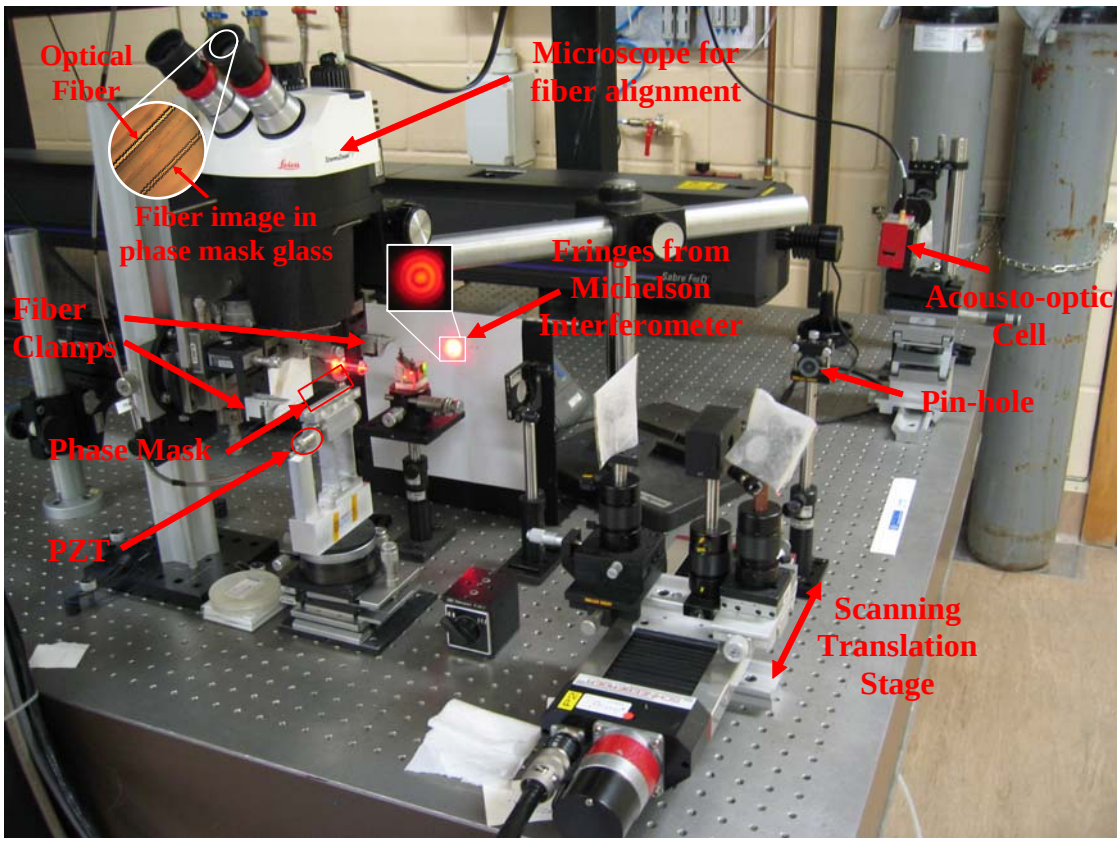

Figure 3.5 – Photograph of the laboratory showing the experimental setup for fiber gratings photoinscription.

3.2.2 Developed software description

The system is totally computer controlled by a LabView™ based program developed for this purpose. The control panel of the program is shown in Figure 3.6.

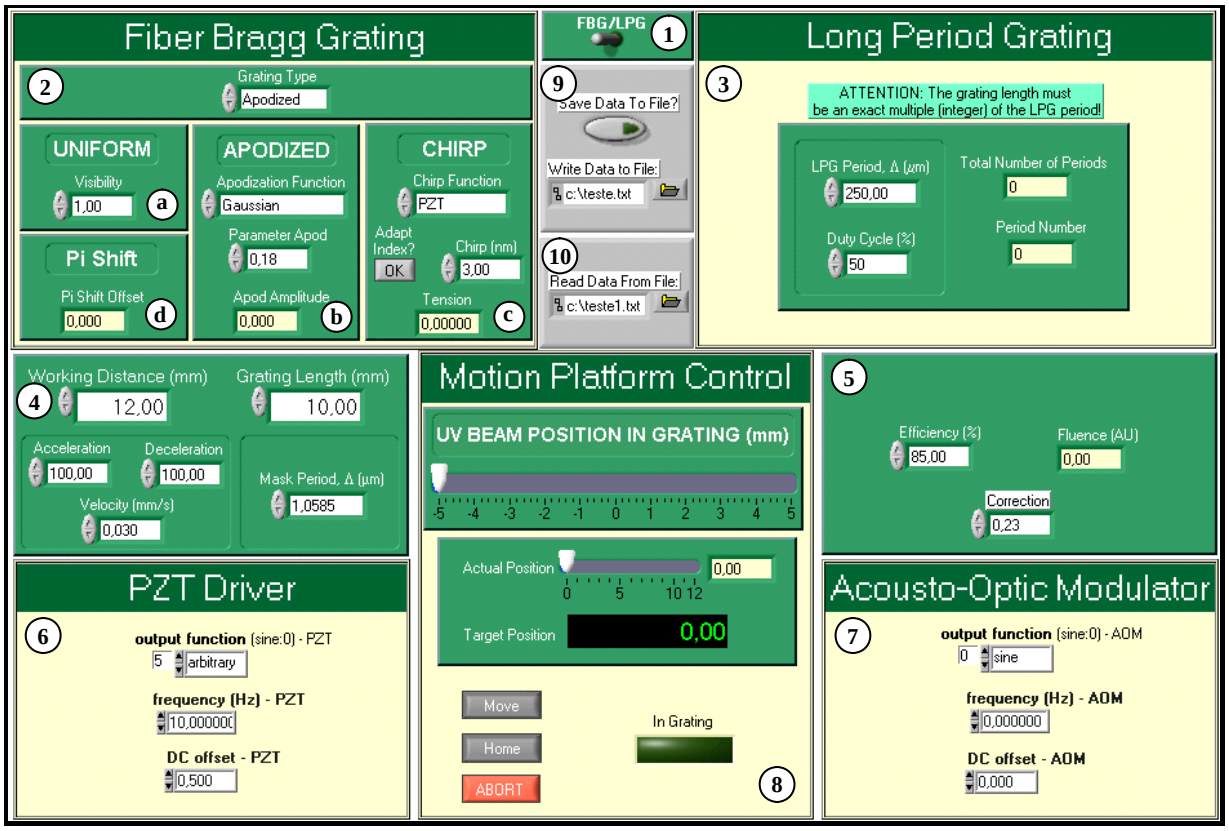

Figure 3.6 – Control panel of the LabView™ based program developed for the experimental setup control.

The control panel is divided in several frames. In Figure 3.6 they are clearly identified and it is now important to describe the functionalities of each.

Frame 1: This switch should be used to choose the kind of grating to be written, Bragg Grating or Long Period Grating (FBG/LPG).

Frame 2: Allows the selection of the type of Bragg grating to be written:

a) *Uniform Bragg gratings* – It is allowed to change the visibility between 0 and 1, i.e., for a visibility of 1 one should be able to produce a Bragg grating with maximum reflectivity (corresponding to no dithering on the phase mask) and for a visibility of 0 one should produce a grating with zero (or nearly zero) reflectivity (corresponding to the maximum dither of the phase mask calculated in order to destroy the interference pattern by fringe blurring);

b) *Apodized Bragg gratings* – In this frame, the user is allowed to choose between the programmed apodized profiles to perform apodization. Gaussian, raised cosine,

Blackman and sinc are some examples of the pre-defined functions. Also the capability of reading the profile from a text file (where there should be two columns, the first with the position on the grating in millimetres and the second with the normalized relative refractive index change) is available. This allows the realization of any kind of apodization function or profile without the need of computing it inside and while executing the program for Bragg grating inscription. The reading value ("Apod Amplitude") is the corresponding amplitude voltage applied to the PZT for the dithering of the phase mask;

c) *Chirped Bragg gratings* – There are two main functions in this frame, allowing the user to change between positive or negative chirp. Positive or negative chirp are referred to the fact that the phase mask displacement and beam scanning movement during grating exposure are made in the same or opposite directions, respectively. The reading value ("Tension") is the corresponding offset voltage applied to the PZT for the displacement of the phase mask. The "Adapt Index" control allows to make a smooth transition between the induced and the unperturbed refractive indexes, by increasing/decreasing the cell efficiency value at the ends of the grating;

d) *Phase Shifted Bragg gratings* – In this case there is a pre-definition for a Pi-shift Bragg grating in the program. By this, a displacement of the phase mask is defined in the middle of the grating by a quantity related with the Bragg grating period. The reading value ("Pi Shift Offset") is the corresponding offset voltage applied to the PZT. A script can be written to allow the fabrication of multiple phase shifts on the same grating.

Frame 3: For writing Long Period Gratings (LPGs), this frame allows to choose the desired period and the corresponding duty cycle. The reading values "Total Number of Periods" and "Period Number" gives the user the information of the number of periods of the chosen LPG and the evolution during the grating inscription, respectively.

Frame 4: In this frame the user must define the main parameters regarding the grating length, beam scanning velocity and phase mask period. The working distance should be always higher than the grating length, avoiding in this way the acceleration and deceleration movements performed by the translation stage, and assuring a uniform scanning velocity of the beam inside the grating. The

phase mask period introduced here is then used for the calibrations of the voltage to be applied to the PZT.

Frame 5: The efficiency value of the acousto-optic cell can be adjusted with a value between 0 and 85%. This allows the control of the incident UV beam power on the fibre/waveguide. Also available is a parameter called "Correction Factor". Its function is to introduce a correction value to the PZT calibration curve in order to compensate mechanical non-expected responses of the phase mask holder. The reading value "Fluence" is defined by the ratio between the efficiency and the scanning velocity.

Frame 6: Defines the function, frequency and offset to be applied to the PZT.

Frame 7: Defines the function, frequency and offset to be applied to the AOM.

Frame 8: Indicates the position of the beam while executing the beam scanning. Two indicators differentiate when the beam is writing the grating and when the absolute value regarding the working distance applies. Control buttons for "Move" and "Home" should be pressed on in order to allow the scanning and the returning of the translation stage to its initial/home position at the end of the grating inscription. An "Abort" button is also available to stop the process anytime during the execution.

Frame 9: Allows the scanning of a data file containing information about the kind of grating to be written and all the associated writing parameters (length, velocity, mask period, efficiency, PZT voltages, etc.). If selected the file path should be filled in the corresponding box.

Frame 10: Allows selection of the file path of the data file from which the apodization profile defined in frame 2-b will be read.

3.2.3 Basic calibrations

It has been stated in the previous sections that the control of the grating modulation profile during writing is achieved by a precise control of the phase mask dithering amplitude by a piezoelectric transducer (PZT), for each position of the UV beam over the fiber. Correct adjustment

of the dithering amplitude is then crucial to have a good control of the fringe visibility. This is easily achieved by changing the phase mask dither voltage as the writing beam is scanned across the fiber and therefore one is able to control the index modulation written into the fiber at each position. So, the way how the dither voltage applied to the PZT affects the refractive index modulation amplitude is one of the most important aspects when implementing this technique in a particular writing system. To calculate the resulting refractive index change, one can start by considering the superposition of spatially dependent waves, with different phase, corresponding to the pattern created by the mask at the fiber plane during one dither period. Thus, from the harmonic addition theorem, any superposition of harmonic and coherent waves

$$\psi(x) = \sum_{i=1}^{N} A\cos\left(2\pi \frac{(x + i\,\Delta x)}{\Lambda}\right) \tag{3.7}$$

where A corresponds to the amplitude of each, Λ represents the period of each wave (and will correspond to the period of the resultant wave), and $x+i\,\Delta x$ is the position of wave i (in the limit, $x+N\,\Delta x$ corresponds to the position of the wave resultant from the maximum displacement induced in the phase mask), which is by itself an harmonic wave. The amplitude variation of this resultant wave gives the information of the refractive index modulation that can be achieved.

However, the calibration curve for how the grating amplitude varies with dither amplitude depends also on the periodic function describing the oscillatory motion of the phase mask. As an example, the simulation of a square and a triangular dither function will be presented using (3.7). For simplicity, the amplitude variation of the resultant wave is normalized, and represented in terms of fringe visibility. The dither amplitude is represented in units of the grating period, Λ_g, normalizing Λ to 1. For the square function, N=2 (representing the two states of the square wave function in a period) and Δx = dither amplitude, and normalized to a grating period, so that a dither amplitude of 0.5 corresponds to a displacement equal to half of a grating period. For the triangular function, N=100 and Δx = dither amplitude/N, which results in dividing a function period into 100 small sections, i.e., superposition of 100 harmonic waves, in order to simulate the continuous linear movement that this function induces, unlike the first case that is represented by a discrete two step function. Also in this second case, a dither amplitude of 0.5 corresponds to a displacement equal to half of a grating period. Thus, Figure 3.7 shows the fringe visibility versus dither amplitude for both the square and triangular dither functions.

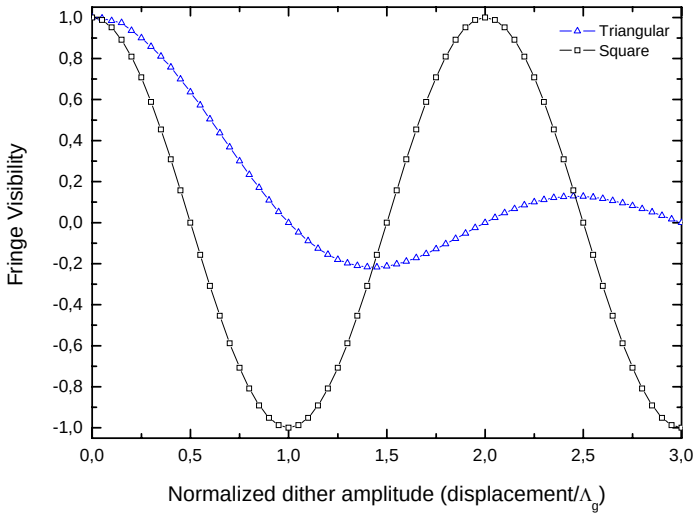

Figure 3.7 – Variation of fringe visibility with dither amplitude (in units of the grating period) for a square and a triangular carrier function.

As it can be confirmed from Figure 3.7, as the amplitude of the dithering is increased, the visibility of the grating fringes decreases until a certain value where the grating fringes disappear entirely; this point is referred to as the extinction amplitude. After this extinction point, the visibility of the fringes grows again, but now the written grating is 180 degrees out of phase relatively to its original position. This is known as over-dithering, and it produces a grating with an opposite phase to the one with dither amplitude below the extinction point. In Figure 3.7, this is shown by a negative fringe visibility. For the square wave dithering function, the visibility varies cosinusoidally with increasing dither amplitude, while for the triangular dither function the visibility shows a *sinc* like behaviour.

For this work, and in terms of the experimental application, the interest of the calibration curves shown in Figure 3.7 is restricted to the positive fringe visibility values between dither amplitude points ranging from zero to one grating period. Also, for experimental applicability in this work, as shown latter on, the axes should be interchanged, and the dither amplitude displayed as a function of the fringe visibility, or as it will be called from now on, as a function of the normalized index modulation. This representation is shown in Figure 3.8.

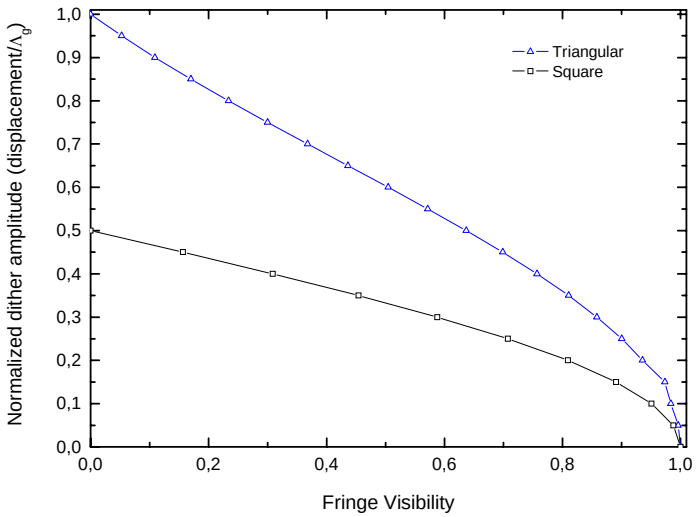

Figure 3.8 – Dither amplitude (in units of the grating period) as a function of the normalized modulation index for a square and a triangular carrier function.

From Figure 3.8, it can be seen that using a triangular carrier function, the extinction point, i.e., the dither amplitude value for which the modulation amplitude of the grating is completely destroyed, corresponds to one grating period (or alternatively, using (3.3) to half the phase mask period). For square excitation, this value is half the grating period, which corresponds to one quarter of the phase mask period. A polynomial fit for the two curves of Figure 3.8 results in the following polynomials

$$y_{Triang} = 0.99912 - 0.62467x - 8.1361x^2 + 77.903x^3 - 337.98x^4 + 783.33x^5 - 1000.1x^6 + 662.76x^7 - 178.09x^8 \quad (3.8)$$

$$y_{Square} = 0.49984 + 0.086216x - 5.1628x^2 + 23.076x^3 - 46.994x^4 + 44.287x^5 - 15.781x^6 \quad (3.9)$$

with correlation coefficients of 0.99978 and 0.99936 for the triangular (3.8) and square (3.9) functions, respectively, and y represent the dither amplitude and x the normalized modulation index, Δn_{Norm}. This calculation is of extreme importance, and can define a good performance or not of an experimental system. It is most of the times found and confirmed empirically [173, 174].

However, this is not the only calibration curve used in this work. There are two more important curves, which depend on the response of two components of the writing system. One is the displacement response of the PZT with applied voltage, and the other is the efficiency of the acousto-optic cell also with applied voltage. For the first case, a PZT performance test document was supplied by the manufacturer describing a quasi-linear response (maximum nonlinearity of

0.256 % at 5.5 V) of the displacement as a function of applied voltage given by the following equation

$$Displacement = 1.500554 \times AppliedVoltage \tag{3.10}$$

where the displacement is in micron and the voltage in units of Volt.

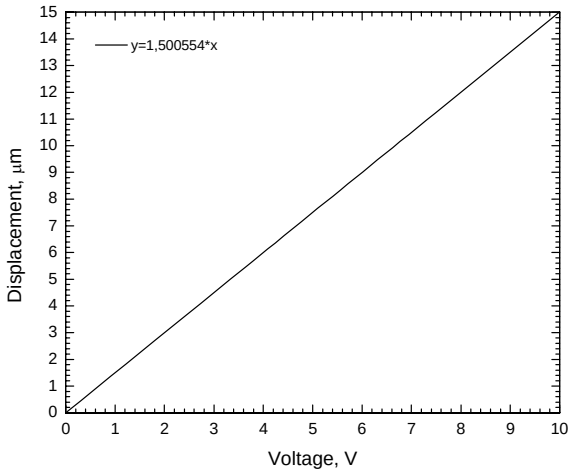

Figure 3.9 – PZT calibration curve.

As it can be seen from the PZT calibration of Figure 3.9, the PZT has a maximum expansion of 15 μm for an applied voltage of 10 V.

The calibration curve of the acousto-optic cell was obtained experimentally by applying different voltages, V_{AO}, and measuring the power transferred from the zero order to the order +1. In this work, the acousto-optic cell is used as a deflector, transferring the power from order 0 to order +1 by the application of a voltage. This calibration was found to have the behaviour shown in Figure 3.10.

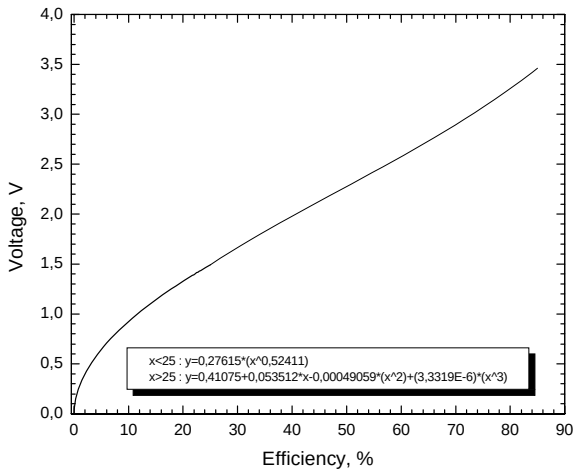

Figure 3.10 – Acousto-optic cell calibration curve.

The curve displayed in Figure 3.10 was fitted by two different functions, one describing its response from 0 % to 25 %, and the other from 25 % to 85 %, the maximum obtainable efficiency, *E*, for this cell. These fit functions are:

$$V_{AO} = \begin{cases} 0.2765 \times E^{0.52411}, & E < 25\% \\ 0.41075 + 0.053512E - 0.00049059E^2 + 3.3319 \times 10^{-6} E^3, & E > 25\% \end{cases} \tag{3.11}$$

For a maximum efficiency, an applied voltage of 3.46 V is required.

In conclusion, there are three main calibration curves used in this work: the dither amplitude versus the normalized index modulation; the PZT displacement versus the applied voltage; and the applied voltage versus acousto-optic cell efficiency. With the first, one is able to control the induced modulation index, Δn, without affecting the average refractive index. With the second, one can convert the desired displacement into voltage, so that the control voltage to apply to the PZT corresponds to the desired dither amplitude. With the third, one can control the UV power that illuminates the fiber. By applying more or less voltage to the acousto-optic cell, more or less writing power (and in consequence higher or lower index change) is achieved.

To finalize, and as an example, Figure 3.11 shows how some of these calibration curves are integrated in the system. A Gaussian apodization profile and a triangular wave dithering function were used.

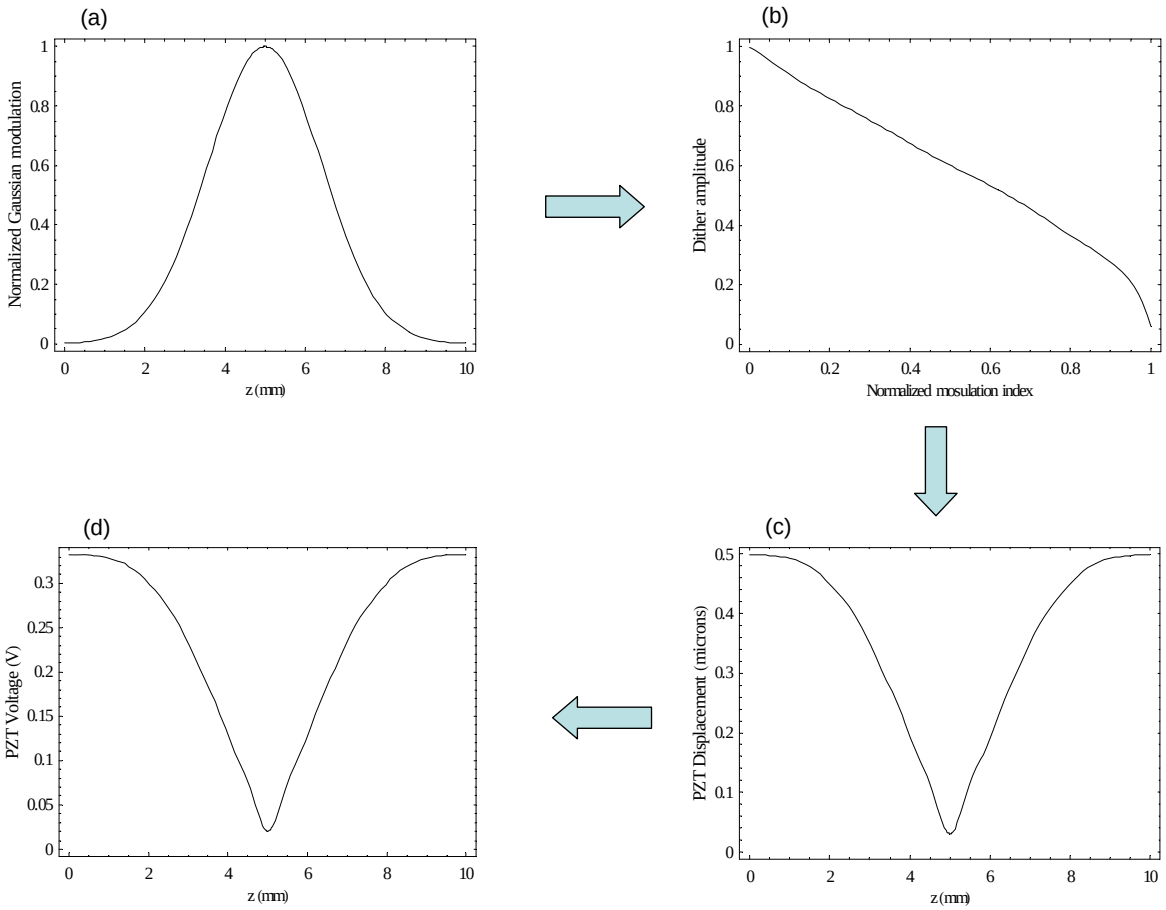

Figure 3.11 – Example of implementation of the Gaussian apodization profile using the required calibrations.

First of all, the desired spatial profile function should be introduced. In the case of Figure 3.11, a Gaussian profile, as described by equation (2.66), for a 10 mm grating is displayed – (a). After having the normalized modulation profile, the PZT displacement (dithering amplitude) for each grating position can be derived by using one of the calibration functions showed in Figure 3.8. In this example, the triangular dithering function is used – (b), and so the equation (3.8) is applied, allowing one to achieve the PZT displacement as a function of the grating length – (c). Finally, using the PZT calibration curve (shown in Figure (3.9) and given by (3.10)), the necessary voltage at each grating position is obtained – (d). As it can be seen, a dither amplitude of 0.34 V (peak-to-peak) is needed to destroy the interference pattern, and wash out the modulation index at both grating ends.

The example of Figure 3.11 gives a perspective of the interactions needed to put the system working properly for a given modulation profile. These interactions are introduced in the LabView™ software by means of a formula node (that uses C programming language), as represented in Figure 3.12. As it can be seen, the input variables are the grating position, z, that is read in real time, the total grating length, L, and the grating period, Λ_g, which are introduced in the front panel of the

software (remember that the grating period is half the mask period). The output variable is the PZT voltage, V, and is updated in real time for each grating position, while the writing beam is scanning the phase mask.

```
z   float gauss;
    float FWHM;
    FWHM=L/3;
L   gauss=exp(-(4*ln(2)*(z-L/2)**2)/(FWHM**2));

Λg                                                                    V
    /* triangular */
    V=(((0.99912-0.62467*gauss-8.1361*(gauss**2)+77.903*(gauss**3)-337.98*(gauss**4)+783.33*(gauss**5)-
    1000.1*(gauss**6)+662.76*(gauss**7)-178.09*(gauss**8))*Λg)/(1.500554));
```

Figure 3.12 – Application of the example of Figure 3.11 in the LabView™ system control software.

3.3 Conclusion

Fabrication methods of Bragg gratings were presented in this chapter. Special attention was dedicated, of course, to the experimental setup implemented for the phase mask dithering/moving technique. The description of this setup and the developed control software (in LabView™) was presented, followed by the required calibration functions. These include the analysis for the correct adjustment of the phase mask dithering amplitude for each visibility and the acousto-optic diffraction cell efficiency response curves to applied voltages. Finally, integration of these calibration functions in the implemented system was described.

4 Fabrication and characterization of Bragg gratings

4.1 Introduction

In this chapter, experimental results from complex Bragg grating structures fabricated by the phase mask dithering/moving technique using a standard uniform phase mask are presented. As already mentioned, the particular advantage of this method is that a particular grating can be tailored or structured in order to fit a desired application using a standard uniform phase mask. This chapter starts by addressing the characterization methods and setups used in this work for an evaluation of the Bragg gratings performance. It is followed by a description of the experiments implemented to verify the calibrations described in 3.2.3, showing the problems encountered and adjustments that were made in order to correct those problems. Studies of the functionalities of the setup and the variation of the main parameters are shown, giving the information for Bragg gratings writing. Complex structures, like apodized, chirped and phase shifted Bragg gratings in optical fibers are demonstrated, showing the enormous potential of this technique. Finally, Bragg gratings written in planar waveguides using the proposed technique are presented, including also the modifications implemented in order to allow processing of integrated optic planar structures.

4.2 Characterization of Bragg gratings

A written fiber Bragg grating (FBG) is often analyzed by the examination of the reflected power spectrum. This is very limited in the indication of the origins of errors that can degrade the spectral quality, but is a fast and efficient method just to have a first idea if the result is according to what was expected. Systematic problems, such as phase-mask imperfections, could be difficult to diagnose in this manner. Thus, the writing process often involves a process of trial and error, ending when the correct spectrum is achieved. The spectral measurements of the gratings presented in this chapter were carried out in real-time during UV writing and after the gratings were written, by illumination through a broadband source using an optical circulator and an optical spectrum analyzer (OSA) with maximum resolution of 0.5 nm, allowing in this way to obtain the reflection and the transmission spectrum (Figure 4.1a). In cases a high resolution measurement was required, a tunable

laser source with 0.1 pm wavelength resolution and low side spontaneous emission (high side mode suppression ratio - > 60 dB) was used in place of the broadband source and swept in wavelength over the grating reflection/transmission band. The power was measured using an optical power meter (Figure 4.1b).

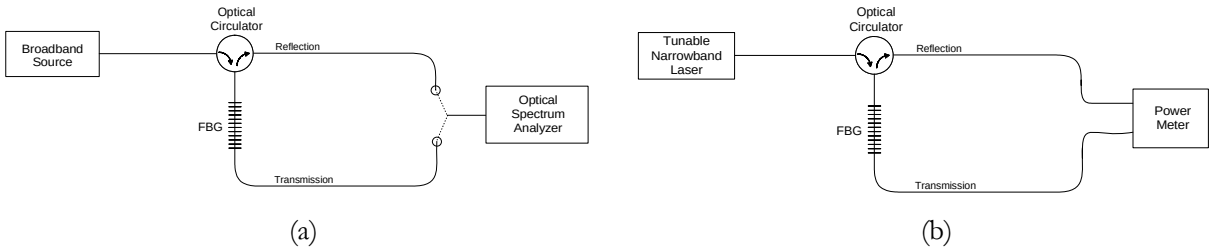

Figure 4.1 – Experimental setup for spectral characterization of Bragg gratings using (a) a broadband source and an OSA; and (b) a tunable laser source and an optical power meter for high resolution measurements.

For some applications, like dispersion compensation, is the temporal behaviour that is essential to determine its suitability for a given application. Therefore, it is of extreme importance to measure relative propagation delays as a function of wavelength in order to determine the chromatic dispersion. There are several methods for measuring chromatic dispersion, but each method has a particular fiber range and operating conditions in which the measurements will yield good results. For instance, in the phase-shift method, changes in the phase of a modulated pulse are measured and the accuracy of the phase method is determined by the design of the test equipment. Therefore, measurement of a phase change of an optical pulse that has travelled through the fiber will result in a measurement of the time delay, as well as the dispersion of the fiber.

The two phase-shift methods for measuring chromatic dispersion are the modulated phase-shift method and the differential phase-shift method. Both methods measure the phase shift of optical pulses propagating through the fiber as a function of frequency. Modulation of the intensity for both techniques is required. Chromatic dispersion measured by the modulated phase-shift method requires the amplitude of the input signal to be modulated by a reference signal and applied to the fiber under test. The transmitted signal is detected at the output of the fiber and the phase of the transmitted signal is compared to the reference signal used to modulate the input signal. The measured value for the modulated phase-shift method is the group delay corresponding to a wavelength interval. The chromatic dispersion can be calculated by taking the derivative of the group delay with respect to wavelength and dividing it by the wavelength. This measurement is repeated at different wavelengths.

The differential phase-shift method differs from the modulated phase method in that it measures the dispersion directly instead of the group delay. Just as in the modulated phase

technique, the amplitude is modulated. In the differential phase method, however, the wavelength is also modulated around a central wavelength where the group delay is to be measured. The detected signal not only has a phase difference but also varies with frequency. At the output end of the fiber, the transmitted signal is compared with the reference signal yielding the phase difference. To obtain the dispersion curve, the measurement is repeated for several wavelengths.

The dispersion measurements of the Bragg gratings fabricated in this work were carried out using the modulated phase-shift method. This measurement of such narrow-band devices requires high wavelength-resolution to accurately measure the relative group delay. For that, the setup of Figure 4.2 was implemented.

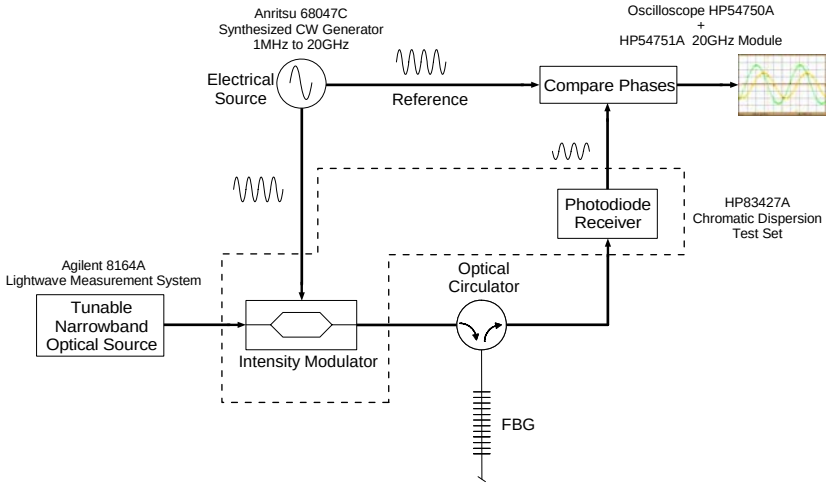

Figure 4.2 – Experimental setup for chromatic dispersion measurements by the modulated phase-shift method.

In operation, the output of a narrow band tunable laser source is intensity modulated and applied to the grating under test through an optical circulator. The reflected signal is detected and the phase of its modulation is measured relative to the electrical modulation source. The phase measurement is repeated at intervals across the wavelength range of interest.

4.3 Preliminary setup calibrations and Bragg grating studies

In order to confirm the calibrations referred in section 3.2.3 of this thesis, the next results are of extreme importance since they can determine the final quality of complex structures like apodized, chirped and phase shifted gratings. The study of how beam scanning velocities, incident

UV power and grating lengths affect the grating reflectivity, is presented in this section. It is not important to read this data as absolute values, since other key parameters should be considered, like, for example, the fiber photosensitivity. Thus, the results presented in this section are valid for the fiber type used and for the photosensitivity enhancement conditions employed, which is perfectly acceptable for the purpose of these experiments, since only a relative behaviour for each case was searched.

4.3.1 Phase mask dithering amplitude variation

Using the calibration curve of Figure 3.8 (with triangular PZT driving function), several uniform Bragg gratings were written, changing the writing visibility between 0 and 1. A visibility of 1 means that one should be able to produce a Bragg grating with maximum reflectivity (corresponding to no dithering of the phase mask) and that for a visibility of 0 one should produce a grating with zero (or nearly zero) reflectivity. Figure 4.3 shows the obtained grating reflectivities for different visibilities.

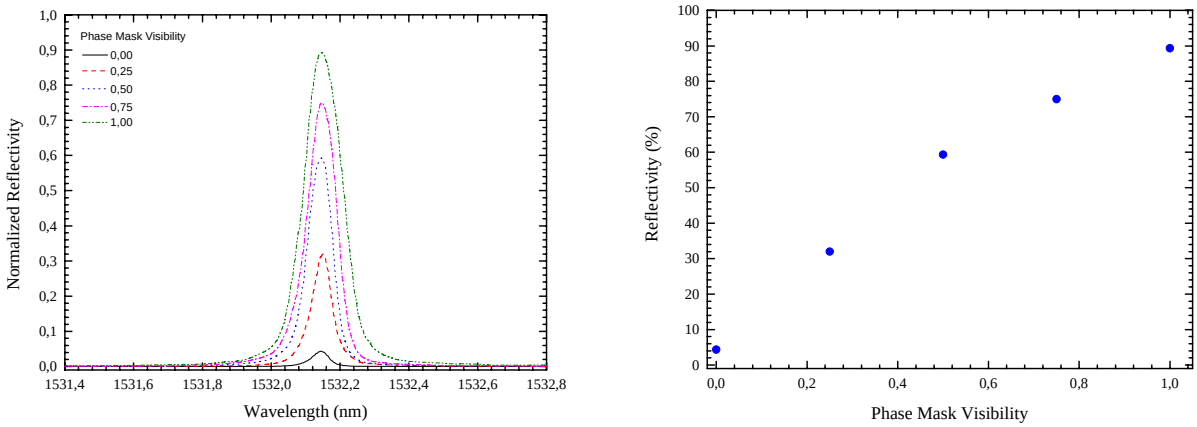

Figure 4.3 – 30 mm long uniform fiber Bragg gratings fabricated with different phase mask dithering amplitudes.

All 30 mm long uniform Bragg gratings were written in hydrogen loaded standard Single Mode Fiber (ITU-T G.652), with 50 mW of UV power incident in the phase mask (with a period of 1058.5 nm) and a beam scanning velocity of 30 μm/s. For each grating, the visibility was changed from 0 to 1, in steps of 0.25. For the writing conditions employed, the strongest grating presents a peak reflectivity of ~90 % and the weakest a peak reflectivity of ~4 %. The observation of a grating with 4 % reflectivity when maximum dithering amplitude is applied indicates that the dithering amplitude is not correctly calibrated in order to completely destroy the interference pattern created

by the phase mask. To check the mechanical stability of the PZT holder, one mirror of another Michelson interferometer was placed in the aluminum arm that holds the PZT. In principle, this arm should be static, but it was observed that small oscillations occurred, which meant that not all the translation movement was being transferred to the two arm deflector that holds the phase mask. Thus, the phase mask holder movement does not match exactly the movement of the PZT piston when a triangular function is used to drive the PZT. It was not a calibration function problem, but instead a mechanical one. With this new data in mind, other mechanical possible solutions were implemented for the aluminum holder, namely the reinforcement of the PZT arm holder. The need for other kind of optimization arose, namely the use of an arbitrary function to drive the PZT. This arbitrary function is basically a triangular function with some dwell times added to improve the mechanical response in the inversion points (see Figure 4.4-a). Secondly, a correction to the PZT calibration curve was performed by changing its slope (see Figure 4.4-b). The optimum value was achieved by finding the correct PZT dither amplitude that resulted in a grating with zero (or almost zero) reflectivity.

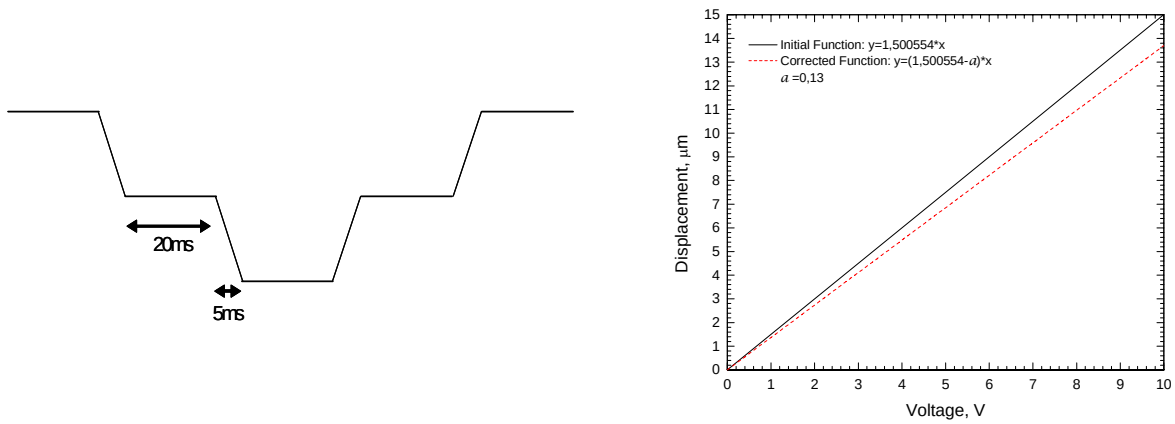

(a) (b)

Figure 4.4 – Corrections to the writing system to compensate bad mechanical response of the PZT/phase mask holder by (a) introducing and arbitrary PZT driven function and by (b) introducing a correction factor to the PZT calibration curve(a is the correction factor which has a value of 0.13).

Results of the tests using the same parameters as used in Figure 4.3 are now shown in Figure 4.5, already with the implemented corrections described above.

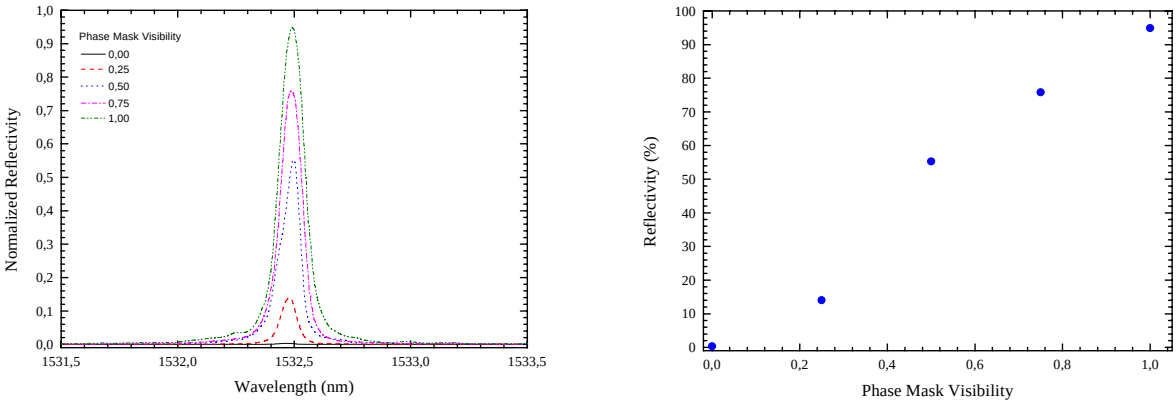

Figure 4.5 – 30 mm long uniform fiber Bragg gratings fabricated with different phase mask dithering, with software corrections and an arbitrary PZT carrier function.

Before the correction was performed, a grating with approximately 4% was measured when a visibility of zero was chosen. With correction in place, the weakest grating presents a reflectivity of 0.3 %. This difference indicates that the correction resulted in a reduction of the reflectivity by more than one order of magnitude, as it can be seen by the direct comparison shown in Figure 4.6.

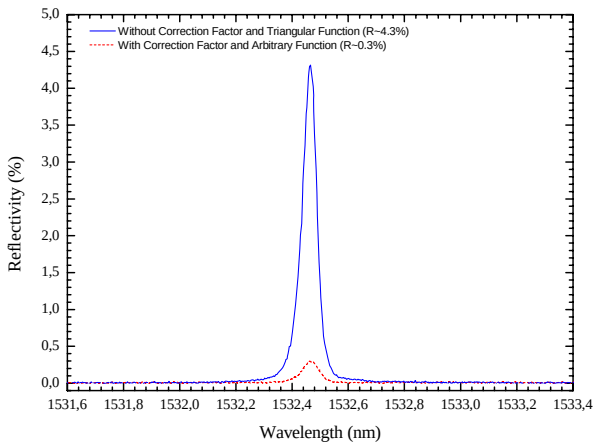

Figure 4.6 – Direct comparison of two fiber Bragg gratings written with zero visibility before and after corrections were made to the writing system.

4.3.2 Beam scanning velocity variation

An important feature of this setup is that the UV writing beam scans the phase mask by means of a mirror mounted in a translation stage. The dependence of the reflectivities (or refractive index change) of the gratings written with different scanning velocities should be known. To achieve

this, several gratings were written, each with a different scanning velocity. All the uniform Bragg gratings fabricated with a visibility of 1 were 30 mm long and were written in hydrogen loaded standard Single Mode Fiber (ITU-T G.652) with 50 mW of UV power incident in the phase mask (with a period of 1058.5 nm). The grating spectra were acquired and the peak reflectivity of each for the corresponding velocity was registered. The result of the maximum reflectivity as a function of the scanning velocity is shown in Figure 4.7, for velocities varying from 0.01 to 1.5 mm/s.

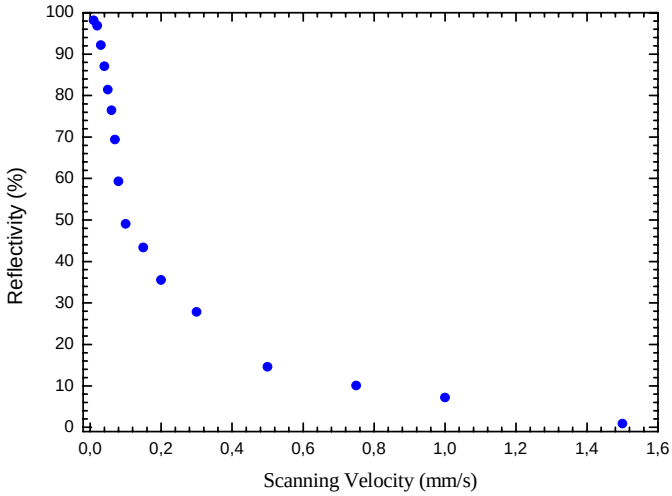

Figure 4.7 – Grating reflectivity versus beam scanning velocity.

As expected, the grating reflectivity decreases with increasing velocity since for faster scanning sweeps, the exposure time is shorter. This means that the fluence, defined as the ratio between the cell efficiency and the scanning velocity, is lower. By fitting the reflectivity values obtained for each velocity with equation (2.42), considering L=30mm, the graph of Figure 4.8 can be obtained. From it, one can see that for this fiber and for the writing conditions mentioned above, the maximum index change was $\sim 5.8\times10^{-5}$.

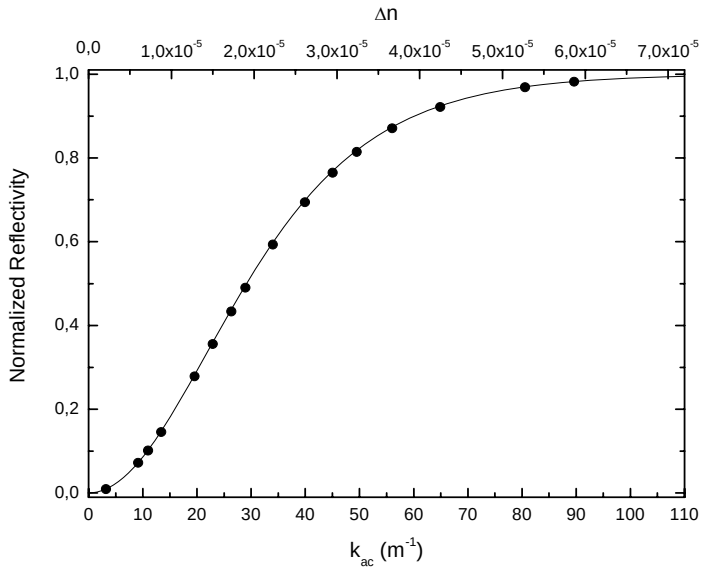

Figure 4.8 – Reflectivity versus k_{ac} and modulated index change, Δn, for the 30 mm gratings with peak reflectivities plotted in Figure 4.7 (λ_B=1532nm and η=0.75).

4.3.3 Writing UV beam power variation

Another way of controlling the grating reflectivity is by changing the incident UV power. As a change of the laser output power is most of the times not desirable since it can affect its pointing and output power stability, one way to control the power incident in the phase mask is by changing the acousto-optic cell efficiency value. Therefore, several uniform (visibility=1) gratings were written, each with a different cell efficiency value. All 30 mm long gratings were written in hydrogen loaded standard Single Mode Fiber (ITU-T G.652) with a scanning velocity of 30 μm/s, and with a UV power incident in the phase mask (with a period of 1058.5 nm) ranging from 5 mW (efficiency of 15 %) to 31 mW (efficiency of 85 %). The grating spectra were acquired and the peak reflectivity of each for the corresponding efficiency was registered. The results of the reflectivity as a function of the cell difraction efficiency are shown in Figure 4.9.

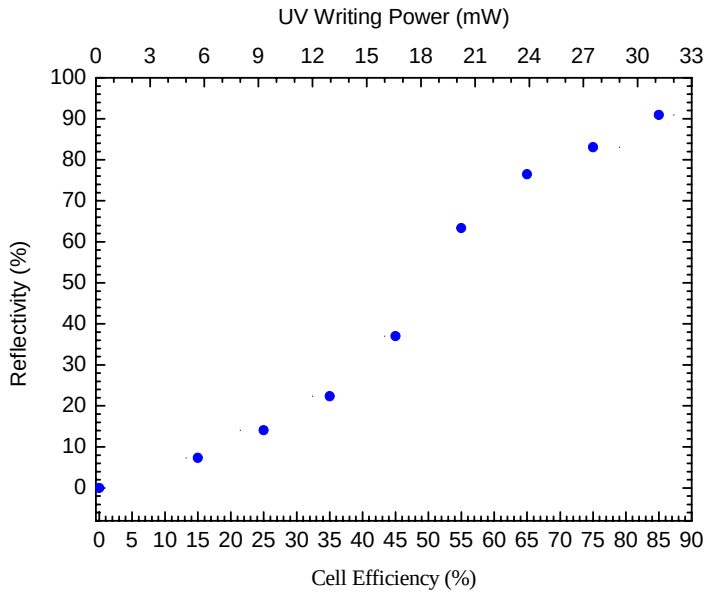

Figure 4.9 – Grating reflectivity versus cell efficiency (or writing power).

As expected, the grating reflectivity increases when the cell efficiency also increases. It behaviour should respect equation (2.42) since what is being affected once more is the index change (coupling coefficient), which should be higher for higher incident powers. Thus, by fitting the reflectivity obtained for each efficiency value (or corresponding measured incident power) with (2.42), considering L=30mm, the graph of Figure 4.10 can be obtained, allowing to estimate the values of the index change induced. From this, one can see that a maximum index change for this fiber and for the writing conditions mentioned above is $\sim 4\times10^{-5}$.

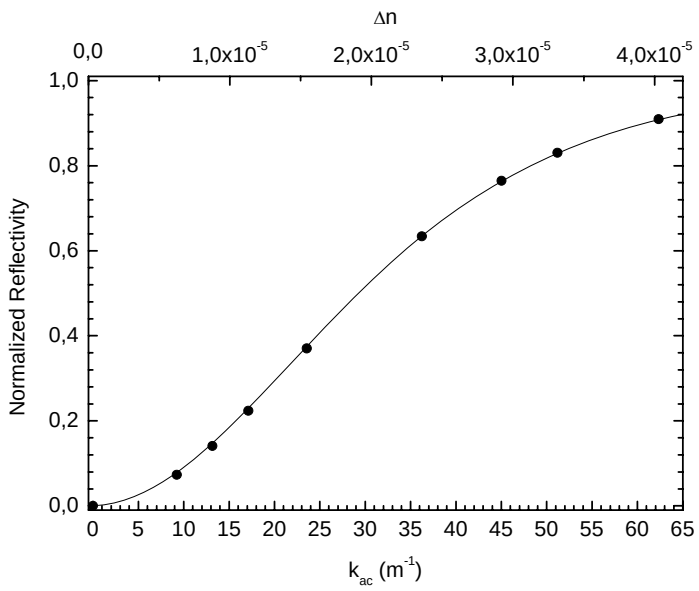

Figure 4.10 – Reflectivity versus k_{ac} and modulated index change, Δn, for the 30 mm gratings with peak reflectivities plotted in Figure 4.9 (λ_B=1532nm and η=0.75).

4.3.4 Grating length variation

The reflectivity of each grating also depends on its length. To observe such variation, several gratings were written, each with a different length, ranging from 5 to 30 mm, in steps of 5 mm. All the uniform Bragg gratings (visibility 1) were written in hydrogen loaded standard Single Mode Fiber (ITU-T G.652) with a scanning velocity of 30 μm/s, and with a UV power incident in the phase mask (with a period of 1058.5 nm) of 50 mW. The grating spectra were acquired and the peak reflectivity of each was registered. The results of the reflectivity as a function of the grating length are shown in Figure 4.11.

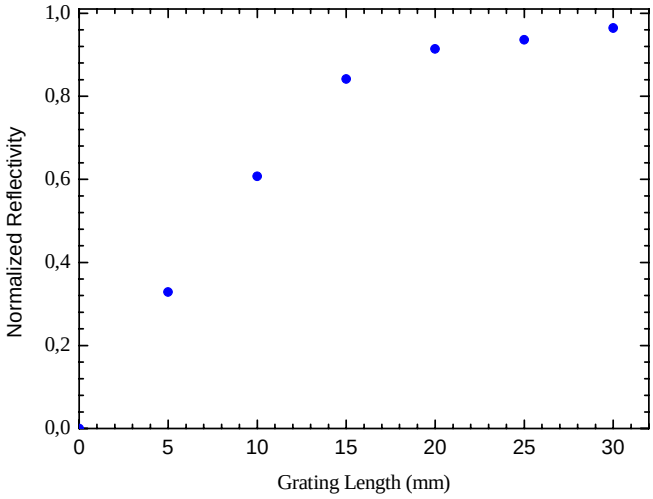

Figure 4.11 – Normalized grating reflectivity versus grating length.

As it can be observed, a maximum reflectivity of ~ 97 % is achieved for a grating length of 30 mm. For a 5 mm long grating, a peak reflectivity of ~ 33 % was registered.

4.3.5 High reflective fiber Bragg gratings

The maximum reflectivity of fiber Bragg gratings can depend on several parameters. First of all it will depend strongly on the waveguide photosensitivity, which can be enhanced by using the different techniques described in section 2.6. In what concerns the writing system, one can play with the fluence, either by changing the writing power or the scanning beam velocity, as demonstrated in the previous sub-sections. By increasing the writing UV power and/or reducing the beam scanning

velocity, gratings with high reflectivity can be achieved. Results of a fiber Bragg grating written with high fluence in an enhanced photosensitive fiber are shown in Figure 4.12. Also seen in Figure 4.12-b) is the transmission spectrum in logarithmic scale. It should be noted that the suppression level shown could be limited by the OSA noise floor.

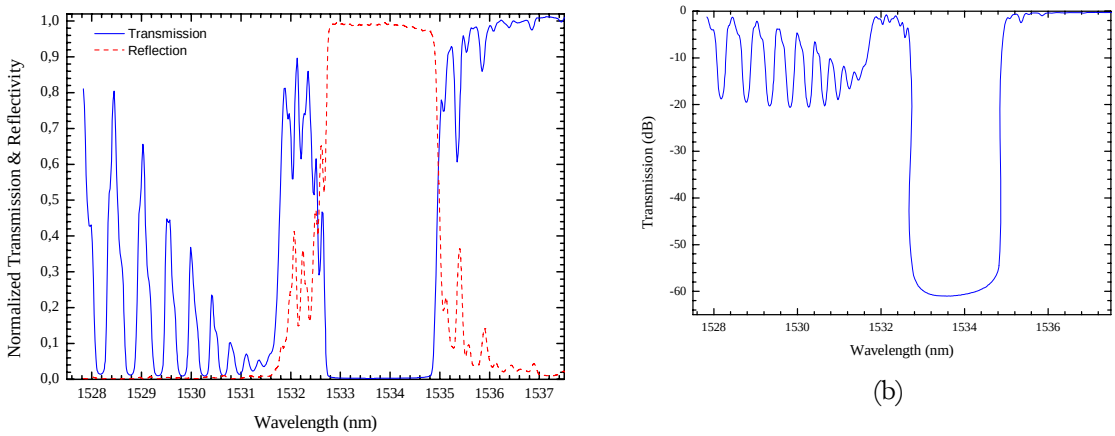

Figure 4.12 – Experimental results of high reflective fiber Bragg grating showing (a) reflection and transmission in normalized linear scale and (b) transmission in logarithmic scale.

The 7 mm long uniform Bragg grating was written in a hydrogen loaded photosensitive fiber (intrinsically high photosensitive fiber PS1500 from Fibercore) with a scanning velocity of 30 μm/s, and with a UV power incident in the phase mask (with a period of 1058.5 nm) of 80 mW. When compared to the results presented so far, it is clearly seen a big increase in grating reflectivity. This is especially due to the enhanced photosensitivity characteristics of the fiber used, achieved through boron and Germanium co-doping and high pressure room temperature hydrogenation.

Also, and as it can be seen from Figure 4.12, some very pronounced resonances appear on the short wavelength side of the Bragg peak, which become stronger when the grating reflectivity is higher. The grating has a bandwidth, $2\Delta\lambda$, of ~2 nm, that allows an estimation (equation 2.50) of the UV index change, Δn, of $\sim 1.8\times10^{-3}$. The multiple resonances at short wavelengths are a consequence of mode coupling between the core mode and several co-propagating cladding modes (this is the reason why resonances are only seen in transmission)[175, 176]. This effect becomes more noticeable when the Bragg grating becomes stronger and is due to an asymmetry effect in the refractive index modulation in the transversal direction. The cladding mode radiation related problems become very serious with large excess losses at wavelengths shorter than the peak reflection wavelength.

There are several ways to avoid or reduce this effect [177]. As a first example, this can be achieved by having a uniform photosensitive region across the cross-section of the optical fibre, and using suppression of the normalized refractive index modulation for this coupling [178]. A second method is based on instructing the coupling from the guided mode into cladding modes [179]. By introducing a depressed cladding with appropriate index and thickness, a substantial suppression of the coupling into the cladding modes can be achieved through a reduction of the cladding mode field strength.

The third option is to use a high numerical aperture (NA) fiber [180]. The gap between the main resonance wavelength (core mode) and the first cladding mode coupling wavelength is increased by using a high NA fibre, but this result in a useful operating band that is only about 7 nm wide. As an example, Figure 4.13 shows a 7 mm long fiber Bragg grating written in a hydrogen loaded intrinsically photosensitive fiber (SM1500 from Fibercore) with a scanning velocity of 10 μm/s, and with a UV power incident in the phase mask (with a period of 1058.5 nm) of 100 mW. The fiber used is highly co-doped with Germanium and has a NA of 0.3, which is a high value when compared to the NA of 0.13 of the previous fiber (PS1500). As it is clear from the figure, the resonant cladding modes appear far from the Bragg peak and not so pronounced. A wavelength spacing of more than 7 nm is measured.

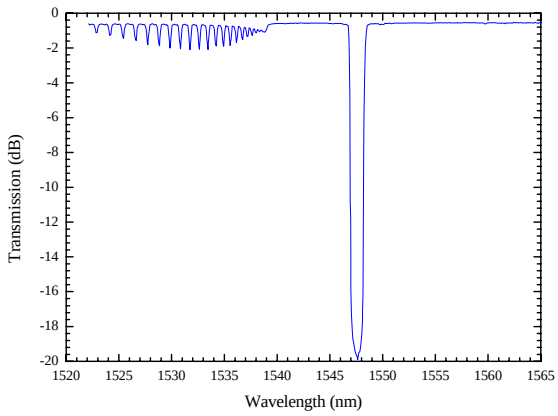

Figure 4.13 – Reduction of cladding mode resonances by using high NA fiber in high reflective fiber Bragg gratings.

4.4 Apodized fiber Bragg gratings

In this section, experimental results of apodized fiber Bragg gratings are presented. The apodization profiles used are described analytically (section 2.5.1) in the software. For each position along the grating, and according to the selected apodization function, the corresponding dither

amplitude is calculated and applied. However, generic apodization profiles obtained by simulation in other programs and using different techniques can also be implemented. The input to the software is thus a text file with two columns, the first indicating the grating position and the second the normalized index change required.

4.4.1 Direct spatial profile functions

Implementation of analytical apodization functions is the most straightforward approach to achieve side lobes suppression in Bragg gratings. Among the most popular profiles are the *Gaussian*, the *raised cosine* and the *sinc* functions, as described in chapter 2. An experimental comparison between a uniform Bragg grating and the mentioned apodized Bragg gratings using the corresponding spatial profiles given in section 2.5.1 (by equations (2.67), (2.68) and (2.70), respectively) are shown in Figure 4.14.

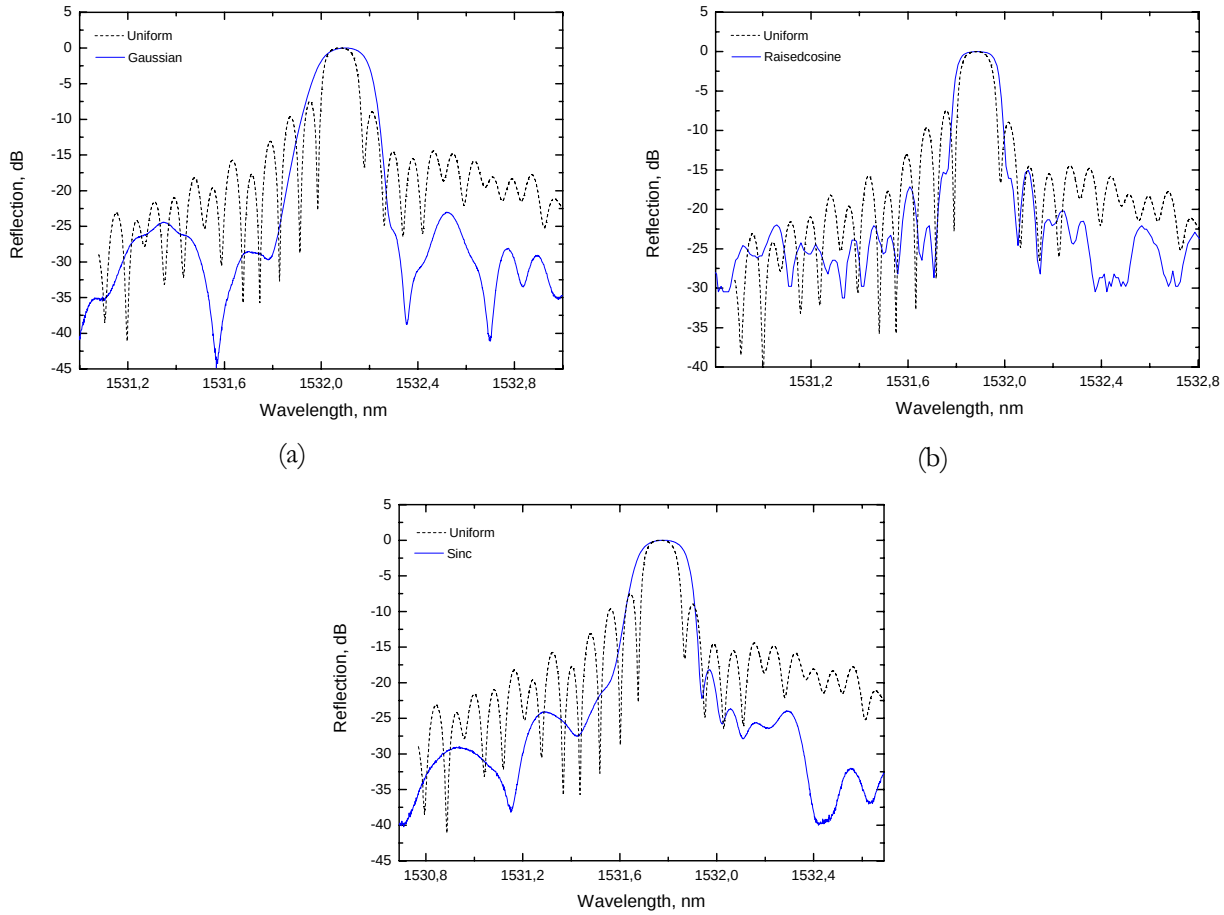

Figure 4.14 – Experimental comparison of a uniform Bragg grating and a (a) Gaussian, a (b) raised cosine and a (c) sinc apodized Bragg grating.

All gratings were fabricated in a hydrogen loaded standard Single Mode Fiber (ITU-T G.652), have peak reflectivities of around 90 % and it is clearly seen that side lobe suppression was achieved for every case, when directly compared with the uniform grating. Figure 4.15 shows a close-up view of all the fiber Bragg gratings for easier comparison.

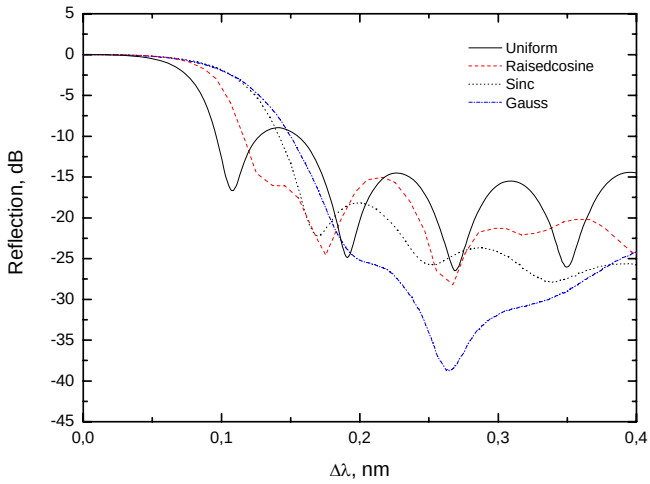

Figure 4.15 – Close-up view of the edges of the three apodized and the uniform Bragg gratings shown in Figure 4.14.

As it can be seen, the Gaussian apodization profile is the one that gives more side lobe suppression, while the raised cosine still presents a more clear side lobe structure, closer to the one obtained for the uniform case. These experimental results follow the simulations obtained in Figure 2.12.

4.4.2 Modelled spatial profiles

Sometimes and in order to achieve desired spectral and temporal responses of Bragg gratings, grating spatial profiles are generated by sophisticated synthesis techniques. Some examples are the genetic algorithm [181, 182] and the layer-peeling method [183-185]. The idea is to design the grating structure by numerical optimization using a certain merit function and a goal spectrum. Taking advantage of the participation in project PLATON (PLAnar Technology for Optical Networks), some modelled profiles using these techniques were supplied by the project partners (namely TUHH - Technische Universität Hamburg - Harburg). One example is the profile shown in Figure 4.16.

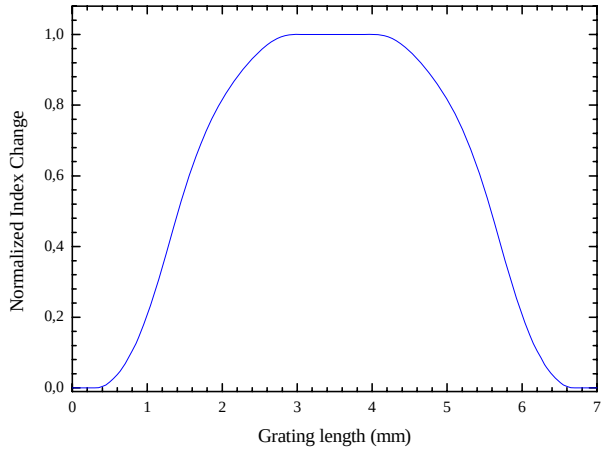

Figure 4.16 – Apodization spatial design#1 provided by TUHH.

This profile, supplied in a text file with two columns, the first indicating the grating position and the second the normalized index change, was introduced in the software as described in section 3.2.2. Fiber Bragg gratings were then written in hydrogen loaded standard Single Mode Fiber (ITU-T G.652). Figure 4.17 shows two examples of the fabricated gratings using the profile displayed in Figure 4.16.

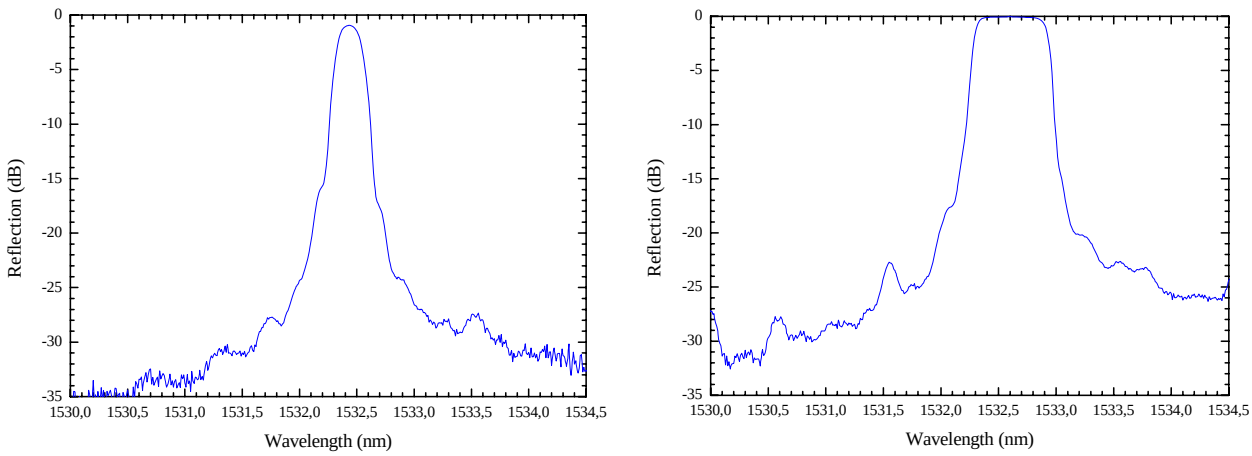

(a) (b)

Figure 4.17 – Fiber Bragg gratings fabricated using the spatial profile shown in Figure 4.16 presenting reflectivities of (a) 78 % and (b) 99 %.

Grating (a) have a measured transmission filtering level of ~6.7dB (78 % reflectivity), while grating (b) has a value of 20 dB (99 % reflectivity). The reflection spectra show that good side lobe suppression was achieved, even for the high reflectivity grating. To confirm that the results were according to the desired profile, reconstruction of the spatial distribution of the coupling coefficient

was performed using coherent optical frequency domain reflectometry (OFDR) [186]. Thus, grating of Figure 4.17-a) was reconstructed spatially and the result shown in Figure 4.18.

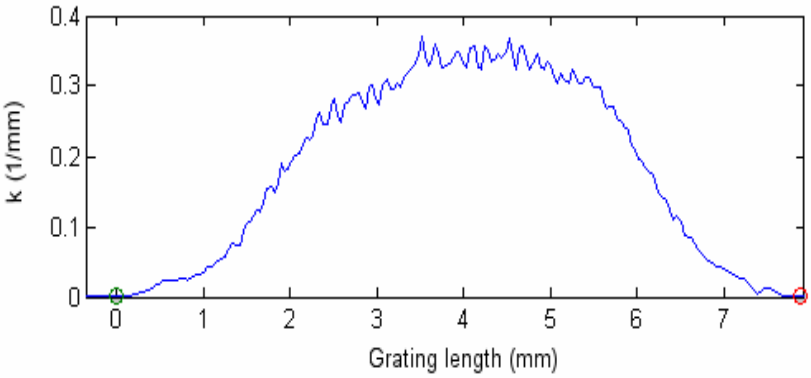

Figure 4.18 – Measured magnitude of k_{dc} (z) of the grating of Figure 4.17-a) using optical frequency domain reflectometry (OFDR).

The peak reflectivity of the grating is 78 % which corresponds to a calculated k_{dc} (by using equation (2.42) and considering $k_{ac}=k_{dc}/2$) of 0.39 mm^{-1}. The magnitude of the coupling coefficient of the reconstructed grating is thus in good agreement, as well as the overall obtained shape profile, when compared to the one of Figure 4.16.

To simultaneously achieve high reflectivity (>99.9 % ⇒ 30 dB) and high side lobe suppression (>25 dB@ ±0.6 nm) suitable to DWDM applications, another modelled spatial profile (supplied by TUHH, Germany) very similar to the one of Figure 4.16, but adjusted to fulfil the above performance, is represented in Figure 4.19. It was implemented in the experimental setup using hydrogen loaded fibers with high Germanium doping levels.

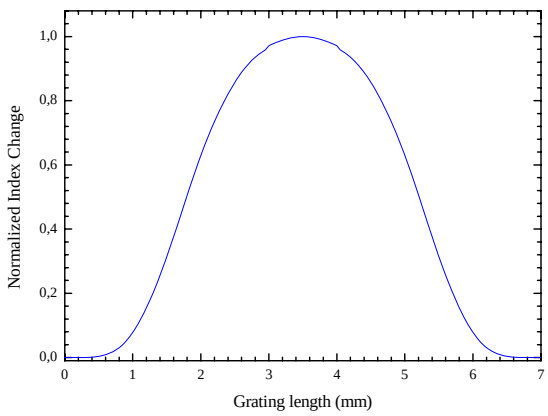

Figure 4.19 – Apodization spatial design#2 provided by TUHH.

Results for this profile are shown in Figure 4.20.

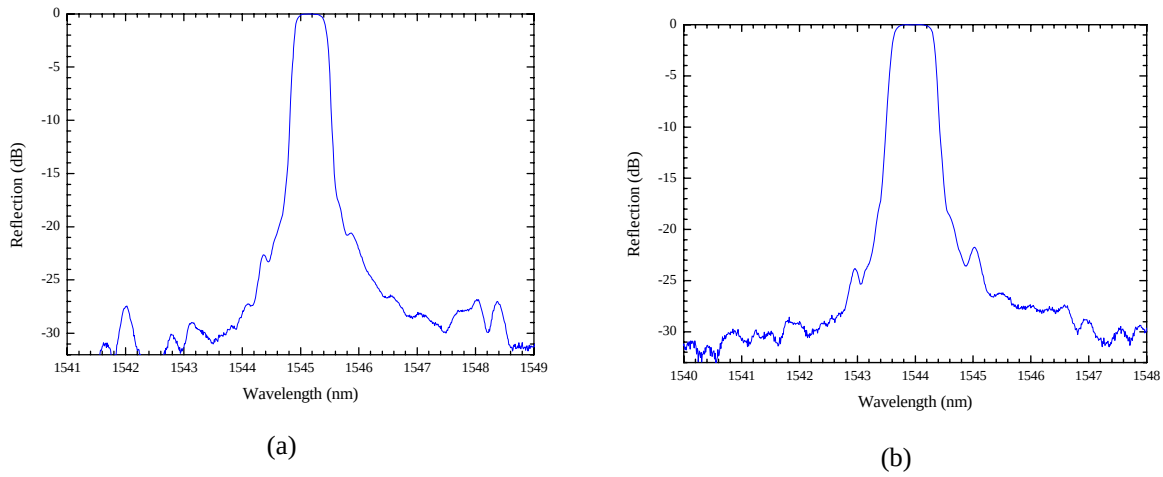

Figure 4.20 – High reflectivity apodized fiber Bragg gratings using the spatial profile of Figure 4.19.

Both fiber Bragg gratings shown in Figure 4.20 have a total length of 7 mm and were written with a scanning beam velocity of 30 μm/s, but with different incident optical powers. Therefore, grating (a) have a measured transmission filtering level of 25dB, while grating (b) has a value of 30 dB. The reflection spectra show that the first side lobes appear at levels above 20 dB and a noise floor situated at around 30 dB for both gratings. The first grating presents a flat-hat top of 0.3 nm, while the second 0.4 nm, both inside a 0.1 dB power variation from the peak maximum.

4.5 Chirped fiber Bragg gratings

In this case, the phase mask is slowly moved (unidirectionally) while the writing beam is scanned, allowing the production of variable wavelength/phase shifted gratings. This process enables a gradual phase shift to be added to the grating while being written. For uniform motion, this results in a simple shift of the Bragg wavelength, as described by equation (3.5).

To demonstrate this technique experimentally, five different Bragg gratings were written in hydrogen loaded standard Single Mode Fiber (ITU-T G.652) with a total length of 10 mm each, and using a beam diameter of 350 μm. The scanning beam velocity was 10 μm/s for all gratings, while the phase mask velocity was different for each grating, but kept constant. Figure 4.21 shows the obtained results.

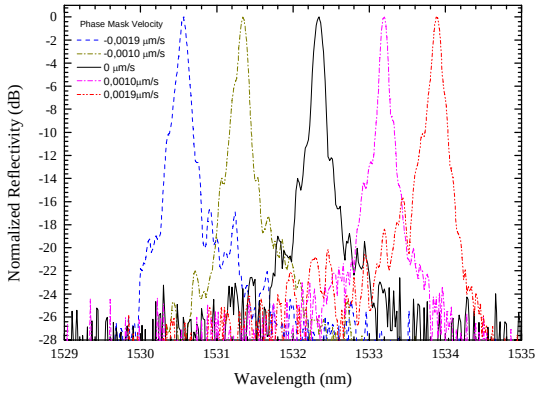

Figure 4.21 – Wavelength shift by the moving phase mask/ scanning beam technique.

While the photoinscription was performed, each grating was written with a given constant phase mask velocity, indicated in the figure, producing in this way the wavelength shift described above. Shifts to the right of the normal Bragg wavelength (static phase mask) represent movement of the phase mask and beam scanning in the same direction, whereas shifts to shorter wavelengths represent movement of the phase mask and beam scanning in opposite directions. For each side, a wavelength shift of around 2 nm is achieved, limited by the PZT maximum displacement, resulting in a total wavelength tunability of 4 nm.

Another important aspect that it is not shown in Figure 4.21, since the graph is normalized, is that for larger wavelength shifts, the grating strength decreases, since the refractive index modulation decreases when the phase mask velocity increases. The grating reflectivity has the dependence already described by equation (3.6).

It is now expectable that by increasing the phase mask velocity linearly (constant acceleration) during the UV writing results in a chirped grating. The results are shown in Figure 4.22.

From Figure 4.22 one can confirm that, at least spectrally, the gratings produced are chirped. Also, Figures 4.22–a) and b) show the grating spectral evolution during the photoinscription. In the first case the phase mask and the scanning beam are moving in opposite directions (negative chirp), while in the second their movement is in the same direction (positive chirp). Figure 4.22 – c) is a combination of a negative chirp and a positive chirp, obtained by double exposure of the fiber, maintaining all the writing parameters from one exposure to the other, except that the phase mask direction was reversed. Obviously, it is expectable that the second exposure, if not compensated by higher fluence, results in a lower reflectivity since the photosensitivity of the fiber is already reduced by the first illumination process. Also clear from the figure is that the grating strength decreases for larger wavelength shifts, as expected.

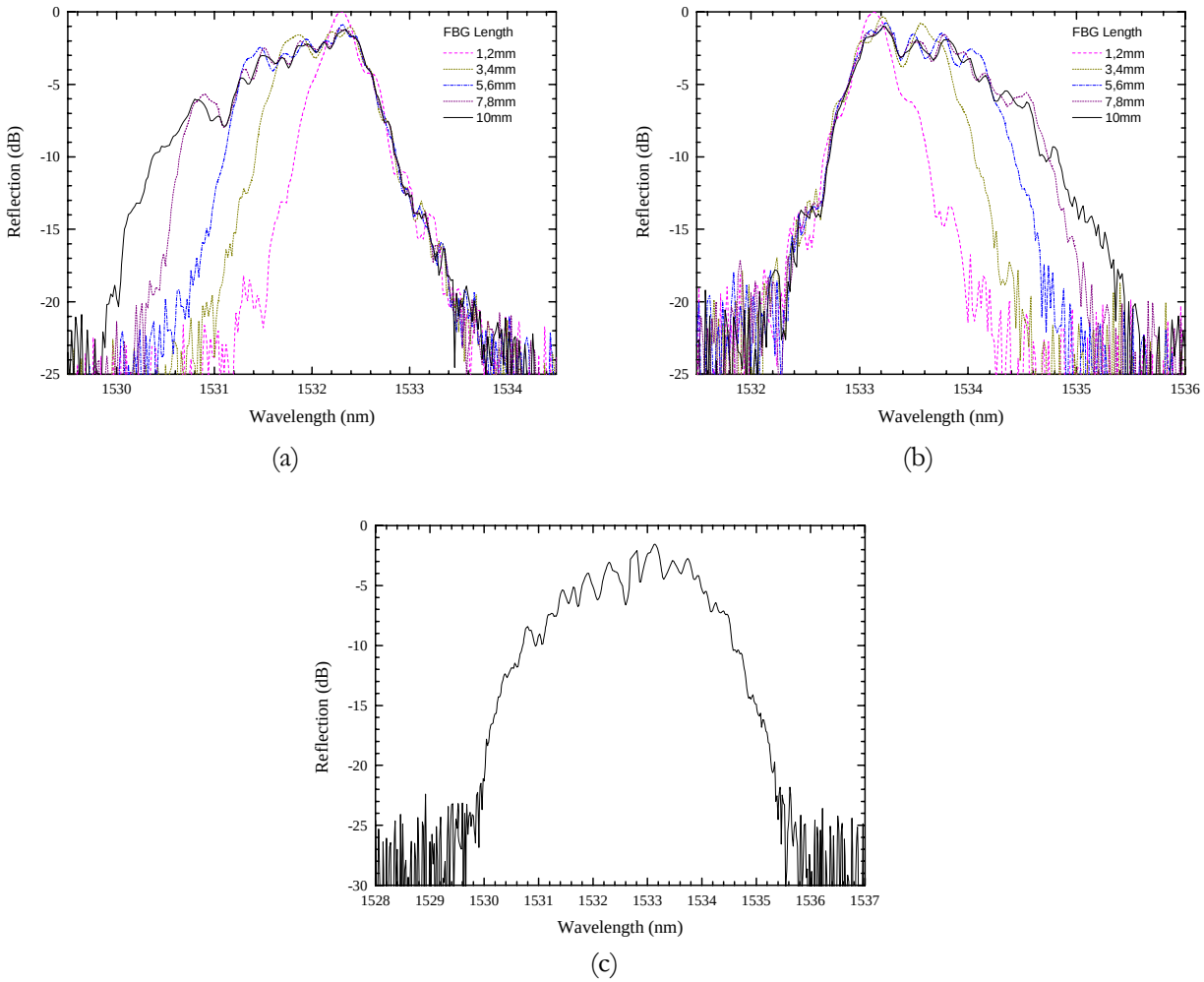

Figure 4.22 – Spectra of chirped fiber Bragg gratings fabricated by simultaneous phase mask movement and beam scanning. The spectra were obtained when the phase mask and beam move (a) in opposite directions (*negative chirp*), (b) in the same direction (*positive chirp*), and (c) in both (double exposure).

However, one of the most important properties of this type of gratings is its temporal response. The characterization setup of Figure 4.2 was assembled and the delay of a positive chirped fiber Bragg grating measured (see Figure 4.23).

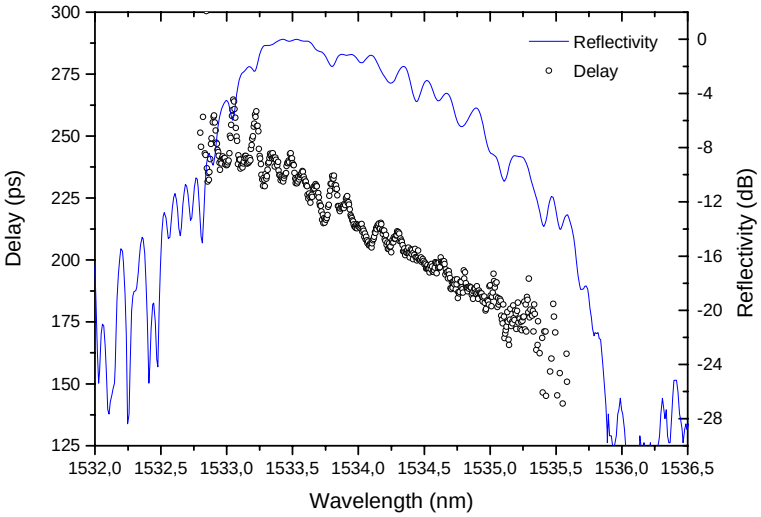

Figure 4.23 – Measured reflection spectra and group delay of a positive chirped fiber Bragg grating.

The total dispersion value for this chirped fiber Bragg grating (CFBG) is ~-38.2 ps/nm (as described by equation (2.52)). Important to note is that the sign of the dispersion value depends on the launched light direction into the CFBG. It will be positive when shorter wavelengths are reflected first and negative otherwise.

4.6 Phase shifted fiber Bragg gratings

The inscription of precise complex gratings, such as phase shifted structures, usually involves the translation of an interferogram by the desired phase shift. In this case, the shift of the interference pattern is achieved by translating the phase mask, being the precision with which the phase shift is made determined by the precision of the induced spatial shift along the waveguide, i.e., translation across the interferogram. As already seen in section 2.5.3, discrete phase shifts are normally used to create extremely narrow transmission resonances in a grating. The most well known application of discrete phase shifts is the use of a "quarter-wave" or π-shift in the center of a distributed-feedback laser. Figure 4.24 shows a π-shift fiber Bragg grating fabricated by displacing the phase mask at the middle of the grating, and its reflection spectra simulated by the transfer matrix method.

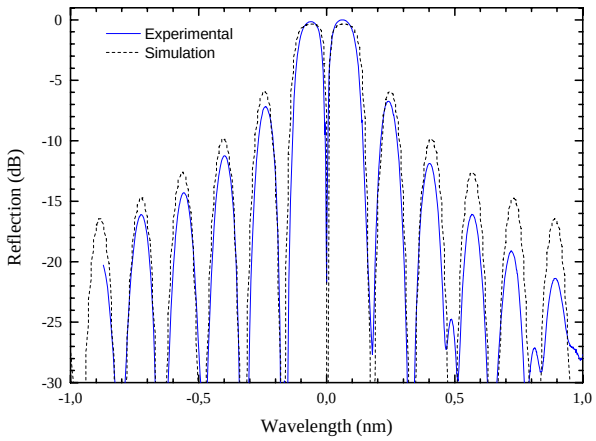

Figure 4.24 – Experimental and simulation of a π-shift fiber Bragg grating.

The 10 mm long grating was fabricated in hydrogen loaded standard Single Mode Fiber (ITU-T G.652), using a phase mask with a period of 1058.5 nm, and characterized with a resolution of 1 pm, using a tunable laser source to probe the grating and reading the reflected power on a power meter (see Figure 4.1-b). The experimental spectrum was fitted with a calculated profile from numerical simulation, with the following parameters: grating length of 10 mm, refractive index change of 1.7×10^{-4} and a spatial shift of 264.625 nm, corresponding to 1/4 of the phase mask pitch.

In order to achieve fine control and also check calibrations, the PZT shift driven voltage was changed by its maximum allowable resolution (1 mV). Three π-shift fiber Bragg gratings were then written with a difference of 1 mV in the applied voltage, corresponding to a spatial shift difference of 15 nm. Figure 4.25 shows the results obtained.

All fiber Bragg gratings shown have a total length of 10 mm, were written with a scanning beam velocity of 30 μm/s and were fabricated in hydrogen loaded standard Single Mode Fiber (ITU-T G.652). The center resonant wavelength is not totally resolved since the characterization was carried out using a broadband source and an OSA (Figure 4.1-a) with maximum resolution of 0.05nm. Figure 4.25 shows that a good control of the position of resonance (or phase shift value) can be achieved.

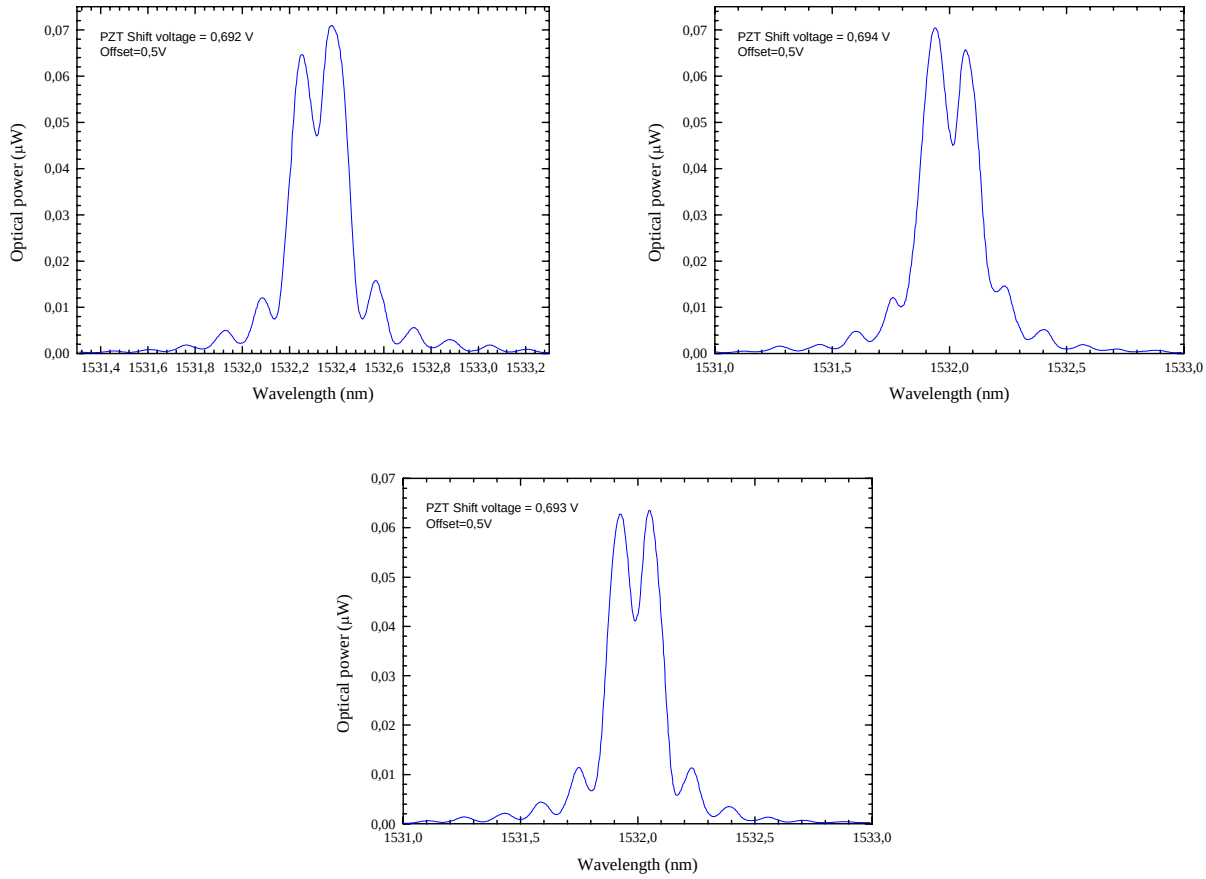

Figure 4.25 – Fine control of π-shift fiber Bragg gratings by changing PZT driven voltage by 1 mV, corresponding to a spatial shift difference of 15 nm.

To test reproducibility and accuracy of the writing setup, three fiber Bragg gratings with a spatial shift of $\Lambda_{PM}/8$, $\Lambda_{PM}/4$ and $3\Lambda_{PM}/8$, corresponding to expected phase shifts of $\pi/2$, π and $3\pi/2$, respectively (by using equation (2.74) and making the substitution obtained in equation (3.4)) were written. Figure 4.26 shows the results obtained.

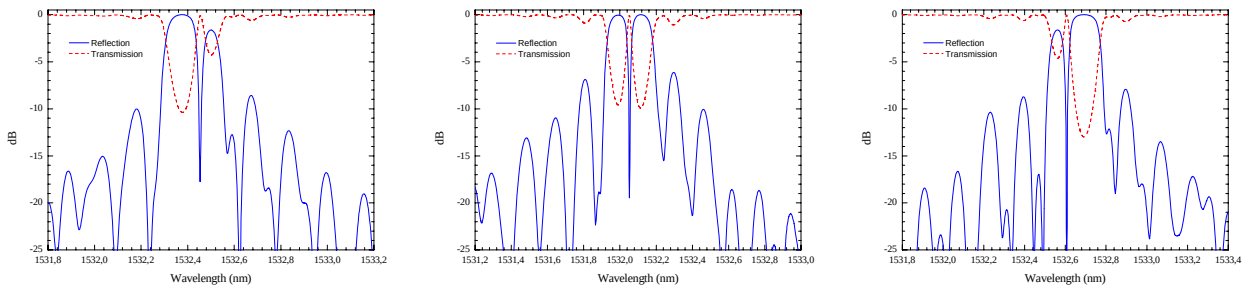

(a) (b) (c)

Figure 4.26 – Transmission and reflection spectrums of 10 mm long fabricated fiber Bragg gratings with a (a) $\pi/2$, a (b) π and a (c) $3\pi/2$ phase shift.

Also a measurement of the dispersion of the π-shift FBG was performed. The result is shown in Figure 4.27.

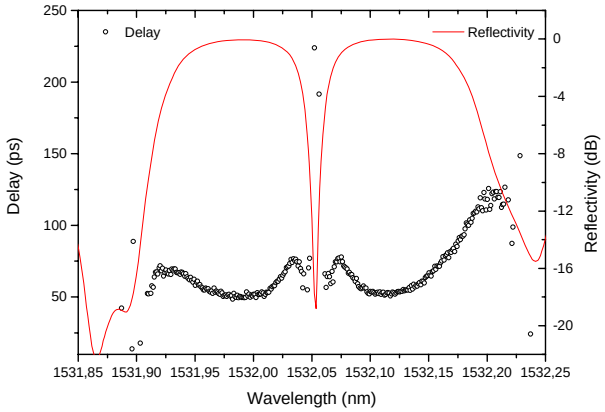

Figure 4.27 – Measured reflection spectra and group delay of a π-shift fiber Bragg grating.

The delay in the narrow band is difficult to measure since for this low reflectivity level, the signal reaching the oscilloscope is already under the sensitivity of the device. Nevertheless, the dispersion measurement presents two similar responses, one for each of the two originated Bragg gratings out of phase.

4.7 Sampled fiber Bragg gratings

More complex structures can be implemented by a periodic modulation of the refractive index amplitude and/or phase in the waveguide (sampled Bragg gratings). The resultant reflection spectrum and channel separation is a function of the shape and period of this modulation. As already described in section 2.5.4, the sampled grating is a conventional grating at the appropriate wavelength multiplied by a sampling function. Therefore, the spatial frequency content of these superstructures can be approximated by a comb of delta functions centered at the Bragg frequency. The separation between consecutive peaks is given by (2.76). Taking this into account, several experiments were performed. First by amplitude modulation, and then by phase modulation, allowing dense channel spacing without increasing the total grating length, as described by (2.77).

Amplitude modulation was performed by two ways: by changing the acousto-optic cell diffraction efficiency and by changing the phase mask dithering amplitude. Figure 4.28 shows results

of two sampled Bragg gratings written by changing the cell efficiency from 0 to 85 % with two different sampling periods.

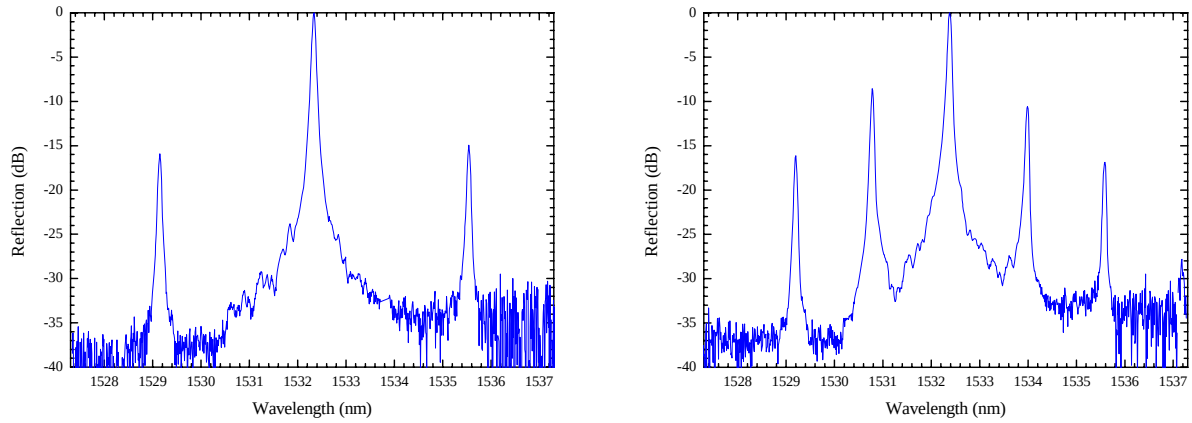

(a) (b)

Figure 4.28 – Sampled fiber Bragg gratings fabricated by amplitude modulation through acousto optic cell efficiency variation (0, 85 %, 0, 85 %, …) with a sampling period of (a) 250 μm and (b) 500 μm.

Both 30 mm long Bragg gratings shown were written in a hydrogen loaded standard Single Mode Fiber (ITU-T G.652) using a scanning beam velocity of 30 μm/s. A sampling period of 250 μm and 500 μm should result on a peak separation of 3.24 nm and 1.62 nm, respectively, as predicted by using equation (2.76). From Figure 4.28-a) a peak separation of 3.19 nm is measured, while from Figure 4.28-b) a value of 1.60 nm is obtained. This shows good agreement with predicted values, and confirms that by doubling the sampling period one can easily halve the peak spacing.

Another way of modulating the refractive index amplitude is by phase mask dithering, by changing visibility from 0 to 1 with a well defined sampling period. Figure 4.29 shows an example of a sampled Bragg grating written by this method. By using this technique, only the visibility is changed, maintaining the average refractive index constant.

The 30 mm long fiber Bragg grating was also written in hydrogen loaded standard Single Mode Fiber (ITU-T G.652) with a scanning beam velocity of 30 μm/s and a period of 500 μm, resulting in a measured peak separation of 1.60 nm.

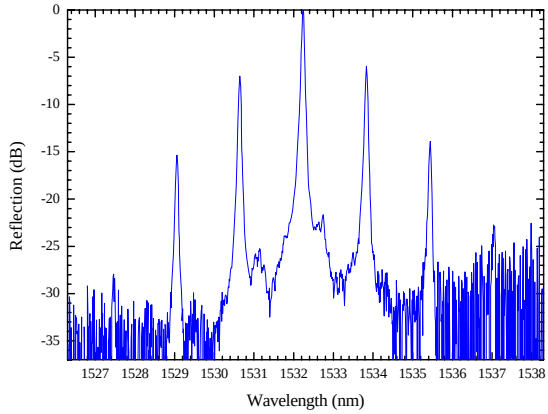

Figure 4.29 – Sampled fiber Bragg grating fabricated by amplitude modulation through phase mask dithering variation (visibility: 0, 1, 0, 1, …) with a sampling period of 500 μm.

However, the most interesting approach is grating sampling by using multiple phase shifts. Using this approach, peak equalization was also sought. Figure 4.30 illustrates the results obtained with several discrete π phase shifts.

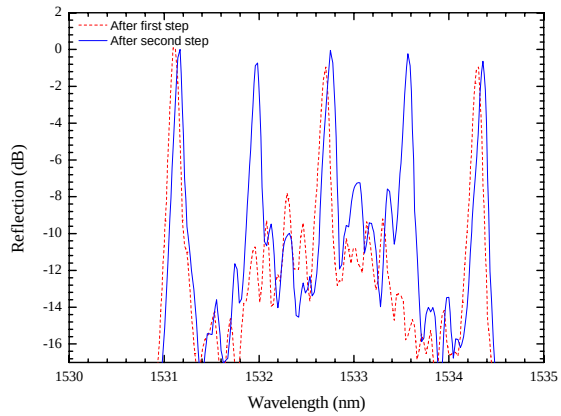

Figure 4.30 –Experimental results from sampled fiber Bragg gratings fabricated by phase modulation (0, π, 0, π, …) with a double exposure and different sampling periods.

The final sampled fiber Bragg grating spectrum shown in Figure 4.30 (solid line) was achieved by a double exposure process. In the first (dashed line), a UV beam power of ~80 mW was scanned at 20 μm/s and a sampling period of 500 μm was employed, resulting in a peak separation of 1.6 nm (confirmed by equation (2.76)). In the second exposure, a UV beam power of ~60 mW was scanned at 30 μm/s and a sampling period of 1000 μm was employed, resulting in a peak separation of 0.8 nm (confirmed by equation (2.76)). In this way, new peaks appear in the middle of the ones created by the first exposure grating since the sampling period doubled. By a suitable adjustment of

exposure powers and scanning velocity, equalization is achieved, being the five peaks within 1.5 dB peak power variation. The total grating length is 30 mm and was fabricated in hydrogen loaded standard Single Mode Fiber (ITU-T G.652).

4.8 Bragg gratings on planar devices

The rapidly growing optical communication market requires photonic components with ever-increasing functionality and complexity that can be fabricated reliably at low cost. Of the various approaches used to fabricate photonic components, those based on planar waveguides have achieved high performance and represent a promising path toward compact integration of optical functions. Now taking advantage of the possibility of writing Bragg gratings by UV exposure on such structures, one can fabricate devices with great interest. As an example, combined with planar silica technology [187], Bragg gratings allow for realizing optical add-drop multiplexers for DWDM [188]. As in fibers, the waveguides photosensitivity must be enhanced to make the fabrication of the grating-based optical devices easier. Enhancement photosensitivity techniques were already described in section 2.6. One example is use of co-dopants like Germanium that can be added to the silica core. However, the concentration of germanium cannot be made too high as germanium doping increases the numerical aperture of the waveguide, raising the problem of the efficient coupling of the guide to standard telecommunication optical fibers. Thus, to reduce this difficulty, it looks necessary to use a moderate concentration of germanium for doping the core of the waveguide and to further sensitize the waveguide through methods such as hydrogen or deuterium loading at a high pressure (> 100 bars) and room temperature (≤ 40°C) [164, 189] or UV-hypersensitization [190]. These two processes have proved already to be efficient ways for writing strong gratings in pure silica.

This section shows how the experimental writing system was adapted to allow the inscription of Bragg gratings in planar waveguides and presents results of Bragg gratings written such structures.

4.8.1 Experimental setup conversion and waveguide alignments

The experimental setup described in Figure 3.4 and showed in Figure 3.5 can be converted to write the type of gratings described in the previous sections in planar waveguides. For this purpose, the system was fitted with a CCD camera for device alignment and a vacuum holder for planar devices (see Figure 4.31).

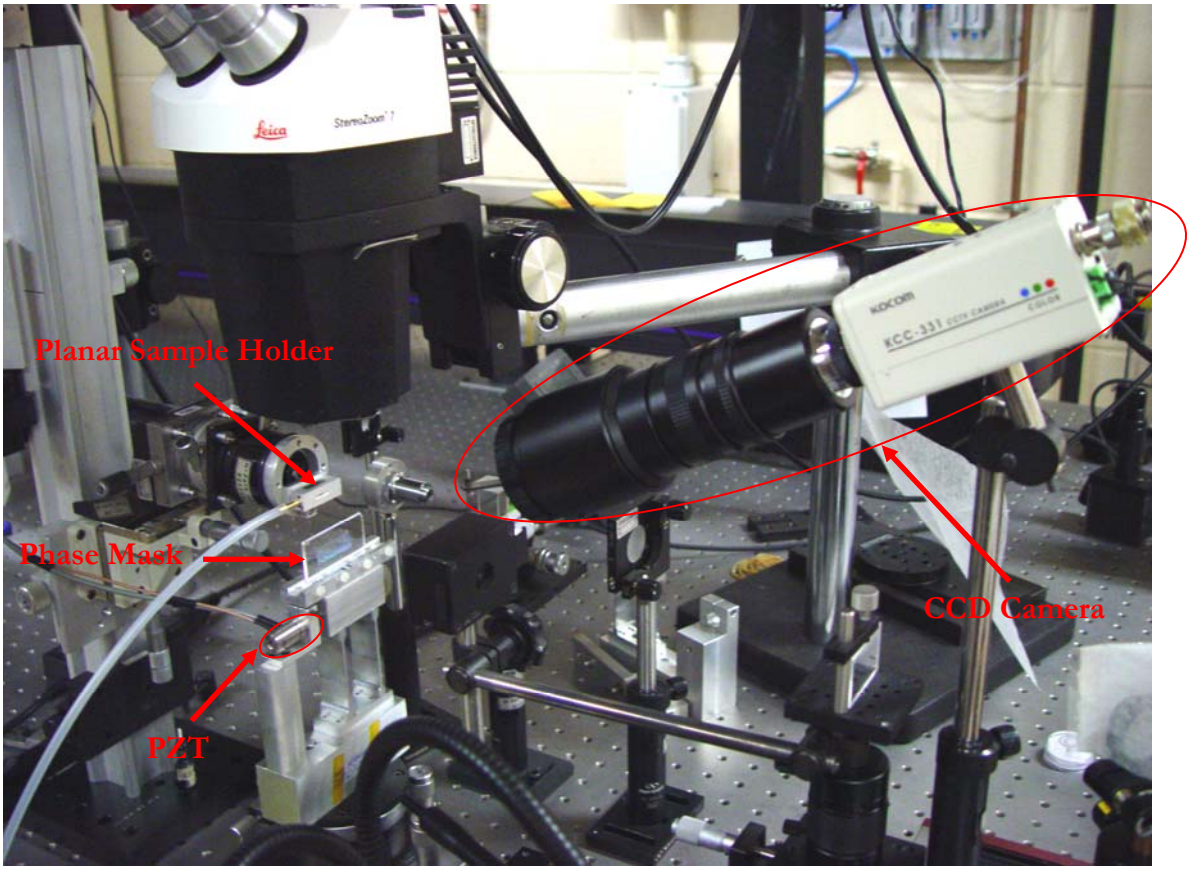

Figure 4.31 – Photograph of the experimental setup for planar waveguide gratings photoinscription.

The first difficulty encountered was related to sample alignment with the phase mask, visualization of the waveguides and the relative alignment between the UV writing beam and the waveguides. In order to achieve good parallelism between the sample and the phase mask, the final choice was to employ a special holder with an internal spherical mechanism that allows an infinity of degrees of freedom. The parallelism is achieved when the sample is pressed against the phase mask. The orientation of the sample is changed under pressure and the two surfaces become parallel (in fact, during this procedure the phase mask is removed and is replaced by flat piece of glass to prevent phase mask damage). At this point, the waveguide alignment is done by X-Y translation and rotation in a plane perpendicular to the incoming UV beam. A CCD camera was initially fitted around the system, but the last option was to mount it directly on the translation stage, and therefore the operator can check the relative position of the beam spot/waveguide at all times. There is white light illumination for waveguide inspection.

A picture of the waveguides as seen by the CCD camera (for alignment with the laser beam) is shown in Figure 4.32. Also displayed is the waveguide fluorescence while the UV beam is incident on it.

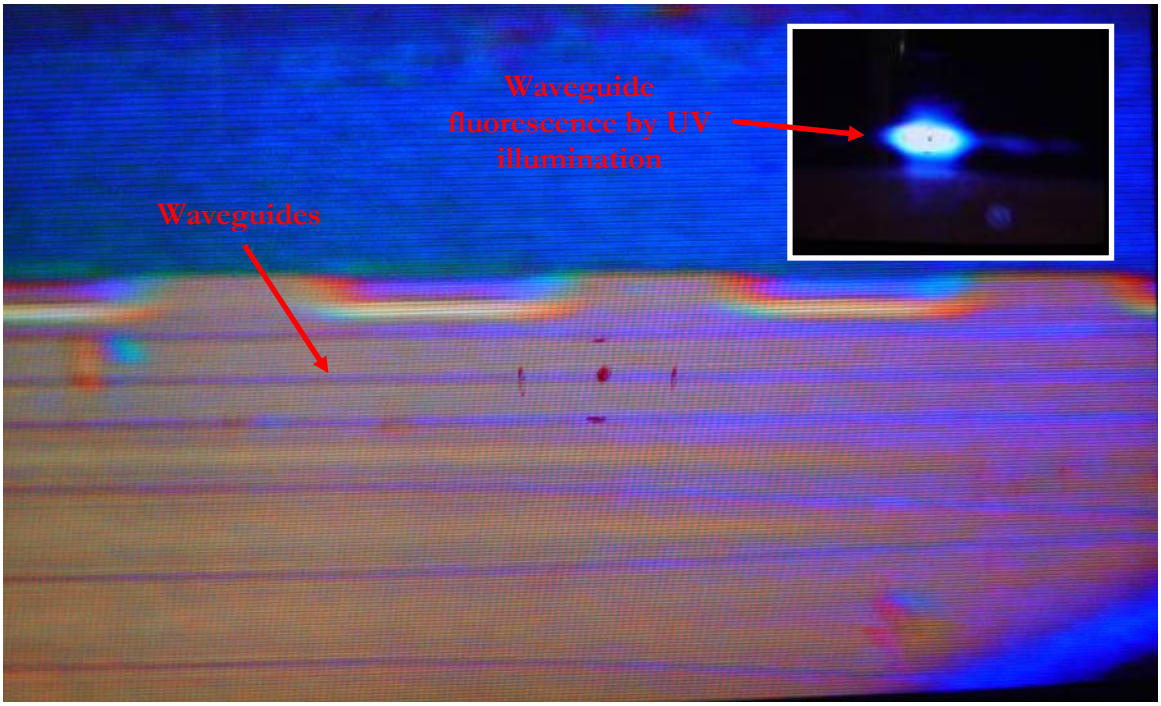

Figure 4.32 – CCD camera view of planar waveguide structures and waveguide fluorescence with UV laser beam incidence.

4.8.2 Apodized Bragg gratings in straight waveguides and MZIs

The buried planar single-mode waveguides used in this work have been manufactured at Alcatel SEL (Stuttgart, Germany) and IPHT - Institute for Physical High Technology (Jena, Germany) by the FHD technique [191]. The core was co-doped with Germanium (11.4% wt) and phosphorous (6.5% wt). The samples were hydrogen loaded at ~120 atm at room temperature for more than one week.

Bragg gratings with the spatial profile of Figure 4.19 were then written in 4 μm wide straight waveguides. The 7 mm long fiber Bragg gratings were written with a beam scanning velocity of 10 μm/s, and with a UV power incident in the phase mask (with a period of 1058.5 nm) of 100 mW (Figure 4.33-a) and 90 mW (Figure 4.33-b). The first issue to be addressed was the photosensitivity of the planar samples. As it can be seen in Figure 4.33, waveguide photosensitivity is not a problem in this hydrogen loaded samples, since filtering levels of more than 40 dB were easily achieved.

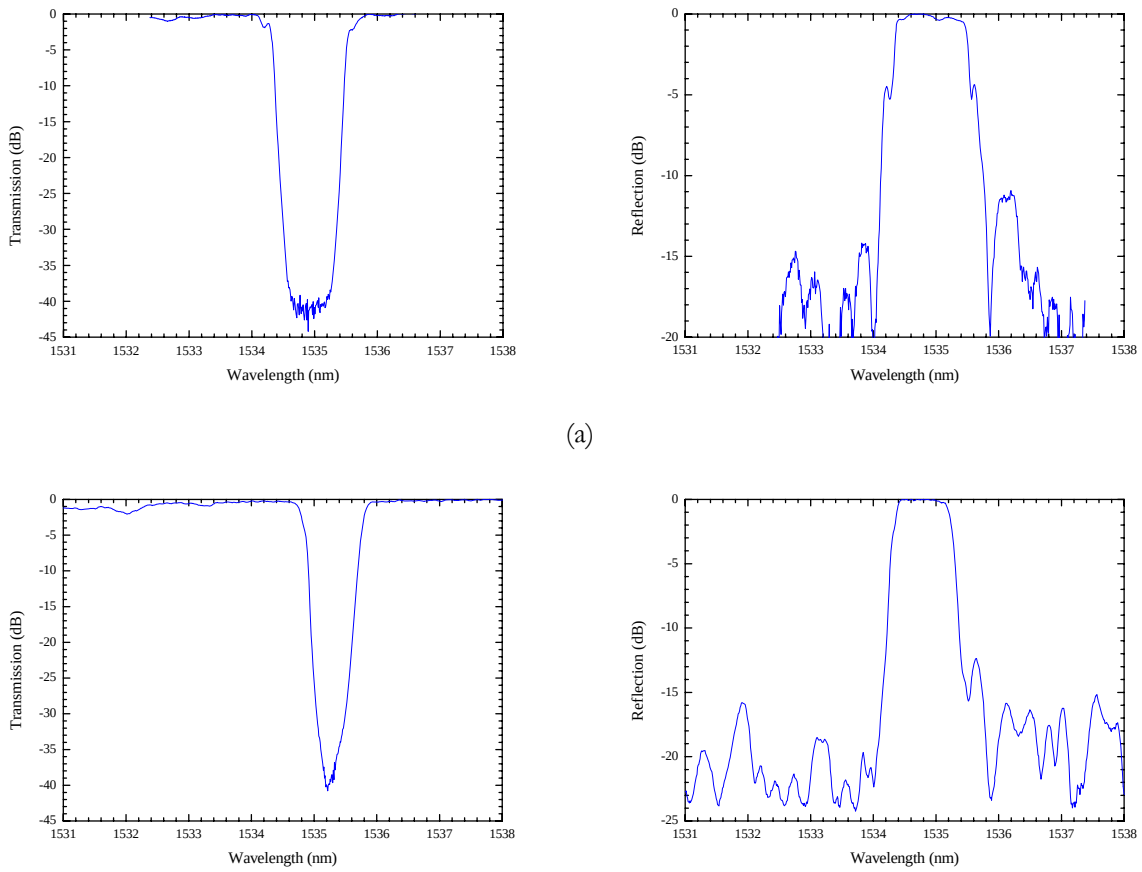

Figure 4.33 – Spectral transmission and reflectivity of apodized Bragg gratings written in straight waveguides with scanning velocities of 10 mm/s and different UV laser powers.

It was immediately noticed that it is harder to produce good quality Bragg gratings in waveguides than it is on fibers. In many cases, the level of the sidelobes is much higher than expected and it was also noticed the appearance of distinct sidelobes on each side of the main peak. One possible reason for the appearance of these sidelobes is a low frequency modulation of the interference pattern. Many alignment tests were performed and many gratings written but the results were inconclusive. Although the quality is not similar to the one obtained in fibers, Bragg gratings were successfully written in planar waveguides, which by itself is a very good achievement.

Following the first tests related to the process of writing apodized Bragg gratings on straight channel waveguides, the next step was to realize an add-drop filter based on a Mach-Zhender Interferometer (MZI) as shown in Figure 4.34.

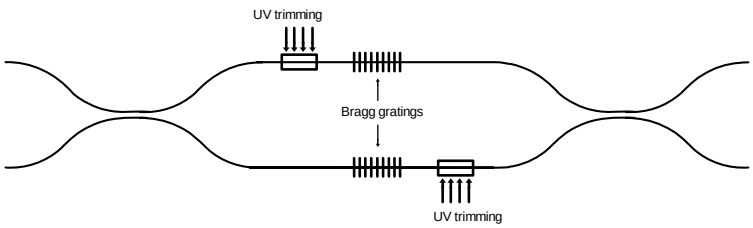

Figure 4.34 – Add-drop filter implementation based on a Mach-Zhender interferometer.

The challenge was to write equal gratings in both arms of a Mach-Zhender interferometer. Following that, the two path lengths have to be adjusted by UV trimming (to correct phase errors that arise from nonsymmetrical positioning of the two Bragg gratings on the interferometer arms) with real time monitoring (this operation was performed by Dr. Martin Becker at IPHT, Jena, Germany).

Figure 4.35 shows the reflected and the output signals from an integrated Mach-Zhender Interferometer, in hydrogen loaded Alcatel VO105/4 Single Stage OADM samples, when two equal apodized Bragg gratings were written on the interferometer arms. This result was obtained before any UV trimming procedure was implemented.

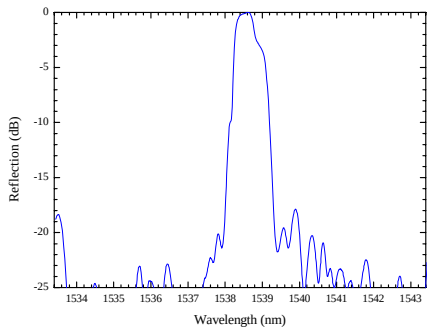

(a)

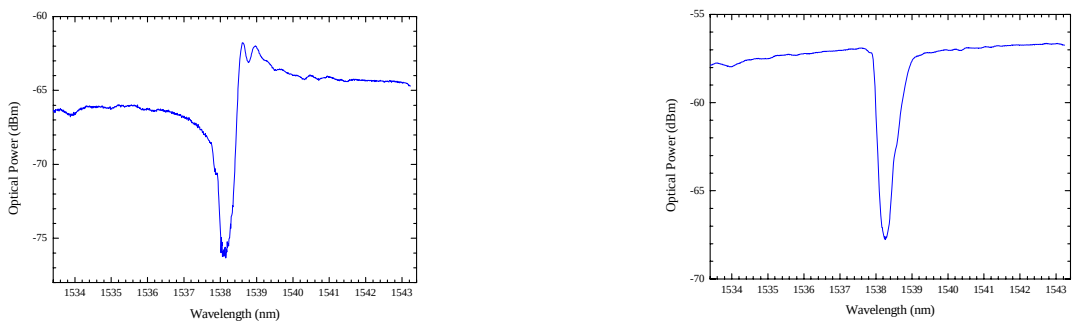

(b)

Figure 4.35 – Reflected and transmitted signals from an integrated MZI when two equal apodized Bragg gratings were written on the interferometer arms, before UV trimming.

The reason for the lower quality of the gratings written in planar waveguides was extensively searched. One possible reason was the formation of a resonant cavity formed between the pure silicon and the outer surface of the top cladding. This is a situation which is intrinsic to the planar structures, and therefore other possibilities were investigated. The first one was the possibility of this cavity being formed between the sample surface and the phase mask. To check this, the phase mask was replaced with a flat glass slide and the usually alignment routine was performed in order to achieve parallelism between both surfaces. Then the set was illuminated with a hydrogen lamp, and a modulation pattern was clearly seen through the CCD camera (Figure 4.36). In fact the two arms of the Mach-Zhender interferometer are clearly seen in the middle of the picture. The periodicity of the fringes changed when the alignment conditions were modified. It was obvious that this effect can be a potential problem, since this pattern could not be eliminated. Even if the pattern is completely aligned with the waveguides, the UV dose changes depending if the waveguide is located in a point of high or low visibility.

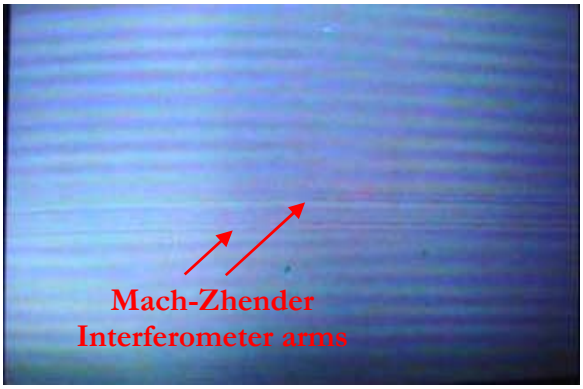

Figure 4.36 – CCD camera view of a planar sample and a flat glass slide in parallelism when illuminated with a hydrogen lamp.

4.9 Conclusion

Fabrication of complex Bragg gratings using the implement phase mask dithering/moving techniques was demonstrated in this chapter. Initially, the phase mask dithering amplitude was experimentally calibrated, and the study of several controlled parameters, like the scanning beam velocity, the UV incident power and the grating length was performed. The fabricated and characterized fiber Bragg gratings include the comparison of different apodization profiles, the inscription of several phase shifted gratings, the achievement of chirp behavior and finally, the

writing of sampled Bragg gratings by amplitude and phase modulation. Also high performance apodized Bragg gratings with modeled spatial profiles were achieved.

Another extremely relevant aspect of this chapter was the conversion of the setup to afford the inscription in planar structures. Apodized high reflective gratings in planar waveguides and in the arms of Mach-Zhender interferometers were demonstrated.

5 Conclusions

5.1 Final considerations and evaluation of the developed work

The advantages of Bragg gratings were already presented and examples given, and so is not worth to be mentioned again here. What is important to note is that their performance is intrinsically connected to their fabrication. Most of the methods currently available are based on the phase mask technique and allow the fabrication of good quality and reproducible Bragg gratings but the method consent very low flexibility. This means that if other types of gratings are required, the use of a phase mask with the desired profile is also necessary, increasing the cost/effectiveness of the method. Thus, the method chosen in this work makes use of the effectiveness of the phase mask method, introducing other control elements to allow the tailoring of Bragg grating structures. The phase mask dithering/moving technique allows, in this way, the combination of simplicity and high reproducibility with the desired flexibility. Some of the essential aspects related to the experimental implementation of this method are presented in this work. Basically, the local grating visibility or contrast and phase are controlled by dithering/displacement of the phase mask, without affecting the average refractive index. High dithering amplitudes destroy the interference pattern created by the phase mask at the fiber plane by fringe blurring. Thus, dithering is an ideal mechanism for varying the local strength of the grating without changing its local Bragg wavelength, since it keeps the average refractive index constant. Associated with the fact that tailored Bragg gratings can be achieved by using a standard uniform phase mask makes this one of the most interesting and useful methods available.

Regarding the theoretical aspects of Bragg gratings, chapter 2 gave an overview of Bragg grating properties and introduced coupled-mode theory, which describes the relation between the spectral dependence of a grating and the corresponding grating structure. The idea is not to give the reader a detailed analysis of how the relations can be deduced from Maxwell's equations, but instead to focus on how each physical parameter can affect the grating response, as for example how the dependency of the grating reflectivity behaves with refractive index change or grating length, among others. This understanding is also useful to follow the results obtained for the different types of Bragg gratings modeled by the transfer matrix method. By defining its spatial profile, several types of gratings were simulated by implementing this method in Matlab®. Results of the spectral response of apodized (by using specific apodization functions, also described), phase shifted and chirped

(including the temporal behavior for this case) Bragg gratings were presented. The description and simulation of these complex structures provided a very useful understanding for when the fabrication technique was implemented.

The description of the system implemented using the phase mask dithering technique was described in chapter 3, including an analysis of the basic calibrations needed. Also important to note is that a LabView™ based program was fully developed in order to control the writing setup. This enables to have an almost fully automated system, with a user-friendly interface. Therefore, the operator only needs to place the waveguide and perform the basic alignments (at least once) and then just select the desired type of Bragg grating to be written. The choice includes uniform, apodized, chirped, phase shifted and sampled Bragg gratings. Also, any spatial profile can be introduced in the software, allowing in this way the execution of even more complex structures.

The demonstration of the setup capabilities were shown in chapter 4, starting by studying several controlled parameters (beam scanning velocity, UV incident power, grating length) and showing the adjustments and re-calibrations that were needed to obtain a good performance, and ends with the presentation of the fabricated complex structures. Different apodization profiles were compared, several phase shifted gratings were written, chirped behavior was achieved, as proved by its temporal response, and finally, sampled Bragg gratings by amplitude and phase modulation were shown. It should be noted that the objective was not to look for optimized fiber Bragg gratings, except when using the apodization spatial design#2 (Figure 4.19). From here, the intention was to meet some specifications for application in optical communication networks. The produced fiber Bragg gratings were inside the targeted values, proving to be useful to the application envisaged. Another particularity of the developed setup is that it can be easily adapted to write Bragg grating in planar structures. This increases the potential of this system enormously. High reflective gratings in planar waveguides and Mach-Zhender interferometers were presented. Although the results for this waveguides were not as good as for fibers, high reflectivities were achieved, which is only possible in this cases the alignment is properly made and controlled, and apodization was demonstrated.

As demonstrated by the results presented in this thesis, the goal of this work was completely satisfied. The requirement of optimization is probably needed in some cases as it is in any other system when the demanding for a specific targeted grating exists. However, the basic infrastructure already exists and proved to be efficient.

5.2 Suggestions for future work

In terms of the fabrication system, suggestions should go in the way of improving the overall system performance and making it as reproducible as possible. The need for user intervention should be reduced, by building, for example, a system for automated vision alignment of the fiber and planar samples and distance to the phase mask. To broaden the system capacity, the phase mask or waveguide holders can be placed on a high resolution translation stage which would allow the inscription of longer gratings, overcoming the phase mask length limitation.

In terms of grating fabrication, the sampled grating with phase shifts and the phase shifted gratings can have a great potential in some applications, like fiber lasers. Studies of these structures can be made in detail by varying the location and amplitude of the shifts. Also, more studies should be carried in planar waveguides, not only to increase its performance but also to take advantage of all the complex gratings described in this technology. Also a setup that would allow real time monitorization of the grating growing over time in planar waveguides would be very useful and should be implemented.

Bibliography

1. Hill, K.O., et al., *Photosensitivity in Optical Fiber Waveguides - Application to Reflection Filter Fabrication.* Applied Physics Letters, 1978. **32**(10): p. 647-649.
2. Kawasaki, B.S., et al., *Narrow-Band Bragg Reflectors in Optical Fibers.* Optics Letters, 1978. **3**(2): p. 66-68.
3. Lam, D.K.W. and B.K. Garside, *Characterization of Single-Mode Optical Fiber Filters.* Applied Optics, 1981. **20**(3): p. 440-445.
4. Meltz, G., W.W. Morey, and W.H. Glenn, *Formation of Bragg Gratings in Optical Fibers by a Transverse Holographic Method.* Optics Letters, 1989. **14**(15): p. 823-825.
5. Hosono, H., et al., *Nature and origin of the 5-eV Band in SiO_2:GeO_2 Glasses.* Physics Review B, 1995. **46**: p. II-445-II-451.
6. Hill, K.O., et al., *Bragg Gratings Fabricated in Monomode Photosensitive Optical Fiber by Uv Exposure through a Phase Mask.* Applied Physics Letters, 1993. **62**(10): p. 1035-1037.
7. Lemaire, P.J., et al., *High-Pressure H_2 Loading as a Technique for Achieving Ultrahigh UV Photosensitivity and Thermal Sensitivity in GeO_2 Doped Optical Fibers.* Electronics Letters, 1993. **29**(13): p. 1191-1193.
8. Canning, J. and M.G. Sceats, *Pi-Phase-Shifted Periodic Distributed Structures in Optical Fibers by UV Post-Processing.* Electronics Letters, 1994. **30**(16): p. 1344-1345.
9. Erdogan, T. and J.E. Sipe, *Radiation-Mode Coupling Loss in Tilted Fiber Phase Gratings.* Optics Letters, 1995. **20**(18): p. 1838-1840.
10. Byron, K.C., et al., *Fabrication of Chirped Bragg Gratings in Photosensitive Fiber.* Electronics Letters, 1993. **29**(18): p. 1659-1660.
11. Vengsarkar, A.M., et al., *Long-period fiber gratings as band-rejection filters.* Journal of Lightwave Technology, 1996. **14**(1): p. 58-65.
12. Patrick, H.J., et al., *Amplitude mask patterned on an excimer laser mirror for high intensity writing of long period fibre gratings.* Electronics Letters, 1997. **33**(13): p. 1167-1168.
13. Philips, H.M., et al., *Sub-100 nm lines produced by direct laser ablation in polyimide.* Applied Physics Letters, 1991. **58**(24): p. 2761-2763.
14. Dyer, P.E., R.J. Farley, and R. Giedl, *Analysis and application of a 0/1 order Talbot interferometer for 193 nm laser grating formation.* Optics Communications, 1996. **129**(1-2): p. 98-108.
15. Kashyap, R., et al., *Novel Method of Producing All-Fiber Photoinduced Chirped Gratings.* Electronics Letters, 1994. **30**(12): p. 996-998.
16. Kashyap, R., *Assessment of tuning the wavelength of chirped and unchirped fibre Bragg grating with single phase-masks.* Electronics Letters, 1998. **34**(21): p. 2025-2027.
17. Hill, K.O., et al., *Efficient Mode Conversion in Telecommunication Fiber Using Externally Written Gratings.* Electronics Letters, 1990. **26**(16): p. 1270-1272.
18. Malo, B., et al., *Point-by-Point Fabrication of Micro-Bragg Gratings in Photosensitive Fiber Using Single Excimer Pulse Refractive-Index Modification Techniques.* Electronics Letters, 1993. **29**(18): p. 1668-1669.
19. Anderson, D.Z., et al., *Production of in-Fiber Gratings Using a Diffractive Optical-Element.* Electronics Letters, 1993. **29**(6): p. 566-568.
20. Martin, J. and F. Ouellette, *Novel writing technique of long and highly reflective in-fibre gratings.* Electronics Letters, 1994. **30**(10): p. 811-812.
21. Malo, B., et al., *Single-excimer-pulse writing of fiber gratings by use of a zero-order nulled phase mask: grating spectral response and visualization of index perturbations.* Optics Letters, 1993. **18**(15): p. 1277.
22. Matsuhara, M. and K.O. Hill, *Optical-Waveguide Band-Rejection Filters - Design.* Applied Optics, 1974. **13**(12): p. 2886-2888.

23. Tanaka, K., et al., *Apodization for Gaussian-Beam Incidence - Numerical Examination.* Optics Communications, 1995. **115**(1-2): p. 29-34.
24. Malo, B., et al., *Apodised in-Fiber Bragg Grating Reflectors Photoimprinted Using a Phase Mask.* Electronics Letters, 1995. **31**(3): p. 223-225.
25. Albert, J., et al., *Apodization of the Spectral Response of Fiber Bragg Gratings Using a Phase Mask with Variable Diffraction Efficiency.* Electronics Letters, 1995. **31**(3): p. 222-223.
26. Cortes, P.Y., F. Ouellette, and S. LaRochelle, *Intrinsic apodisation of Bragg gratings written using UV-pulse interferometry.* Electronics Letters, 1998. **34**(4): p. 396-397.
27. Albert, J., et al., *Moire phase masks for automatic pure apodisation of fibre Bragg gratings.* Electronics Letters, 1996. **32**(24): p. 2260-2261.
28. Kashyap, R., A. Swanton, and D.J. Armes, *Simple technique for apodising chirped and unchirped fibre Bragg gratings.* Electronics Letters, 1996. **32**(13): p. 1226-1228.
29. Cole, M.J., et al., *Moving Fibre/Phase Mask-Scanning Beam Technique for Enhanced Flexibility in Producing Fiber Gratings with Uniform Phase Mask.* Electronics Letters, 1995. **31**(17): p. 1488-1490.
30. Loh, W.H., et al., *Complex Grating Structures with Uniform Phase Masks Based on the Moving Fiber-Scanning Beam Technique.* Optics Letters, 1995. **20**(20): p. 2051-2053.
31. Williams, J.A.R., et al., *Fiber Dispersion Compensation Using a Chirped in-Fiber Bragg Grating.* Electronics Letters, 1994. **30**(12): p. 985-987.
32. Hill, K.O., et al., *Chirped in-Fiber Bragg Gratings for Compensation of Optical-Fiber Dispersion.* Optics Letters, 1994. **19**(17): p. 1314-1316.
33. Durkin, M., et al., *1m long continuously-written fibre Bragg gratings for combined second- and third-order dispersion compensation.* Electronics Letters, 1997. **33**(22): p. 1891-1893.
34. Garthe, D., G. Milner, and Y. Cai, *System performance of broadband dispersion compensating gratings.* Electronics Letters, 1998. **34**(6): p. 582-583.
35. Hill, P.C. and B.J. Eggleton, *Strain Gradient Chirp of Fiber Bragg Gratings.* Electronics Letters, 1994. **30**(14): p. 1172-1174.
36. Lauzon, J., et al., *Implementation and characterization of fiber Bragg gratings linearly chirped by a temperature gradient.* Optics Letters, 1994. **19**(23): p. 2027-2029.
37. Dong, X.Y., et al., *Strain gradient chirp of uniform fiber Bragg grating without shift of central Bragg wavelength.* Optics Communications, 2002. **202**(1-3): p. 91-95.
38. Putnam, M.A., G.M. Williams, and E.J. Friebele, *Fabrication of tapered, strain-gradient chirped fibre Bragg gratings.* Electronics Letters, 1995. **31**(4): p. 309-310.
39. Zhang, Q., et al., *Linearly and nonlinearly chirped Bragg gratings fabricated on curved fibers.* Optics Letters, 1995. **20**(10): p. 1122-1124.
40. Painchaud, Y., A. Chandonnet, and J. Lauzon, *Chirped fibre gratings produced by tilting the fibre.* Electronics Letters, 1995. **31**(4): p. 171-172.
41. Dong, L., et al., *Fabrication of chirped fibre gratings using etched tapers.* Electronics Letters, 1995. **31**(11): p. 908-909.
42. Mora, J., et al., *Tunable chirp in Bragg gratings written in tapered core fibers.* Optics Communications, 2002. **210**(1-2): p. 51-55.
43. Frazao, O., et al., *Chirped Bragg grating fabricated in fused fibre taper for strain-temperature discrimination.* Measurement Science & Technology, 2005. **16**(4): p. 984-988.
44. Xu, M.G., et al., *Temperature-Independent Strain Sensor Using a Chirped Bragg Grating in a Tapered Optical-Fiber.* Electronics Letters, 1995. **31**(10): p. 823-825.
45. Kim, S., et al., *Temperature-independent strain sensor using a chirped grating partially embedded in a class tube.* IEEE Photonics Technology Letters, 2000. **12**(6): p. 678-680.
46. Kim, S., et al., *Fiber Bragg grating strain sensor demodulator using a chirped fiber grating.* IEEE Photonics Technology Letters, 2001. **13**(8): p. 839-841.
47. Alferness, R.C., et al., *Narrowband grating resonator filters in InGaAsP/InP waveguides.* Applied Physics Letters, 1986. **49**(3): p. 125-127.

48. Utaka, K., et al., *λ/4-shifted InGaAsP/InP DFB lasers.* IEEE Journal of Quantum Electronics, 1986. **22**(7): p. 1042-1051.
49. Uttamchandani, D. and A. Othonos, *Phase shifted Bragg gratings formed in optical fibres by post-fabrication thermal processing.* Optics Communications, 1996. **127**(4-6): p. 200-204.
50. Poladian, L., et al., *Characterisation of phase-shifts in gratings fabricated by over-dithering and simple displacement.* Optical Fiber Technology, 2003. **9**(4): p. 173-188.
51. Ashton, B.J., J. Canning, and N. Groothoff, *Two-Point Source Interferometric Grating Writing.* Applied Optics, 2004. **43**(15): p. 3140-3144.
52. Jensen, J.B., et al., *Polarization control method for ultraviolet writing of advanced Bragg gratings.* Optics Letters, 2002. **27**(12): p. 1004-1006.
53. Deyerl, H.-J., et al., *Fabrication of Advanced Bragg Gratings with Complex Apodization Profiles by Use of the Polarization Control Method.* Applied Optics, 2004. **43**(17): p. 3513-3522.
54. Canning, J., H.-J. Deyerl, and M. Kristensen, *Precision phase-shifting applied to fibre Bragg gratings.* Optics Communications, 2005. **244**(1-6): p. 187-191.
55. Eggleton, B.J., et al., *Long periodic superstructure Bragg gratings in optical fibres.* Electronics Letters, 1994. **30**(19): p. 1620-1622.
56. Ouellette, F., et al., *Broadband and WDM dispersion compensation using chirped sampled fibre Bragg gratings.* Electronics Letters, 1995. **31**(11): p. 899-901.
57. Ibsen, M., et al., *30 dB sampled gratings in germanosilicate planar waveguides.* Electronics Letters, 1996. **32**(24): p. 2233-2235.
58. Ibsen, M., et al., *Sinc-sampled fiber Bragg gratings for identical multiple wavelength operation.* IEEE Photonics Technology Letters, 1998. **10**(6): p. 842 - 844.
59. Nasu, Y. and S. Yamashita, *Multiple phase-shift superstructure fibre Bragg grating for DWDM systems.* Electronics Letters, 2001. **37**(24): p. 1471-1472.
60. Pliska, T., et al., *Wavelength stabilized 980 nm uncooled pump laser modules for erbium-doped fiber amplifiers.* Optics and Lasers in Engineering, 2005. **43**(3-5): p. 271-289.
61. Ventrudo, B.F., et al., *Wavelength and intensity stabilisation of 980 nm diode lasers coupled to fibre Bragg gratings.* Electronics Letters, 1994. **30**(25): p. 2147-2149.
62. Hamakawa, A., et al. *Wavelength stabilization of 1.48μm pump laser by fiber grating.* in *European Conference on Optical Communication, ECOC'96*. 1996. Oslo, Norway.
63. McGowan, R. and D. Crawford. *Dual Bragg grating frequency stabilization of a 980 nm diode laser.* in *Optical Fiber Communication Conference and Exhibit, OFC'02*. 2002.
64. Buryak, A.V., et al. *Recent progress and novel directions in multichannel FBG dispersion compensation.* in *Conference on Lasers and Electro-Optics, CLEO '03*. 2003.
65. Hill, K.O., et al., *Chirped in-fibre Bragg grating dispersion compensators: linearisation of dispersion characteristic and demonstration of dispersion compensation in 100 km, 10 Gbit/s optical fibre link.* Electronics Letters, 1994. **30**(21): p. 1755-1756.
66. Kashyap, R., et al., *30 ps chromatic dispersion compensation of 400 fs pulses at 100Gbits/s in optical fibres using an all fibre photoinduced chirpedreflection grating.* Electronics Letters, 1994. **30**(13): p. 1078-1080.
67. Pan, Z., et al., *Using sampled nonlinearly chirped fiber Bragg gratings to achieve 40-Gbit/s tunable multi-channel dispersion compensation.* Optics Communications, 2004. **241**(4-6): p. 371-375.
68. Pan, Z., et al. *40-Gb/s RZ 120-km transmission using a nonlinearly-chirped fiber Bragg grating (NL-FBG) for tunable dispersion compensation.* in *Optical Fiber Communication Conference and Exhibit, OFC'02*. 2002.
69. Hill, K.O., et al., *Variable-spectral-response optical waveguide Bragg grating filters for optical signal processing.* Optics Letters, 1995. **20**(12): p. 1438-1440.
70. Bilodeau, F., et al., *High-return-loss narrowband all-fiber bandpass Bragg transmission filter.* IEEE Photonics Technology Letters, 1994. **6**(1): p. 80-82.
71. Bilodeau, F., et al., *An all-fiber dense wavelength-division multiplexer/demultiplexer using photoimprinted Bragg gratings.* IEEE Photonics Technology Letters, 1995. **7**(4): p. 388 - 390.

72. Cullen, T.J., et al., *Compact all-fibre wavelength drop and insert filter.* 1994. **30**(25): p. 2160 - 2162.
73. Baumann, I., et al., *Compact all-fiber add-drop-multiplexer using fiber Bragg gratings.* IEEE Photonics Technology Letters, 1996. **8**(10): p. 1331 - 1333.
74. Dong, L., et al., *Novel add/drop filters for wavelength-division-multiplexing optical fiber systems using a Bragg grating assisted mismatched coupler.* IEEE Photonics Technology Letters, 1996. **8**(12): p. 1656 - 1658.
75. Xia, L., et al., *Custom design of large chirped fiber Bragg gratings on application of arbitrary profile filtering.* Optics Communications, 2003. **226**(1-6): p. 175-179.
76. Chen, Y., et al., *Mach–Zehnder fiber-grating-based fixed and reconfigurable multichannel optical add-drop multiplexers for DWDM networks.* Optics Communications, 1999. **169**(1-6): p. 245-262.
77. Romero, R., et al., *Chirped fibre Bragg grating based multiplexer and demultiplexer for DWDM applications.* Optics and Lasers in Engineering, 2005. **43**(9): p. 987-994.
78. Turitsyna, E.G. and S. Webb, *Simple design of FBG-based VSB filters for ultra-dense WDM transmission.* Electronics Letters, 2005. **41**(2): p. 89–91.
79. Ball, G.A. and W.H. Glenn, *Design of a single-mode linear-cavity erbium fiber laser utilizing Bragg reflectors.* Journal of Lightwave Technology, 1992. **10**(10): p. 1338 - 1343.
80. Ball, G.A., et al., *Low noise single frequency linear fibre laser.* Electronics Letters, 1993. **29**(18): p. 1623-1625.
81. Sejka, M., et al., *Distributed feedback Er3+-doped fibre laser.* Electronics Letters, 1995. **31**(17): p. 1445-1446.
82. Fermann, M.E., K. Sugden, and I. Bennion, *High-power soliton fiber laser based on pulse width control with chirped fiber Bragg gratings.* Optics Letters, 1995. **20**(2): p. 172-174.
83. Forster, R.J., et al., *Narrow linewidth operation of an erbium fiber laser containing a chirped Bragg grating etalon.* Journal of Lightwave Technology, 1997. **15**(11): p. 2130-2136.
84. Loh, W.H., et al., *High performance single frequency fiber grating-based erbium/ytterbium-codoped fiber lasers.* Journal of Lightwave Technology, 1998. **16**(1): p. 114-118.
85. Stepanov, D.Y., et al., *Apodized Distributed-Feedback Fiber Laser.* Optical Fiber Technology, 1999. **5**(2): p. 209-214.
86. Song, Y.W., et al., *40-nm-wide tunable fiber ring laser with single-mode operation using a highly stretchable FBG.* IEEE Photonics Technology Letters, 2001. **13**(11): p. 1167–1169.
87. Ibsen, M., et al., *Broad-band continuously tunable all-fiber DFB lasers.* IEEE Photonics Technology Letters, 2002. **14**(1): p. 21-23.
88. Yla-Jarkko, K.H. and A.B. Grudinin, *Performance limitations of high-power DFB fiber lasers.* IEEE Photonics Technology Letters, 2003. **15**(2): p. 191-193.
89. Baek, S., et al., *A cladding-pumped fiber laser with pump-reflecting inner-cladding Bragg grating.* IEEE Photonics Technology Letters, 2004. **16**(2): p. 407–409.
90. Fu, L.B., et al., *977-nm all-fiber DFB laser.* IEEE Photonics Technology Letters, 2004. **16**(11): p. 2442-2444.
91. Capmany, J., D. Pastor, and J. Martí, *EDFA gain equalizer employing linearly chirped apodized fiber gratings.* Microwave and Optical Technology Letters, 1996. **12**(3): p. 158-160.
92. Harun, S.W., et al., *Gain clamping in L-band erbium-doped fiber amplifier using a fiber Bragg grating.* IEEE Photonics Technology Letters, 2002. **14**(13): p. 293–295.
93. Kashyap, R., R. Wyatt, and R.J. Campbell, *Wideband gain flattened erbium fibre amplifier using aphotosensitive fibre blazed grating.* Electronics Letters, 1993. **29**(2): p. 154-156.
94. Kashyap, R., R. Wyatt, and P.F. McKee, *Wavelength flattened saturated erbium amplifier using multipleside-tap Bragg gratings.* Electronics Letters, 1993. **29**(11): p. 1025-1026.
95. Riant, I., *UV-photoinduced fibre gratings for gain equalisation.* Optical Fiber Technology, 2002. **8**(3): p. 171-194.
96. Cavaleiro, P.M., et al., *Simultaneous measurement of strain and temperature using Bragg gratings written in germanosilicate and boron-codoped germanosilicate fibers.* IEEE Photonics Technology Letters, 1999. **11**(12): p. 1635.

97. Cusano, A., et al., *Dynamic strain measurements by fibre Bragg grating sensor.* Sensors and Actuators A: Physical, 2004. **110**(1-3): p. 276-281.
98. Frazão, O., M.J.N. Lima, and J.L. Santos, *Simultaneous measurement of temperature and strain using type I and type IIA fiber Bragg gratings.* Journal of Optics A: Pure and Applied Optics, 2003. **5**(3): p. 183.
99. Frazão, O., et al., *Sampled fibre Bragg grating sensors for simultaneous strain and temperature measurement.* Electronics Letters, 2002. **38**(14): p. 693.
100. Frazão, O. and J.L. Santos, *Simultaneous measurement of strain and temperature using a Bragg grating structure written in germanosilicate fibres.* Journal of Optics A: Pure and Applied Optics, 2004. **6**(6): p. 553.
101. Guan, B.-O., et al., *Simultaneous strain and temperature measurement using a single fibre Bragg grating.* Electronics Letters, 2000. **36**(12): p. 1018.
102. James, S.W., M.L. Dockney, and R.P. Tatam, *Simultaneous independent temperature and strain measurement using in-fibre Bragg grating sensors.* Electronics Letters, 1996. **32**(12): p. 1133.
103. Jin, W., et al., *Simultaneous measurement of strain and temperature: Error analysis.* Optical Engineering, 1997. **36**: p. 598.
104. Jones, J.D.C. *Review of fiber sensor techniques for temperature-strain discrimination.* in *Twelfth International Conference on Optical Fiber Sensors.* 1997.
105. Xu, M.G., et al., *Discrimination between strain and temperature effects using dual-wavelength fibre grating sensors.* Electronics Letters, 1994. **30**(13): p. 1085.
106. Ferreira, L.A., et al., *Simultaneous measurement of displacement and temperature using a low finesse cavity and a fiber Bragg grating.* IEEE Photonics Technology Letters, 1996. **8**(11): p. 1519.
107. Rao, Y.J., et al., *Simultaneous measurement of displacement and temperature using in-fibre-Bragg-grating-based extrinsic Fizeau sensor.* Electronics Letters, 2000. **36**(19): p. 1610.
108. Yu, Y., et al., *Fiber Bragg grating sensor for simultaneous measurement of displacement and temperature.* Optics Letters, 2000. **25**(16): p. 1141.
109. Zhang, W., et al., *FBG-type sensor for simultaneous measurement of force (or displacement) and temperature based on bilateral cantilever beam.* IEEE Photonics Technology Letters, 2001. **13**(12): p. 1340.
110. Araújo, F.M., L.A. Ferreira, and J.L. Santos, *Simultaneous determination of curvature, plane of curvature, and temperature by use of a miniaturized sensing head based on fiber Bragg gratings.* Applied Optics, 2002. **41**(13): p. 2401.
111. Gwandu, B.A.L., et al., *Simultaneous measurement of strain and curvature using superstructure fibre Bragg gratings.* Sensors and Actuators A: Physical, 2002. **96**(2-3): p. 133.
112. Romero, R., et al., *Intensity-referenced and temperature-independent curvature-sensing concept based on chirped fiber Bragg gratings.* Applied Optics, 2005. **44**(18): p. 3821-3826.
113. Chen, G., et al., *Simultaneous pressure and temperature measurement using hi-bi fiber Bragg gratings.* Optics Communications, 2003. **228**(1-3): p. 99.
114. Nellen, P.M., et al., *Reliability of fiber Bragg grating based sensors for downhole applications.* Sensors and Actuators A: Physical, 2003. **103**(3): p. 364.
115. Zhao, Y., Y. Liao, and S. Lai, *Simultaneous measurement of down-hole high pressure and temperature with a bulk-modulus and FBG sensor.* IEEE Photonics Technology Letters, 2002. **14**(11): p. 1584.
116. Pereira, D.A., O. Frazão, and J.L. Santos, *Fiber Bragg grating sensing system for simultaneous measurement of salinity and temperature.* Optical Engineering, 2004. **43**(2): p. 299.
117. Shu, X., et al., *Sampled fiber Bragg grating for simultaneous refractive-index and temperature measurement.* Optics Letters, 2001. **26**(11): p. 774.
118. Theriault, S., et al. *High-g accelerometer based on an in-fibre Bragg grating sensor.* in *Conference on Optical Fibre Sensors.* 1996. Sapporo, Japan.
119. Todd, M.D., et al., *Flexural beam-based fiber Bragg grating accelerometers.* IEEE Photonics Technology Letters, 1998. **10**(11): p. 1605.

120. Yeo, T.L., et al., *Polymer-Coated Fiber Bragg Grating for Relative Humidity Sensing.* IEEE Sensors Journal, 2005. **5**(5): p. 1082–1089.
121. Davis, M.A., D.G. Bellemore, and A.D. Kersey, *Distributed fiber Bragg grating strain sensing in reinforced concrete structural components.* Cement and Concrete Composites, 1997. **19**(1): p. 45-57.
122. Davis, M.A. and A.D. Kersey. *Fiber Bragg grating sensors for infrastructure sensing.* in *Conference on Optical Fiber Communication, OFC'97*. 1997.
123. Lin, Y.B., et al., *Packaging methods of fiber-Bragg grating sensors in civil structure applications.* IEEE Sensors Journal, 2005. **5**(3): p. 419.
124. Maaskant, R., et al., *Fiber-optic Bragg grating sensors for bridge monitoring.* Cement and Concrete Composites, 1997. **19**(1): p. 21-33.
125. Jonathan, E., *Light synthesis with linearly chirped fibre Bragg gratings (FBGs) for optical coherence tomography (OCT) applications.* Optics Communications, 2005. **252**(1-3): p. 64-72.
126. Rao, Y.J., et al., *In-fiber Bragg-grating temperature sensor system for medical applications.* Journal of Lightwave Technology, 1997. **15**(5): p. 779 – 785.
127. Kersey, A.D., *A Review of Recent Developments in Fiber Optic Sensor Technology.* Optical Fiber Technology, 1996. **2**(3): p. 291-317.
128. Bennion, I., et al., *UV-written in-fiber Bragg gratings.* Optical and Quantum Electronics, 1996. **28**: p. 93-135.
129. Erdogan, T., *Fiber grating spectra.* Journal of Lightwave Technology, 1997. **15**(8): p. 1277-1294.
130. Giles, C.R., *Lightwave applications of fiber Bragg gratings.* Journal of Lightwave Technology, 1997. **15**(8): p. 1391-1404.
131. Kersey, A.D., et al., *Fiber grating sensors.* Journal of Lightwave Technology, 1997. **15**(8): p. 1442-1463.
132. Hill, K.O. and G. Meltz, *Fiber Bragg grating technology fundamentals and overview.* Journal of Lightwave Technology, 1997. **15**(8): p. 1263-1276.
133. Rao, Y.-J., *In-fibre Bragg grating sensors.* Measurement Science and Technology, 1997. **8**: p. 355-375.
134. Riant, I., *Fiber Bragg gratings for optical telecommunications.* Comptes Rendus Physique, 2003. **4**(1): p. 41-49.
135. Lee, B., *Review of the present status of optical fiber sensors.* Optical Fiber Technology, 2003. **9**: p. 57.
136. Frazão, O., et al., *Applications of Fiber Optic Grating Technology to Multi-Parameter Measurement.* Fiber and Integrated Optics, 2005. **24**: p. 227-244.
137. Othonos, A. and K. Kalli, *Fiber Bragg gratings: Fundamentals and applications in telecommunications and sensing.* 1999: Artech House.
138. Kashyap, R., *Fiber Bragg Gratings.* 1999: Academic Press.
139. Grattan, K.T.V. and B.T. Meggitt, *Optical Fiber Sensor Technology: Advanced Applications-Bragg Gratings and Distributed Sensors.* 2000.
140. López-Higuera, J.M., *Handbook of Optical Fibre Sensing Technology.* 2002: John Wiley.
141. Born, M. and E. Wolf, *Principles of optics.* Sixth ed. 1997, New York: Cambridge University Press.
142. Snyder, A.W. and J.D. Love, *Optical Waveguide Theory.* 1983: Chapman & Hall.
143. Yariv, A., *Coupled-mode theory for guided-wave optics.* IEEE Journal of Quantum Electronics, 1973. **QE-9**: p. 919-933.
144. Kogelnik, H., *Theory of optical waveguides.* Guided-Wave Optoelectronics, ed. T. Tamir. 1990, New York: Springer-Verlag.
145. Marcuse, D., *Theory of Dielectric Optical Waveguides.* 1991, New York: Academic Press.
146. Poladian, L., *Resonance Mode Expansions and Exact Solutions for Nonuniform Gratings.* Physics Review E, 1996. **54**: p. 2963-2975.
147. Haus, H.A. and W. Huang, *Coupled-mode theory.* Proceedings of the IEEE, 1991. **79**(10): p. 1505-1518.

148. Yamada, M. and K. Sakuda, *Analysis of almost periodic distributed feedback slab waveguides via a fundamental matrix approach.* Applied Optics, 1987. **26**(16): p. 3474-3478.
149. Erdogan, T., et al., *Decay of ultraviolet-induced fiber Bragg gratings.* Journal of Applied Physics, 1994. **76**: p. 73-80.
150. Rathje, J., M. Kristensen, and J.E. Pedersen, *Continuous anneal method for characterizing the thermal stability of ultraviolet written Bragg gratings.* Journal of Applied Physics, 2000. **88**: p. 1050-1055.
151. Hand, D.P. and P.S.J. Russel, *Photoinduced refractive-index changes in germanosilicate fibers.* Optics Letters, 1990. **15**: p. 102-104.
152. Neustruev, V.B., *Colour centres in germanosilicate glass and optical fibres.* Journal of Physics: Condensed Matter, 1994. **6**(35): p. 6901-6936.
153. Kristensen, M., *Ultraviolet-light-induced processes in germanium-doped silica.* Physical Review B, 2001. **64**(14): p. 4201-4212.
154. Friebele, E.J., D.L. Griscom, and G.H. Sigel, Jr., *Defect centers in a germanium-doped silica-core optical fiber.* Journal of Applied Physics, 1974. **45**(8): p. 3424-3428.
155. Kawazoe, H., *Effect of modes of glass-formation on structure of intrinsic or photon induced defects centered on III, IV or V cations in oxide glasses.* Journal of Non-Crystalline Solids, 1985. **71**(1-3): p. 231-243.
156. Tsai, T.E., et al., *Radiation-induced defect centers in high-purity GeO_2 glass.* Journal of Applied Physics, 1987. **62**(6): p. 2264-2268.
157. Malo, B., et al., *Photosensitivity in phosphorus-doped silica glass and optical waveguides.* Applied Physics Letters, 1994. **65**(4): p. 394-396.
158. Williams, D.L., et al., *Photosensitive index changes in germania-doped silica glass fibers and waveguides.* Proc. SPIE, 1993. **2044**: p. 55-68.
159. Konstantaki, M., et al., *Effects of Ge concentration, Boron co-doping, and hydrogenation on fiber Bragg grating characteristics.* Microwave and Optical Technology Letters, 2005. **44**(2): p. 148-152.
160. Maxwell, G.D., et al., *UV written 1.5 μm reflection filters in single mode planar silica guides.* Electronics Letters, 1992. **28**(22): p. 2106 - 2107.
161. Meltz, G. and W.W. Morey, *Bragg grating formation and germanosilicate fiber photosensitivity.* Proc. SPIE, 1991. **1516**: p. 185-189.
162. Poumelec, B. and F. Kherbouche, *The photorefractive Bragg gratings in the fibers for telecommunications.* Journal de Physique III, 1996. **6**: p. 1595-1624.
163. Williams, D.L., et al., *Enhanced UV photosensitivity in boron codoped germanosilicate fibres.* Electronics Letters, 1993. **29**(1): p. 45-47.
164. Atkins, R.M., et al., *Mechanisms of enhanced UV photosensitivity via hydrogen loading in germanosilicate glasses.* Electronics Letters, 1993. **29**(14): p. 1234-1235.
165. Lemaire, P.J., et al., *High pressure H_2 loading as a technique for achieving ultrahigh UV photosensitivity and thermal sensitivity in GeO_2 doped optical fibres.* Electronics Letters, 1993. **29**(13): p. 1191 - 1193.
166. Maxwell, G.D., et al., *UV written 13 dB reflection filters in hydrogenated low loss planar silica waveguides.* Electronics Letters, 1993. **29**(5): p. 425 - 426.
167. Bilodeau, F., et al., *Photosensitization of optical fiber and silica-on-silicon/silica waveguides.* Optics Letters, 1993. **18**(12): p. 953.
168. Krol, D.M., R.M. Atkins, and P.J. Lemaire, *Photoinduced second-harmonic generation and luminescence of defects in Ge-doped silica fibers.* Proc. SPIE, 1991. **1516**: p. 38-46.
169. Douay, M., et al., *Densification involved in the UV-based photosensitivity of silica glasses and optical fibers.* Journal of Lightwave Technology, 1997. **15**(8): p. 1329 - 1342.
170. Zhang, Q., et al., *Tuning Bragg wavelength by writing gratings on prestrained fibers.* IEEE Photononics Technology Letters, 1994. **6**: p. 839-841.
171. Prohaska, J.D., et al., *Magnification of mask fabricated fibre Bragg gratings.* Electronics Letters, 1993. **29**: p. 1614-1615.

172. Rourke, H.N., et al., *Fabrication and characterisation of long, narrowband fibre gratings by phase mask scanning.* Electronics Letters, 1994. **30**: p. 1341-1342.
173. Espejo, R.J., M. Svalgaard, and S.D. Dyer, *Analysis of a fiber bragg grating writing process using low coherence interferometry and layer-peeling.* Technical Digest: Symposium on Optical Fiber Measurements, 2004., 2004: p. 195-198.
174. Poladian, L., B. Ashton, and W. Padden, *Interactive design and fabrication of complex FBGs.* Optical Fiber Communications Conference, OFC'2003, 2003. **1**: p. 378-379.
175. Mizrahi, V. and J.E. Sipe, *Optical properties of photosensitive fibre phase gratings.* Journal of Lightwave Technology, 1993. **11**(10): p. 1513-1517.
176. Erdogan, T., *Cladding-mode resonances in short- and long period fiber grating filters.* Journal of Optical Society of America A, 1997. **14**(8): p. 1760-1773.
177. Berendt, M.O., et al., *Reduction of Bragg Grating-Induced Coupling to Cladding Modes.* Fiber & Integrated Optics, 1999. **18**(4): p. 255 - 272.
178. Delevaque, E., et al. *Optical fiber design for strong gratings photoimprinting with radiation mode supression.* in *Optical Fiber Communication Conference, OFC'95*. 1995.
179. Dong, L., et al., *Optical fibre with depressed claddings for suppression of coupling into cladding modes in fibre Bragg gratings.* IEEE Photonics Technology Letters, 1997. **9**(1): p. 64-66.
180. Komukai, T. and M. Nakazawa. *Efficient fiber gratings formed on high NA dispersion shifted fibers.* in *European Conference on Optical Communications*. 1995.
181. Skaar, J. and K.M. Risvik, *A Genetic Algorithm for the Inverse Problem in Synthesis of Fiber Gratings.* Journal of Lightwave Technology, 1998. **16**(10): p. 1928-1932.
182. Cormier, G., R. Boudreau, and S. Thériault, *Real-coded genetic algorithm for Bragg grating parameter synthesis.* Journal of the Optical Society of America B, 2001. **18**(12): p. 1771-1776.
183. Feced, R., M.N. Zervas, and M.A. Muriel, *An Efficient Inverse Scattering Algorithm for the Design of Nonuniform Fiber Bragg Gratings.* IEEE Journal of Quantum Electronics, 1999. **35**(8): p. 1105-1115.
184. Poladian, L., *Simple grating synthesis algorithm.* Optics Letters, 2000. **25**(11): p. 787-789.
185. Skaar, J., L. Wang, and T. Erdogan, *On the Synthesis of Fiber Bragg Gratings by Layer Peeling.* IEEE Journal of Quantum Electronics, 2001. **37**(2): p. 165-173.
186. Kieckbusch, S., C. Knothe, and E. Brinkmeyer. *Fast and accurate characterization of fiber Bragg gratings with high spatial and spectral resolution.* in *Conference on Optical Fiber Communication, OFC'2003*. 2003.
187. Yamada, Y., et al., *Silica based-optical waveguide on terraced silicon substrate as hybrid integration platform.* Electronics Letters, 1993. **29**: p. 444-446.
188. Hibino, Y., et al., *Wavelength division multiplexer with photoinduced Bragg gratings fabricated in a planar-ligthwave-waveguide-type asymmetric Mach-Zender interferometer on Si.* IEEE Photonics Technology Letters, 1996. **8**: p. 84-86.
189. Strasser, T.A., et al., *Ultraviolet laser fabrication of strong, nearly polarization-independent Bragg reflectors in germanium-doped silica waveguides on silica substrates.* Applied Physics Letters, 1994. **65**: p. 3308-3310.
190. Kohnke, G.E., et al. *Photosensitization of optical fiber by UV exposure of hydrogen loaded fiber.* in *Optical Fiber Communication Conference, OFC'99*. 1999.
191. Kawachi, M., M. Yasu, and T. Edahiro, *Fabrication of SiO –TiO glass planar optical waveguides by flame hydrolysis deposition.* Electronics Letters, 1983. **19**: p. 583–584.